

# A digital twin concept for a highly-loaded low-speed roller bearing

J. Baks



# A digital twin concept for a highly-loaded low-speed roller bearing

Master thesis report

by

**Jasper Baks**

To obtain the degree of Master of Science in  
Offshore and Dredging engineering  
at the Delft University of Technology,  
to be defended on Wednesday October 2, 2024 at 9:30

Student number:	5081424	
Thesis committee:	Dr. L. Pahlavan	TU Delft, Supervisor, Chair
	Dr.Ir. B. Scheeren	TU Delft, Daily supervisor
	Dr.Ir. J.H. den Besten	TU Delft
	R. el Boubsi	Huisman Equipment, Supervisor
	A. Vollebregt	Bluewater Energy Services, Supervisor
	A. Jones	Bluewater Energy Services, Supervisor

Mechanical Engineering  
Delft University of Technology  
The Netherlands  
October 2, 2024



# Preface

To graduate for my master program Offshore and Dredging engineering, a research has to be conducted. The topic of this research is as follows: ‘A digital twin concept for a highly-loaded low-speed roller bearing’. This research aims to develop a digital twin in order to predict the remaining useful life of these bearings, based on a condition monitoring model and a conventional fatigue model. This research was conducted in collaboration with Huisman Equipment and Bluewater Energy Services.

During this research, I learnt many new skills that made me grow both as a person and professionally. In the beginning of this research, I did not have much knowledge about fatigue problems. However, during this research, I gained a lot of knowledge over this subject. In addition, I gained a lot of knowledge on condition monitoring based on acoustic emission as it was completely new to me. Furthermore, I learned more about how large-scale experiments are done. At last, I learned a lot by working with the collected data.

I met a lot of people who helped me during my research, for which I am very grateful. During my time at both Huisman Equipment and Bluewater Energy Services, I was able to learn a lot from my colleagues which I will not forget anytime soon. As I met quite a lot of people, it will be too many names to mention them all. However, there are some names I would like to mention.

First of all, I would like to thank Pooria Pahlavan and Bart Scheeren for introducing me to this challenging but interesting research topic. I have learned a lot about presenting my findings, the fatigue problem and acoustic emission. I am very grateful for the support, guidance and feedback I received during this journey from you.

Second, I would like to thank Rachid el Boubsi for helping me integrate into Huisman Equipment. In the three months I worked at Huisman Equipment, I have learned a lot from you. Furthermore, you helped me to define the boundaries of my research and prevent me from making the scope of the research too large. In addition, you made me aware about possible bottlenecks when doing a master’ thesis and how to avoid them. For all these things, I am very grateful and I will not forget this anytime soon.

Third, I would like to thank Arjen Vollebregt and Aeron Jones for the time by Bluewater Energy Services. From the moment I stepped into Bluewater Energy Services, I felt welcomed. You helped me with finding the data and finalising the models. In addition, you helped me to get in touch with the right people to get the knowledge I needed to finish the models. For this, I am very thankful to you.

Finally, I would like to thank my friends and family. Especially my parents, brothers and sister, as this journey was not always easy, there were sometimes difficult moments, but you always helped me through them.

*Jasper Baks*  
*Delft, October 2024*

# Abstract

Highly-loaded low-speed roller bearings are commonly used in the offshore machinery, for example in turret moorings systems of Floating Production Storage and Offloading (FPSO) units and in slew bearings in heavy-lifting cranes. Safe and reliable operation and structural integrity can be ensured by monitoring the condition of the bearing. Condition monitoring based on acoustic emission (AE) has shown good potential for monitoring the health of highly-loaded low-speed bearings. With the increase in potential and proven condition monitoring methods, the need for lifetime predicting methods is increasing.

In this thesis, the feasibility of a digital twin (DT) concept is tested to make lifetime predictions of a highly-loaded low-speed roller bearing. The developed DT uses a combination of the Paris model and an AE-based model presenting the current state of the bearing. In the remaining useful life (RUL) prediction, the final crack size and total number of load cycles are determined based on an integrated form of the Paris model. Three different forms were tested for the RUL prediction.

The Paris model and the AE-based model showed good agreement in a benchmark case, based on which the two models were combined. The AE-based prediction was tested for hits and counts, with the counts yielding into better results due to a better fitting of the model constants. The linear RUL based on the number of load cycles resulted in the best prediction. The developed DT showed good potential in making lifetime predictions of highly-loaded low-speed roller bearings and enrichment of future DTs with prognostic information.

# Table of Contents

<b>List of Figures</b>	<b>v</b>
<b>List of Tables</b>	<b>vii</b>
<b>Nomenclature</b>	<b>viii</b>
<b>1 Introduction</b>	<b>1</b>
1.1 Research scope . . . . .	2
1.2 Layout . . . . .	3
<b>2 Literature</b>	<b>4</b>
2.1 Digital twin . . . . .	4
2.1.1 What is a digital twin . . . . .	4
2.1.2 Types of digital twins . . . . .	5
2.2 Wear mechanisms . . . . .	7
2.2.1 Fatigue wear . . . . .	7
2.2.2 Rolling contact fatigue . . . . .	8
2.2.3 Adhesive wear . . . . .	8
2.2.4 Abrasive wear . . . . .	8
2.2.5 Corrosive wear . . . . .	9
2.3 Stages of wear during roller bearings service life . . . . .	9
2.3.1 Running-in stage . . . . .	9
2.3.2 Steady state stage . . . . .	9
2.3.3 Defect initiation . . . . .	9
2.3.4 Defect propagation . . . . .	10
2.3.5 Damage growth . . . . .	10
2.4 The Hertzian contact theory . . . . .	11
2.4.1 Assumptions . . . . .	11
2.4.2 Contact area and pressure distribution . . . . .	12
2.4.3 Stresses in material . . . . .	14
2.4.4 Line contact versus point contact . . . . .	15
2.5 Lifetime predicting models . . . . .	17
2.5.1 Fracture mechanics . . . . .	17
2.6 Acoustic emission monitoring . . . . .	21
2.6.1 Acoustic emission based fracture model . . . . .	22
2.6.2 Parameters for acoustic emission based fracture model . . . . .	24
2.7 Remaining useful life . . . . .	25
<b>3 Methodology</b>	<b>27</b>
3.1 Input data . . . . .	27
3.2 Determining load cycles . . . . .	27
3.3 Force on grid cell . . . . .	29
3.4 Stresses . . . . .	29
3.5 Fracture . . . . .	29
<b>4 Linear bearing test</b>	<b>31</b>

<b>5</b>	<b>Results and Discussion</b>	<b>33</b>
5.1	Linear bearing test . . . . .	33
5.1.1	Hits vs counts . . . . .	33
5.1.2	Sensitivity study . . . . .	34
5.1.3	Influence signal length . . . . .	35
5.1.4	Acoustic emission model compared to the Paris model . . . . .	36
5.1.5	Remaining useful life . . . . .	39
5.2	Aoka Mizu . . . . .	39
5.2.1	Timesteps in data . . . . .	40
5.2.2	Remaining useful life . . . . .	42
5.2.3	Influence counts on Remaining useful life prediction . . . . .	49
5.2.4	Sensitivity study . . . . .	50
5.2.5	Influence AE interval . . . . .	52
<b>6</b>	<b>Conclusion and Recommendations</b>	<b>55</b>
6.1	Recommendations . . . . .	56
	<b>References</b>	<b>58</b>
<b>A</b>	<b>Appendix A - Derivation total number of load cycles to failure equation</b>	<b>62</b>
<b>B</b>	<b>Appendix B - RUL of bearing based on the Paris model</b>	<b>63</b>
<b>C</b>	<b>Appendix C - Remaining useful life based on only AE</b>	<b>64</b>
<b>D</b>	<b>Appendix D - Sensitivity study</b>	<b>66</b>
<b>E</b>	<b>Appendix E - Influence AE interval</b>	<b>72</b>

# List of Figures

1	Examples of industries where highly-loaded low-speed roller bearings are used . . . . .	1
2	An example of physics informed machine learning [53] . . . . .	6
3	An example of machine learning assisted simulation [53] . . . . .	6
4	An example of explainable artificial intelligence [53] . . . . .	7
5	The adhesive wear mechanism [28] . . . . .	8
6	Mechanisms of abrasive wear: microcutting (a), microfracture (b), pull-out (c) and individual grains (d) [28] . . . . .	8
7	The primary fatigue modes [32] . . . . .	10
8	The different wear stages in the life of a roller bearing and their dynamic severity [14]	11
9	The pressure distributions for an elliptical and a cylinder-on-cylinder contact [36] . .	12
10	The directions of the radii of the ellipse [54] . . . . .	13
11	The stresses in the material [36] . . . . .	15
12	Contact pressure for a line and point contact . . . . .	16
13	The contact width of a point contact . . . . .	16
14	The crack size against the number of cycles [31] . . . . .	18
15	The crack growth rate against the stress intensity range [37] . . . . .	19
16	The effect of the stress ratio and the material constant $\gamma$ [31] . . . . .	20
17	Acoustic emission parameters [47] . . . . .	21
18	An example of the relation between acoustic emission and the fracture parameters [55]	23
19	An example of different types of hits [55] . . . . .	24
20	Data points for initial guess of $B$ [55] . . . . .	25
21	An example of the shape of the grid cells and how they are counted . . . . .	28
22	The movement of the rollers from their old location to their new location . . . . .	28
23	The roadmap for the methodology of the DT . . . . .	30
24	The test set-up for the linear bearing test done by Huisman Equipment . . . . .	31
25	The six different sensor locations . . . . .	31
26	The hit-rates for the test 3-1-3 . . . . .	32
27	The $\Delta K$ for both the count and hit rate . . . . .	33
28	Sensitivity study of the intercept constant $B$ . . . . .	34
29	Sensitivity study of the slope exponent $p$ . . . . .	35
30	The influence of the signal length on the resulting $\Delta K$ . . . . .	35
31	The growth of $\Delta K$ over the load cycles done . . . . .	36
32	The $\Delta K$ for both the Paris model as the acoustic emission model for testcase 3-1-3 .	37
33	The $\Delta K$ for both the Paris model as the acoustic emission model for testcase 3-1-2 .	38
34	The $\Delta K$ for both the Paris model as the acoustic emission model for testcase 3-1-1 .	38
35	The comparison of different options for the RUL prediction . . . . .	39
36	The rotations of the turret in half an hour . . . . .	40
37	The difference in load cycles done for a timestep of 1 and 3 minutes in one month .	41
38	The RUL of the bearing of the Aoka Mizu in half 2024 . . . . .	42
39	The RUL development of the RUL without AE . . . . .	43
40	The sensor locations for the linear bearing [44] . . . . .	44
41	The placement of the sensors . . . . .	44
42	The AE data set of the entire linear bearing experiment . . . . .	45
43	Graphical representation on how the AE data is related to the Aoku Mizu data . . .	45
44	The RUL predictions based on the 4 sensor locations after half 2024 . . . . .	46
45	The RUL development at the most right side of the bearing . . . . .	47

46	The RUL predictions based on AE of the 4 sensor locations after half 2024 . . . . .	48
47	The RUL development based on only AE of sensor location U . . . . .	49
48	The RUL predictions based on higher counts for the sensor positions after half 2024	50
49	The RUL predictions based on different initial crack sizes for sensor location U after half 2024 . . . . .	51
50	The development of the RUL for the different initial crack sizes for sensor location U	52
51	The sensitivity of the RUL prediction to the initial crack size for sensor location U .	52
52	The RUL predictions based on different AE intervals for sensor location U after half 2024 . . . . .	53
53	The RUL development for the different AE intervals for sensor location U . . . . .	54
54	The RUL of the bearing of the Aoka Mizu in half 2024 . . . . .	63
55	The RUL development based on only AE of sensor location A . . . . .	64
56	The RUL development based on only AE of sensor location B . . . . .	64
57	The RUL development based on only AE of sensor location L . . . . .	65
58	The RUL predictions based on different initial crack sizes for sensor location A after half 2024 . . . . .	66
59	The RUL predictions based on different initial crack sizes for sensor location B after half 2024 . . . . .	67
60	The RUL predictions based on different initial crack sizes for sensor location L after half 2024 . . . . .	68
61	The development of the RUL for the different initial crack sizes for sensor location A	69
62	The development of the RUL for the different initial crack sizes for sensor location B	69
63	The development of the RUL for the different initial crack sizes for sensor location L	70
64	The sensitivity of the RUL prediction to the initial crack size for sensor location A .	70
65	The sensitivity of the RUL prediction to the initial crack size for sensor location B .	71
66	The sensitivity of the RUL prediction to the initial crack size for sensor location L .	71
67	The RUL predictions based on different AE intervals for sensor location A after half 2024 . . . . .	72
68	The RUL predictions based on different AE intervals for sensor location B after half 2024 . . . . .	73
69	The RUL predictions based on different AE intervals for sensor location L after half 2024 . . . . .	74
70	The RUL development for the different AE intervals for sensor location A . . . . .	74
71	The RUL development for the different AE intervals for sensor location B . . . . .	75
72	The RUL development for the different AE intervals for sensor location L . . . . .	75



# List of Tables

1	The advantages and disadvantages of the different types of digital twins . . . . .	7
2	The maximum Tresca and von Mises stresses [16] . . . . .	15
3	Used parameter values for Paris model and acoustic emission model . . . . .	25
4	The values for the different load levels . . . . .	32
5	The predicted total number of load cycles to failure . . . . .	43

# Nomenclature

## Abbreviations

AE	Acoustic Emission
BCI	Bearing Condition Index
DER	Dark Etching Regions
DT	Digital Twin
FEM	Finite Element Method
FPSO	Floating Production Storage and Offloading
REB	Rolling Element Bearing
RUL	Remaining Useful Life
SIF	Stress Intensity Factor
WEB	White Etching Regions

## Symbols

$\alpha$	Plane stress/strain constraint factor	—
$\alpha_e$	Approximated constant for the elliptical contact	—
$\alpha_k$	Source mechanism scaling	—
$\alpha_q$	Sensor type scaling	—
$\beta$	Approximated constant for the elliptical contact	—
$\Delta a$	Crack growth in a certain time frame $dN$	<i>mm</i>
$\Delta K$	Stress intensity factor range	<i>MPa<math>\sqrt{m}</math></i>
$\Delta K_P$	The stress intensity factor based on the Paris model	<i>MPa<math>\sqrt{m}</math></i>
$\Delta K_{AE}$	The stress intensity factor based on the acoustic emission model	<i>MPa<math>\sqrt{m}</math></i>
$\Delta K_{avg}$	The averaged stress intensity factor over both models	<i>MPa<math>\sqrt{m}</math></i>
$\Delta K_{th}$	Stress intensity factor threshold	<i>MPa<math>\sqrt{m}</math></i>
$\Delta N$	The number of load cycles done in a certain time frame	—
$\frac{da}{dN}$	Crack growth rate	<i>mm/cycle</i>
$\frac{dParameter}{dN}$	Acoustic emission parameter rate	<i>1/cycle</i>
$\gamma$	Material constant for depends stress ratio on the crack growth	—
$\kappa$	Approximated constant for the elliptical contact	—

$\lambda$	Ratio between the effective radii	—
$\nu_1$	Poisson ratio of body 1	—
$\nu_2$	Poisson ratio of body 2	—
$\sigma_c$	Compressive stress	<i>MPa</i>
$\sigma_n$	Normal stress on the crack surfaces	<i>MPa</i>
$\sigma_x$	Normal stress in the x-direction	<i>MPa</i>
$\sigma_y$	Normal stress in the y-direction	<i>MPa</i>
$\sigma_z$	Normal stress in the z-direction	<i>MPa</i>
$\sigma_{max}$	Max stress	<i>MPa</i>
$\sigma_{vM}$	Von Mises stress	<i>MPa</i>
$\tau_{13max}$	Max shear stress in x and z direction	<i>MPa</i>
$\tau_{max}$	Max shear stress	<i>MPa</i>
$\tau_{semax}$	Max effective shear stress	<i>MPa</i>
$\tau_{se}$	Effective shear stress	<i>MPa</i>
$\theta$	Angle of the crack	deg
$\Theta_r$	The angle between the rollers	rad
$a$	Crack length	<i>mm</i>
$A_0$	Newmann's coefficient	—
$A_1$	Newmann's coefficient	—
$A_2$	Newmann's coefficient	—
$A_3$	Newmann's coefficient	—
$a_c$	Contact half width of cylindrical contact	<i>mm</i>
$a_e$	Major axis of elliptic contact	<i>mm</i>
$a_f$	The final predicted crack size	<i>mm</i>
$a_M$	Major axis	<i>mm</i>
$B$	Intercept constant of the acoustic emission model	—
$b$	Minor axis	<i>mm</i>
$b_e$	Minor axis of elliptic contact	<i>mm</i>
$C$	Intercept constant of the Paris model	—
$c$	Counts	—
$C_B$	Bearing condition index	—
$c_e$	Effective contact length	<i>mm</i>

$c_{ave}$	Count factor	—
$c_{k,q_i}$	Number of identified acoustic emission signals	—
$D$	Intercept constant of the acoustic emission model for the crack growth	—
$D_M$	Miner's damage parameter	—
$dN$	Load cycles done in a certain time frame	—
$E'$	Effective elastic modulus	$MPa$
$E_1$	Elastic modulus of body 1	$MPa$
$E_2$	Elastic modulus of body 2	$MPa$
$E_m$	Approximated constant for the elliptical contact	—
$F$	Contact force	$kN$
$f$	Newmann crack closure function	—
$H$	Hits	—
$K$	Stress intensity factor	$MPa\sqrt{m}$
$k$	Friction coefficient	—
$k$	Indices of the source mechanism	—
$K_c$	Critical stress intensity factor/ fracture toughness	$MPa\sqrt{m}$
$K_e$	Elliptical ratio	—
$K_s$	Considered source mechanisms	—
$L$	Length of roller	$mm$
$m$	Approximated constant for the elliptical contact	—
$N$	The total number of load cycles done	—
$n$	Slope constant of the Paris model	—
$N_f$	The total predicted number of load cycles to failure	—
$n_i$	The number of load cycles done at a certain load	—
$N_M$	The number of load cycles a material can hold for that load	—
$p$	Pressure distribution over the contact	$MPa$
$p$	Slope constant of the acoustic emission model	—
$p_N$	NASGRO exponent for stage I	—
$P_{c,max}$	Max cylindrical pressure	$MPa$
$P_{c,mean}$	Mean cylindrical pressure	$MPa$
$P_{e,max}$	Max elliptical pressure	$MPa$
$P_{e,mean}$	Mean elliptical pressure	$MPa$

$Q$	Implemented sensor types	—
$q$	Slope constant of the acoustic emission model for the crack growth	—
$q_i$	Indices of the sensor type	—
$q_N$	NASGRO exponent for stage III	—
$R$	Stress ratio	—
$R_1$	Radius of cylindrical body 1	<i>mm</i>
$R_2$	Radius of cylindrical body 2	<i>mm</i>
$R_x$	Effective radius in the x-direction	<i>mm</i>
$R_y$	Effective radius in the y-direction	<i>mm</i>
$R_{1x}$	Radius in x-direction of elliptic body 1	<i>mm</i>
$R_{1y}$	Radius in y-direction of elliptic body 1	<i>mm</i>
$R_{2x}$	Radius in x-direction of elliptic body 2	<i>mm</i>
$R_{2y}$	Radius in y-direction of elliptic body 2	<i>mm</i>
$R_{eff}$	Effective radius	<i>mm</i>
$S_{fl}$	Material flow strength	<i>MPa</i>
$x$	x-direction	<i>mm</i>
$Y$	Geometry factor	—
$y$	y-direction	<i>mm</i>
$z$	Depth of at which the stress is calculated	<i>mm</i>
$z_{@ \tau_{max}}$	Max shear stress depth	<i>mm</i>

# 1 Introduction

Highly-loaded low-speed roller bearings have great usage in the offshore industry. Examples of these bearings are the slew bearings used in heavy-lifting cranes, Turret Moorings Systems of FPSO's and the nacelle-slew or blade-pitch bearings in wind turbines. In Figure 1 two different industries are shown. In Figure 1a, the deepwater construction vessel Aegir of Heerema Marine Contractors is shown. This vessel has a slew bearing to yaw the boom and sheave bearings to guide the hoisting wire ropes. In Figure 1b, the Aoka Mizu of Bluewater Energy Services is shown. The single point mooring turret of this FPSO contains a toothless slew bearing, which allows for rotation of the vessel around fixed mooring chains [43]. Meaning that these bearings are used in the oil and gas industry, renewables industry and in the decomposition industry.



(a) Deepwater construction vessel Aegir [19]



(b) The FPSO Aoka Mizu [4]

Figure 1: Examples of industries where highly-loaded low-speed roller bearings are used

These bearings are subjected to operational and motion induced loading. In addition, the interaction between these loads is unpredictable. Furthermore, the bearings operate in rough conditions, due to the harsh seawater environment. These conditions are not favorable for the lubrication used in these bearings, as these rough conditions may lead to reduced or even broken lubrication films. The defected film has significant impact on the wear evolution.

Safe and reliable operation conditions has a high priority in the offshore industry, due to the harsh and remote environment these bearings and ships work in. To cope with these conditions, the structures are held to the highest safety and reliability standards available. Meaning that the integrity of the critical roller bearings is essential to ensure a safe working environment.

The standards of the manufactures of these structures prescribe that regular inspection is needed, for instance on a yearly basis or after a few thousand operating hours. There are, however, only limited amount of methods to do these inspections. For slew bearings, lubrication sampling and testing, tilting clearance measurements and visual inspection through endoscopy can be used for these inspection for instance. These methods can be expanded to full internal inspection for other bearings. In full internal inspection, the disassembly of bearing is needed for a part or the full bearing. The methodology described by Scheeren shows a good potential to perform condition monitoring for these large-scale low-speed roller bearings. [43]

The lifetime prediction for these bearings are critical, as unexpected failure will come with major cost. The bearings are theoretically designed to have an operating life of decades. However, due to the harsh environment, failure can occur in an earlier state than expected [47]. These bearings

are only made by a limited number of fabricators and are often custom made. As a result, the replacement can therefore take months when the failure is unexpected. Limiting factors for replacement can be for instance having no spare parts, the spare parts are on the other side of the world and having no port space to do the replacement. The combination of the expensive bearing/bearing parts and the coupled operational down-time will make the replacement very expensive.

By making good estimations of the remaining lifetime the cost of the replacement can be reduced, as the failure of the bearing will not be fully unexpected. Meaning that good replacement plans can be made to reduce down-time. As the bearing can be ordered in time and the replacement can be scheduled for when the operating ship, for instance, is in the port. With good lifetime prediction, the replacement cost of the bearing can be lowered and the integrity of the bearing can be assured. However, there are only limited methodologies which use real time condition monitoring data to make lifetime predictions for these critical large-scale low-speed roller bearings. So, that is why this research will look into having a condition monitoring based model for predicting the remaining lifetime of the bearing.

## 1.1 Research scope

Acoustic emission monitoring has shown to be a good method to monitor highly-loaded low speed roller bearings. Based on this monitoring the health state of the bearing can be predicted [43]. The health state information is important, especially when it can be used to make predictions on the remaining useful life of the bearing. During this research a digital twin will be developed, which is capable of making reliable remaining useful life predictions of the bearing.

The digital twin will be developed as a concept. Meaning that the models used for the digital twin do not have the highest fidelity, but high enough to test the potential of the concept. The development of the digital twin is based on the main research question of this thesis, which reads:

”How can a digital twin be developed to predict the remaining useful life of a highly-loaded low-speed roller bearing?”

In order to answer this research question, it had to be divided into several sub research questions which are:

1. What type of heart does the digital twin needs to have and how to implement it?
2. What type of data needs to be used and how can it be used for predicting the remaining useful life of a bearing?
3. How to enhance the accuracy of the digital twin in predicting the remaining useful life of the bearing?
4. How to combine existing lifetime prediction models with acoustic emission?

## 1.2 Layout

This report is divided into four chapters to answer the main research question. Chapter 2 covers the theory needed to set up the DT. The methodology of the DT for making RUL predictions for the bearing is explained in Chapter 3. The linear bearing test done by Huisman Equipment is described in Chapter 4. In Chapter 5, the results of the DT based on experimental data are shown. Furthermore, the results are evaluated. At last, Chapter 6 gives the conclusion of the report. In addition, some recommendations are given for future work. At the end of the report the appendices are shown. In Appendix A, the derivation of the total number of fatigue cycles to failure is given. Appendix B shows a zoomed in Figure of RUL prediction based on the Paris model. In Appendix C, the remaining useful life development figures based on AE are shown. Appendix D shows the sensitivity study of RUL to the crack size of the sensor locations A,B and L. Finally, appendix E, the influence of the AE interval figures are shown.



## 2 Literature

### 2.1 Digital twin

#### 2.1.1 What is a digital twin

In 2003, the concept of the digital twin (DT) was first presented by Michael Grieves. The definition of a DT given by Grieves is: “a DT is a comprehensive software representation of an individual physical object.” [35] The representation of the physical object includes conditions, properties and the behaviour of the physical object. These features are taken into account through models and data of the physical object. The DT will remain the virtual counterpart of the physical object over the entire lifetime of the physical object.

Since the introduction of the DT, it has gained interests of both academia and industry. At first, it was mainly used in the manufacturing industry. After that it gained popularity in the communities of the Internet of Things and the cyber physical systems. Due to the increasing popularity, the definition of the DT has changed over time and its definition can also differ between different fields of interest.

The requirements to be met by the DT differ from one field to another. In the field of gaming and the related platforms, the DT must comply with the following four aspects:

1. Representing the changing characteristics of the object using a continuous data flow
2. The physical and virtual object are continuously tracked to locate or relate them in space and time
3. Models which can capture the behaviour of the physical object and reasoning about events
4. The virtual object must meet the constraints of the physical world

The features described above are relevant for the evolution of the DT. As, the physical object will change over time in terms of status, behaviour and its reaction to events. These changes are captured by physical laws, meaning that the virtual object needs to obey these laws. In addition, these changes are captured by the continuous data flow of the physical object. So, the virtual object needs to mirror this information properly.

A major part of the DT is the representation of the physical object with respect to the relevant characteristics and behaviour of it. The representation must be considered based on the following parameters:

1. Similarity, to what extent and how well does the virtual object reproduces the physical object and its status and characteristics
2. Randomness, the likelihood that the virtual object has a different state or has other diverging characteristics from the physical object
3. Contextualization, in what way the previous two features must be considered in the context of the operation. For example, in a specific environment, it is highly likely that only a subset of all the characteristics, properties and information is relevant from the physical object. [35]

Based on this information, the following definition of the DT will be used during this thesis. A digital twin is a virtual representation of a physical object in a virtual space, where the virtual object is linked with the physical object, the link is in the form of data transfer, this data flow can be unidirectional or bidirectional, with the goal to optimise or predict a process in the real world. In this thesis, the data flow will be unidirectional from the physical object to the virtual object.

### 2.1.2 Types of digital twins

A DT uses models to describe the behaviour of the physical object. The models used to describe the behaviour vary and therefore there exist multiple different types of DTs. The types can be divided into three categories: physics-based, data-driven and hybrid DT. [34][53]

The physics-based DT makes use of physics-based models to describe the behaviour of the object. The different types of physics-based models commonly used are empirical equations, multi-physics coupling models and finite element models (FEM).

Empirical equations are used to observe and analyse the variations of physical phenomena. When facing complex problems not all empirical equations can be used, as some equations contain a limited amount of physics. Resulting in an inadequately performance and due to complex dynamics, the DT will lack robustness under complex working. Simulation models, such as FEM, can be used to solve the high-complexity problems.

The physics-based models used in the physics-based DT are often considered as white-box models. As, the models are purely based on physics making them easy to understand. However, a major downfall of the physics-based method is the computation time, as it will increase with the complexity of the problem. Resulting in high computational burden for the problems where high-fidelity FEM simulations are needed to be used.

The data-driven DT is most of the time based on deep learning, machine learning and transfer learning algorithms. Machine learning-based algorithms extract features from control signals to represent device information. However, in conventional techniques, feature extraction is limited to simpler problems due to the limited ability to extract features. [53]

Deep learning is part of machine learning. However, these two do differ due to the way they use the input data. In machine learning, the data needs to be labelled first to make predictions. While in deep learning, this labelling step is eliminated. For example, multiple pictures of different types of pets have to be categorized by 'dog', 'cat' et cetera. Deep learning algorithms can determine the most important features to distinguish the different animals. While in machine learning, these features have to be established by a human expert [21]. Due to this ability, it can be used to create end-to-end models, a model which is trained to map the input to the desired output [49], for complex problems.

Transfer learning algorithms extract information from known domains to address problems in related domains. This ability can be useful in complex deep learning models, as the computational time for the hyperparameter optimisation can be reduced.

The data-driven DTs are good in finding complex non-linear relations. However, the major downside of this method is the interpretability of the method used forming a so called black box.

In hybrid DTs, physics-based models and data driven algorithms are combined. Three examples of these hybrid DTs are physics-informed machine learning, machine learning-assisted simulation and explainable artificial intelligence.

In physics-informed machine learning, the interpretability of the DT is increased by using physics. The integration of physics can be done in three different parts of the data driven DT which are in the data, modelling and loss functions. For the data, it can be generated with physics-based models. For the modelling, the internal components of the data-driven model

can be designed based on physics. The loss function is used to decrease the loss between the estimation and the observation, by using physics for establishing the loss function, the data-driven model will have consistency with physics. An example of a physics-informed machine learning is shown in Figure 2.

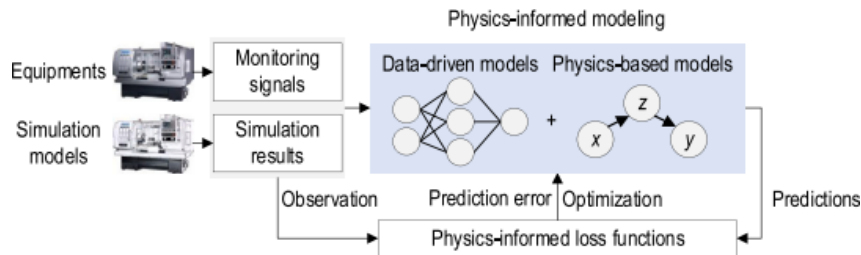


Figure 2: An example of physics informed machine learning [53]

In machine learning assisted simulation, data-driven algorithms are used to reduce the computational burden of high fidelity physics-based DTs. The data-driven algorithms can be used to construct reduced-order models. However, this is not always possible, as intrusive and non-intrusive reduction methods are used. For the intrusive reduction method, full knowledge of the governing equations and the discretized dynamic system is needed. However, data-driven models can be used for solving the differential equations. In this way, the computational burden is reduced. In Figure 3, an example of machine learning assisted simulation is shown.

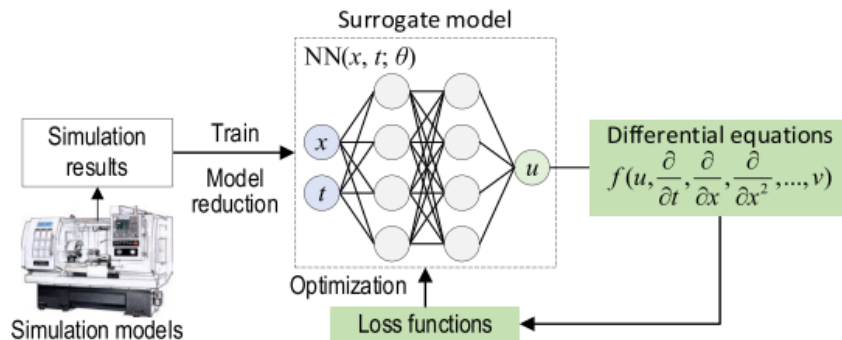


Figure 3: An example of machine learning assisted simulation [53]

In explainable artificial intelligence, the understanding of the model is obtained after the training of the data-driven models, using post-hoc explanations. To improve the interpretability and transparency of neural networks, activation maximization is applied to a deep convolutional network to find representative input samples. The similarity between the representative samples and the feature maps of convolutional neural networks is regarded as the weight of the outputs to improve the interpretability and transparency of the neural network. An example of explainable artificial intelligence is shown in Figure 4. [53]

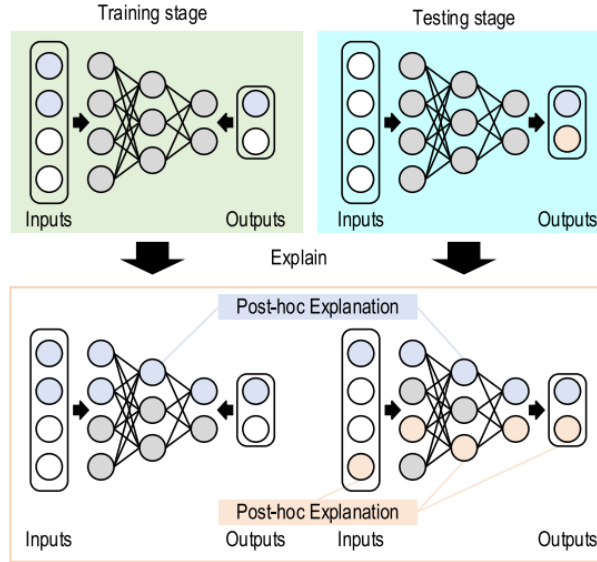


Figure 4: An example of explainable artificial intelligence [53]

In table 1, the advantages and disadvantages of the different DTs are summarized. A physics-based DT will be used for this thesis, as the advantage of having a model which is easy to interpretate outways the potential of having a computational expensive DT. In addition, both the data-driven and hybrid DT lack interpretability and for the data-driven DT physical meaning is also lacking.

Table 1: The advantages and disadvantages of the different types of digital twins

Type of digital twin	Advantages	Disadvantages
<b>Data-driven</b>	Non-linear relations	Black box Large amount of experimental data
<b>Physics-based</b>	Easy interpretation	Computational burden
<b>Physics-informed machine learning</b>	Non-linear relations	Black box
<b>Machine learning assisted simulation</b>	Reduced computational burden	Reduced interpretation
<b>Explainable artificial intelligence</b>	Non-linear relations	Grey box

## 2.2 Wear mechanisms

In roller bearings several wear mechanisms can be active. These wear mechanisms will be discussed in this section. The wear in rolling element bearings (REB) originates from subsurface inclusions and surface asperities [14].

### 2.2.1 Fatigue wear

In systems, which are dynamically loaded, fatigue wear can occur. The fatigue wear can be due to elastic contacts, which result in high number of cycles needed for the fatigue. Additionally, plastic contacts will result in a low number of cycles needed for the fatigue mechanism.

### 2.2.2 Rolling contact fatigue

In rolling contact fatigue, local (sub-)surface shear stress fields, plastic deformations and dislocations are results of the dynamic contact conditions and the possible hoop and tangential stresses, which are amplified by local asperities and/or by contacts with contaminated particles. The nucleation will eventually crack at the defects or inclusions in the micro structure. [17]

### 2.2.3 Adhesive wear

Due to relative motion between the contacting surfaces adhesive wear can occur. The surface texture is modified due to adhesive wear, as the relative motion results in plastic deformation and material transfer from one surface to another [28], as shown in Figure 5. Adhesive wear mainly occurs in roller bearings with a poor lubrication state [17]. The sliding event involved in the adhesive wear is hard to estimate in rolling contacts, as the rolling will be dominant [14].

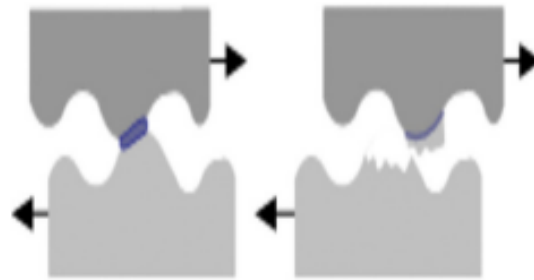


Figure 5: The adhesive wear mechanism [28]

### 2.2.4 Abrasive wear

Solid, hard particles can cause local stress peaks, which may cause abrasive wear to happen. As it mainly occurs when a soft surface is hit by a hard surface, in this case a hard particle. In addition, abrasive wear can take place in contacts between rough surfaces. In abrasive wear, four different mechanisms can occur. These are micro cutting, microfracture, pull-out and individual grains, shown in Figure 6. [28][17]

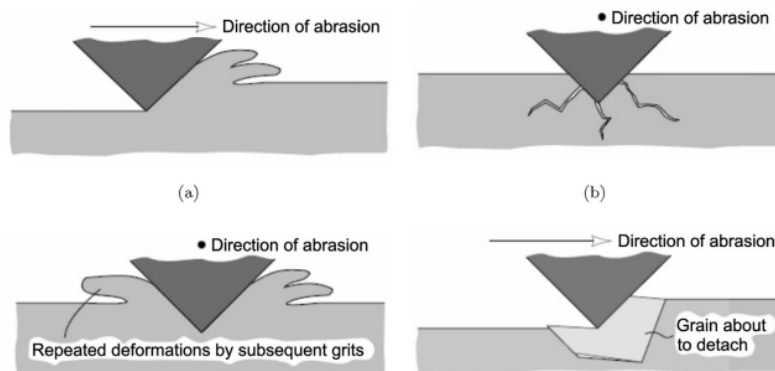


Figure 6: Mechanisms of abrasive wear: microcutting (a), microfracture (b), pull-out (c) and individual grains (d) [28]

### 2.2.5 Corrosive wear

Corrosive wear also called tribochemical wear can be divided into two types namely moisture corrosion and frictional corrosion. The wear happens due to chemical or electrochemical reactions in the tribological contacts. These reactions will result in the formation of brittle or soft layers, which are subsequently removed in the contact event. [28][17]

## 2.3 Stages of wear during roller bearings service life

The wear evolution progress during the lifetime of roller bearing can be divided into five different stages. These are the running-in stage, steady state stage, defect initiation, defect propagation and damage growth [14].

### 2.3.1 Running-in stage

Due to surface manufacturing, the REBs will have some degree of surface roughness and surface waviness. These surface asperities will interact with each other during the running-in stage, resulting in microplastic flow, work hardening and shakedown. During the running-stage, a 'roll polishing' effect occurs in REB, mainly due to plastic deformations of surface asperities. As the surface roughness decreases, the polishing effect will gradually disappear. In addition, the lubrication film will become uniform over time. Due to the shakedown response (first stage of cyclic loading), the subsurface hardness will increase. The subsurface hardness will increase until the work hardening is saturated, meaning that the steady state stage is started. During the running-in stage, only some mild wear will occur on the interacting surfaces. [14][17]

### 2.3.2 Steady state stage

During the steady state stage, the response of the REB will be steady as a result of having almost no wear during this phase. The no wear is due to having uniform Hertzian stresses and lubrication film. However, in this stage dark etching regions (DER) and white etching bands (WEB) are formed. DER and WEB are irreversible microstructural alterations in the subsurface [25]. The length of this stage depends on the maximum load induced stress, operating temperature and material characteristics. [14]

### 2.3.3 Defect initiation

The defect initiation phase consists of two phases, which are the crack initiation phase and the crack opening state [14]. In the defect initiation phase, cracks will start to form, this crack can form at the surface and at the subsurface. In the case that the crack forms at the subsurface, the dominant mechanism for rolling contact fatigue will be spalling. These micro cracks are formed below the surfaces in the region of maximum shear stress. [42]

When the first micro-cracks form due to the wear progression of dented surfaces, the dominant mechanism will be surface pitting. These surfaces can form due to high stresses, contamination, vibrations and lubrication disturbances. The formation of cracks is seen as the core of the fatigue wear process. At the trailing edge of the dent, a crack will form on the surface. Later, new defects will form around the edges of the dent, due to relatively high local surface stresses which are created due to the dent. [14]

Crack opening depends on the stress which is applied on the crack [48]. The opening of the crack can be divided into three primary fatigue modes, these modes also determine the orientation of a crack relative to the loading. Mode I is the opening mode and is due to a tensile stress pulling the crack faces apart. Mode II is due to a shear stress which slides the crack faces in the parallel direction to the primary crack dimension, mode II is called the sliding mode. Mode III, the tearing mode, is due to a shear stress which slides the crack faces in the perpendicular direction to the primary crack dimension. The different fatigue modes are shown in Figure 7. Mode I is the most common and worst-case scenario. In addition, cracks which are formed due to Mode II or Mode III will eventually turn into a Mode I case. [32]

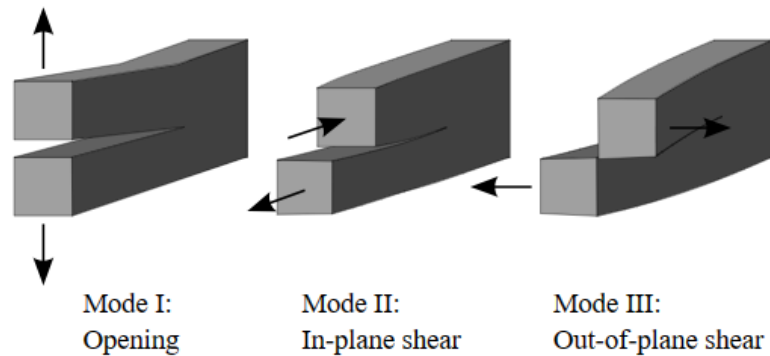


Figure 7: The primary fatigue modes [32]

### 2.3.4 Defect propagation

In the defect propagation phase, the focus will mainly be on the plasticity at the crack tip. The plasticity at the crack tip can be described with the stress intensity factor (SIF). The propagation phase can be divided into three phases: incubation, stable and crack-to-surface. The driving forces of the cracking process are shear stresses (mode II and mode III), fluid pressurization due to lubrication and fluid entrapment. Closure of the mouth sealed fluid to the crack is meant with fluid entrapment. The result of fluid entrapment is a fluid pressure which result in a high SIF at the tip of the crack. Fluid entrapment is linked to the severity of the crack propagation in the normal mode. The fluid pressurization is of concern, when the crack is started at the surface.

When modelling the defect propagation phase multiple things have to be taken into account which are the high stress location, the depth below the surface and the angle and direction of the crack inclination. The propagation phase last until the defect is completed and the material is removed from the surface, meaning that there is either spalling and or pitting. The completion of the defect can be measured with the length of the crack. When the crack reaches a pre-specified critical length, the defect will be completed. [14]

### 2.3.5 Damage growth

In the damage growth phase, instability stage, several changes happen which are a decrease in the yield stress due to material softening, increase in the volume of deformed subsurface, microstructure changes and increase in radial tensile strength. As spalling occurred, the rolling element can now make contact with the softer and rougher surfaces. The material will be softer, as the hardness declines with depth. As a result of the contact with softer and rougher surfaces, more stresses are generated and the defect will propagate faster to become wider and deeper.

Due to the rougher surface, it will become more likely to have adhesive and abrasive wear. In addition, the lubrication film will not be uniform anymore due to the spalling. Furthermore,

the impact of the rolling element will become larger, as the rolling element will hit a larger defected area. The particles, which originate from the first defect, are large and sharp in size and will act as stress raisers and as abrasive particles. All these wear factors will generate new defects in a similar way as discussed. Meaning that the crack opening and propagation in combination with over-rolling and abrasion will repeat until a new defect is completely removed and then it will start again to form a new defect. As shown in Figure 8, the damage growth will increase rapidly after the first defect is formed. [14]

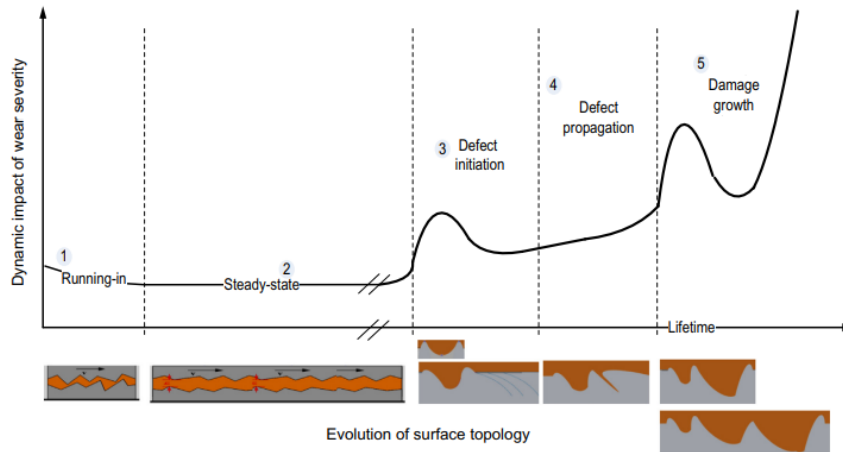


Figure 8: The different wear stages in the life of a roller bearing and their dynamic severity [14]

## 2.4 The Hertzian contact theory

The Hertz contact theory is used to model the contact stresses for rolling contacts. Research has shown that the pressure distribution of rolling contacts is quite similar to the Hertzian pressure distribution, especially for heavily loaded contacts [11]. The theory is relatively simple to use, as the resulting equations form the complicated mathematics are relatively simple. The simplicity of this theory still makes it one of the most widely used theories for calculating deformations, surface area and stresses occurring when two bodies make contact in simulations and calculations, even though it was the first theory to make this possible. [16]

### 2.4.1 Assumptions

For the use of the Hertz contact theory the following assumptions were made [11][3][16]:

1. The material of the contacting bodies is homogeneous, isotropic, non-conforming and elastic
2. The strains are small, meaning that the theory of elasticity is valid to be used
3. The contacting bodies are semi-infinite elastic half-spaces, meaning that the geometrical dimensions are way larger than the contact dimensions and deformations
4. The surfaces are smooth and frictionless
5. Adhesive forces are ignored
6. The curvature of the bodies is constant close to the contact area



The assumptions made in the Hertzian approach will not be completely true in reality, however these assumptions are close enough to be considered reasonable. For example, the assumption of the use of the elasticity theory may be breached for certain load cases. However, the amount of plasticity will be small and so the assumption is justified. Furthermore, the assumption of frictionless contact will not be completely true, as there will always be friction. However, for properly greased/oiled bearings this friction will be small and therefore the assumption is justified [12][30].

## 2.4.2 Contact area and pressure distribution

The type of contact surfaces will influence the pressure distribution on the surfaces. In general, the contact surfaces are modelled as an elliptical contact [54]. However, two special geometry cases are sphere-on-sphere and cylinder-on-cylinder contacts [36]. The elliptical and cylinder-on-cylinder contacts will be touched light on, as does two contact types will be important for the bearings.

The pressure distribution depends on the type of contact. In Figure 9, the pressure distribution of the contact cases for the elliptical contact (a) and the cylinder-on-cylinder contact (b) are shown. The sphere-on-sphere contact is a special form of the elliptical contact, where the major axis and the minor axes are equal to each other. Meaning that the resulting pressure distribution will be a sphere.

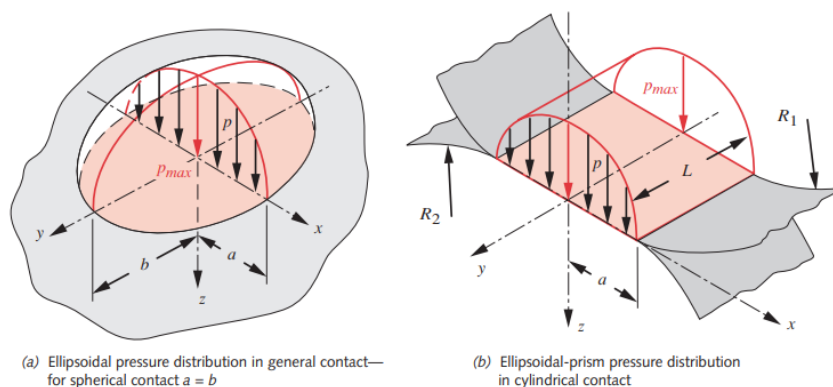


Figure 9: The pressure distributions for an elliptical and a cylinder-on-cylinder contact [36]

The major and minor axes depend on the applied load and the reduced elastic modulus for both contact types. The reduced elastic modulus, equation 1, slightly differs from the equation given in multiple textbooks [51]. However, the resulting answers for the dimensions and stresses will be the same as a different set of equations is used. For the remaining of the thesis, the major axis will be  $a_M$  and the minor axis will be  $b$ , instead of the used notation in Figure 9.

$$\frac{2}{E'} = \frac{1 - \nu_1^2}{E_1} + \frac{1 - \nu_2^2}{E_2} \quad (1)$$

The effective radius depends on the radius of the two contacting bodies, as shown in equation 2. The direction of the different radii are shown in Figure 10. For the cylinder-on-cylinder case, the effective radius will simplify to equation 3. For this case, however, there are three cases, as the bodies can be both convex, shown in Figure 9, one can be convex and one can be concave and one can be convex body contacting a flat surface. When the body is concave, its radius will be negative in equation 3. For the last case, the roller (body 1, convex) is contacting with a flat

surface (body 2), meaning that  $R_2$  is equal to zero in equation 3. [51][36]

$$\frac{1}{R_{eff}} = \frac{1}{R_{1x}} + \frac{1}{R_{1y}} + \frac{1}{R_{2x}} + \frac{1}{R_{2y}} \quad (2)$$

$$\frac{1}{R_{eff}} = \frac{1}{R_1} + \frac{1}{R_2} \quad (3)$$

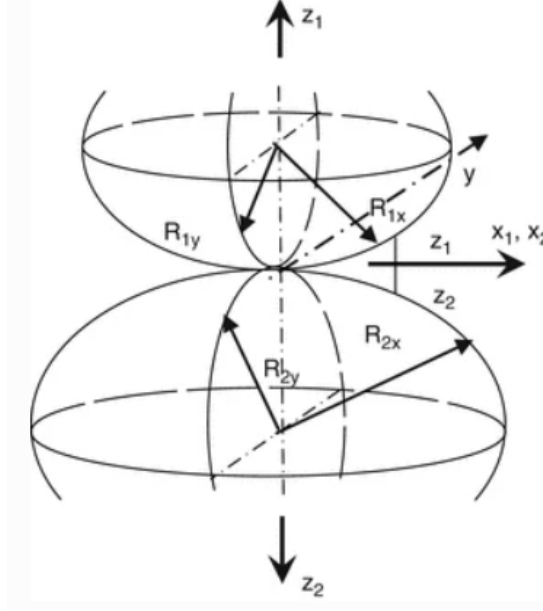


Figure 10: The directions of the radii of the ellipse [54]

The major and minor axis for an elliptical contact are given in equation 4, 5 respectively. Equations 6 - 10 are approximated equations. The  $R_x$  and  $R_y$  are the effective radii of x and y direction, the directions are shown in Figure 10. [51]

$$a_e = \alpha_e \sqrt[3]{\frac{3FR_{eff}}{E'}} \quad (4)$$

$$b_e = \beta \sqrt[3]{\frac{3FR_{eff}}{E'}} \quad (5)$$

$$\alpha_e \approx \kappa^{\frac{1}{3}} \sqrt[3]{\frac{2E_m(m)}{\pi}} \quad (6)$$

$$\beta \approx \kappa^{-\frac{2}{3}} \sqrt[3]{\frac{2E_m(m)}{\pi}} \quad (7)$$

$$E_m(m) \approx \frac{\pi}{2}(1-m) \left( 1 + \frac{2m}{\pi(1-m)} - \frac{1}{8} \ln(1-m) \right) \quad (8)$$

$$m = 1 - \kappa^2 \quad (9)$$

$$\kappa \approx \left( 1 + \sqrt{\frac{\ln(\frac{16}{\lambda})}{2\lambda}} - \sqrt{\ln(4) + 0.16\ln(\lambda)} \right)^{-1} \quad (10)$$

$$\lambda = \frac{R_x}{R_y}, \quad 0 < \lambda < 1 \quad (11)$$

The mean and max pressure distribution can be calculated with the major and minor axis of the ellipse and the contact force (F) as shown in equations 12, 13 respectively. [51][36]

$$P_{e,mean} = \frac{F}{\pi a_e b_e} \quad (12)$$

$$P_{e,max} = \frac{3}{2} P_{e,mean} = \frac{3F}{2\pi a_e b_e} \quad (13)$$

For the cylinder-on-cylinder contact, the contact area depends on the width of the cylinder and the contact-patch half-width. The contact-patch half width can be calculated with equation 14. [51]

$$a_c = 2\sqrt{\frac{2FR_{eff}}{\pi LE'}} \quad (14)$$

The resulting mean and max pressure for the cylinder-on-cylinder contact can be calculated with equations 15 and 16, respectively.

$$P_{c,mean} = \frac{F}{2La_c} \quad (15)$$

$$P_{c,max} = \frac{4P_{c,mean}}{\pi} = \frac{2F}{\pi La_c} \quad (16)$$

The pressure at a certain point can be calculated with equation 17. For the cylinder-on-cylinder contact case the minor axes,  $b$ , is zero and the pressure will be uniform in the width of the cylinder as shown in Figure 9. [36]

$$p(x, y) = P_{max} \sqrt{1 - \frac{x^2}{a^2} - \frac{y^2}{b^2}} \quad , x \leq a, y \leq b \quad (17)$$

### 2.4.3 Stresses in material

Stress fields are created in the material due to the applied load. The stress field can be explained with the von Mises stress and the maximum shear stress. The maximum shear stress can be calculated with the Tresca stress equation, equation 18, and the von Mises stress can be calculated with equation 19. [16]

$$\tau_{max} = \frac{\sigma_x - \sigma_z}{2} = \frac{\sigma_y - \sigma_z}{2} \quad (18)$$

$$\sigma_{vM} = \sqrt{\frac{(\sigma_x - \sigma_y)^2 + (\sigma_x - \sigma_z)^2 + (\sigma_y - \sigma_z)^2}{2}} \quad (19)$$

The maximum for the shear stress and the von Mises stress do not happen at the same depth in the material, as shown in Figure 11. The figure is for two cylinders in static contact or in pure rolling. The maximum normal stresses occur at the surface of the material, while the maximum shear stress happens at a certain depth in the material.

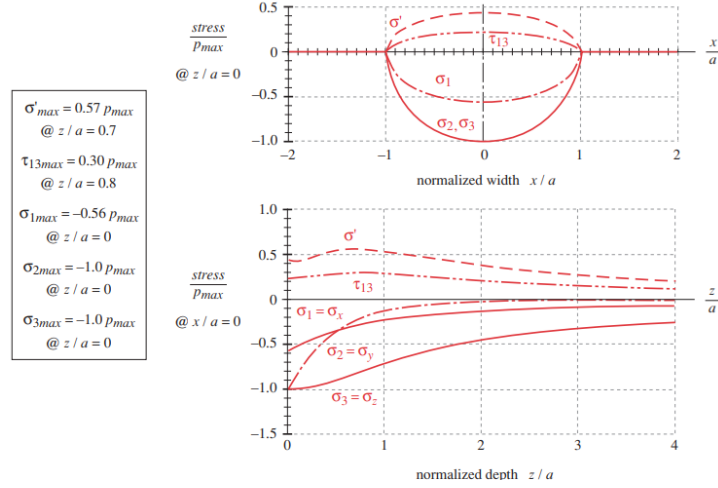


Figure 11: The stresses in the material [36]

The depth at which the maximum shear stress happens depends on multiple things. The first is the contact between the two bodies, whether it is a point or line contact. For a point contact, it will depend on the elliptical ratio  $K_e = b_e/a_e$  and the maximum pressure, as shown in table 2 [16]. While for a line contact, the maximum shear stress only depends on the  $a_c$ , being  $z_{@ \tau_{max}} = 0.786 a_c$ . The combination of the Mohr's circle stresses ( $\sigma_x$  and  $\sigma_z$ ) result in a maximum shear stress ( $\tau_{13}$ ). For two cylinders in static contact, the maximum shear stress is equal to equation 20. [36]

$$\tau_{13max} = 0.304 P_{max} \quad (20)$$

Table 2: The maximum Tresca and von Mises stresses [16]

Ellipticity $K_e$	$\tau_{max}$		$\sigma_{vM}$	
	$\tau_{max}/P_{max}$	at $z/a_e$	$\sigma_{vM}/P_{max}$	at $z/a_e$
0.2	0.321	0.149	0.586	0.142
0.4	0.325	0.266	0.605	0.260
0.6	0.322	0.355	0.615	0.355
0.8	0.316	0.425	0.619	0.425
1.00	0.310	0.480	0.620	0.480
1.25	0.316	0.531	0.619	0.531
1.67	0.322	0.592	0.615	0.591
2.50	0.325	0.665	0.605	0.650
5	0.321	0.745	0.586	0.708
Infinity	0.302	0.785	0.558	0.703

#### 2.4.4 Line contact versus point contact

In the previous sections, the stresses and loads for the different types of contacts are explained. The elliptical contact can be considered as a point contact, where the cylinder-on-cylinder contact is considered to be a line contact [52].

In van den Ende, 2021, it is stated that an elliptical shape results from the contact of a wheel and the rails. Meaning that van den Ende used an elliptical/point contact to model the contact [16]. For ball bearings, the use of an elliptical/point contact is valid [52].

For roller bearings, a cylindrical/line contact is expected. As the roller can be seen as a cylinder. However, the wheel used by van den Ende can also be seen as a cylinder. So, the assumption of van den Ende was tested for rollers, as shown in Figure 12. The test case consist of a roller which has a diameter of 75 mm and and a width of 75 mm.

The contact pressure of the point contact is lower for higher loads compared to the contact pressure of the line contact, as shown in Figure 12. However, as the load increases the contact pressure of the line contact becomes larger than the contact pressure of the point contact.

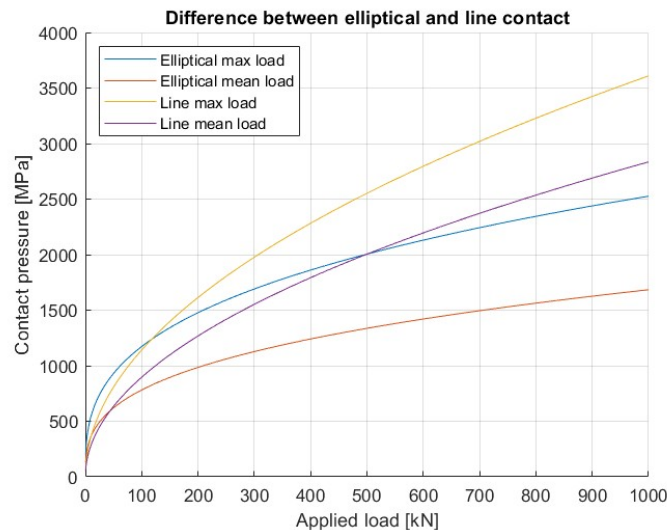


Figure 12: Contact pressure for a line and point contact

Furthermore, from Figure 13, it can be seen that the contact width of the elliptical contact becomes larger than the width of the cylinder. This increase of width can also become larger than the width of both contacting bodies, which is physically not possible. To avoid this problem, for the remaining of thesis a line contact will be used to model the roller contact.

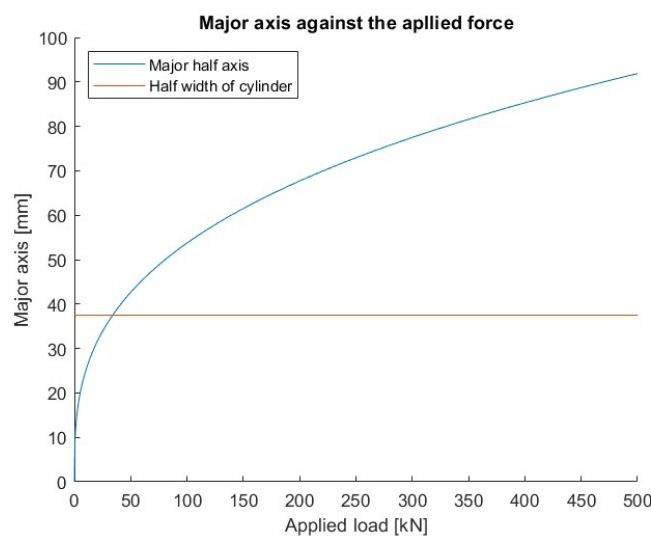


Figure 13: The contact width of a point contact

## 2.5 Lifetime predicting models

There are several different lifetime predicting models for bearings, which are:

1. Basic rating life
2. Miner's rule
3. Damage mechanics
4. Fracture mechanics

The basic rating life indicates the number of cycles that the first incidence of fatigue pit formation forms at any of the rolling surfaces [22][17]. Both the Miner's rule and the damage mechanics make use of a damage fraction. For the Miner's rule, the damage fraction is based on the calculated fatigue cycles limit and the cycles the bearing has done [13]. The fatigue cycles can be determined from the S-N curve or for instance by making use of the described methods by van den Ende, 2021 [46][16]. These methods are FEM 1.001 b4/ ISO 16881-1, EN 13001-3-3 and Horowitz. For the damage mechanics, the damage fraction is based on the effective area of the defect [27][26][47].

The lifetime prediction in this thesis will be based on fracture mechanics. The fracture mechanics will be explained in the remaining of this section.

### 2.5.1 Fracture mechanics

As stated in section 2.3, the crack can originate from the surface and subsurface. Furthermore, the SIF will affect the crack growth. According to van den Ende, 2021, the SIF will be larger for the subsurface originated crack than the surface originated crack [16]. Therefore, only the subsurface crack methodology will be discussed.

#### Stress intensity factor

The SIF, is a linear elastic parameter, shown in equation 21 as  $K$ , which is used in fracture mechanics for analyzing the fatigue crack growth. The object has failed when the SIF is larger or equal to the critical fracture toughness of the material. [16]

The SIF can be calculated with equation 21. The  $Y$  is geometry factor which takes the geometry of the crack, loading configuration and geometry of the part into account. Furthermore,  $a$  is the crack length and  $\sigma_c$  the compressive stress. [32][16]

$$K = Y\sigma_c\sqrt{\pi a} \quad (21)$$

The general equation for the SIF, equation 21, assumes that the crack is perpendicular to the surfaces. Meaning that the effect of the angle of the crack is not taken into account. To take this effect into account the shear stress is used instead of the compressive stress.

In addition, for the SIF only mode II is considered, as the bearing will be primarily be loaded in compression. Meaning that due to this loading mode I will be closed, as shown in Figure 7. Due to the closing of the crack in compression, the friction between the crack faces will be important. So, the effective shear stress will be used. The effective shear stress takes the resulting frictional stress into account, as shown in equation 22. [16]

$$\tau_{se} = \tau - k \sigma_n = \sigma_c \sin(\theta)(\cos(\theta) - k \sin(\theta)) = \tau - \sigma_c k \sin^2(\theta) \quad (22)$$

The resulting SIF, equation 23, is based on the maximum effective shear stress.

$$K = Y\tau_{semax}\sqrt{\pi a} \quad (23)$$

The maximum effective shear stress results from the maximum shear stress. The maximum shear stress will be for an angle of 45 degrees compared to the surface where the normal stress is acting on it, according to the Mohr's circle [15]. Additionally, the depth is also important, as discussed earlier the maximum shear stress will be below the surface. As a result, the compressive strength will be less at that depth, as shown in Figure 11. The compressive strength can be calculated with equations 24 - 26 for an elliptical contact. The maximum pressure in equation 24 is based on the Hertz contact theory as discussed in section 2.4. Furthermore, equation 26 is a curve fit of the table 2. For the cylindrical case, the effective contact length,  $c_e$ , will simply be equal to the contact half width of the cylindrical contact,  $a_c$ . In addition, the maximum shear depth will be equal to  $0.786a_c$ . [16]

$$\sigma_c = \frac{-P_{max}}{1 + \frac{z^2}{c_e^2}} \quad (24)$$

$$\frac{1}{c_e} = \frac{1}{a_e} + \frac{1}{b_e} \quad (25)$$

$$z \approx b_e \left( 0.7929 - 0.3207 \frac{a_e}{b_e} \right) \quad (26)$$

## Crack growth

In Figure 14, the crack growth over the number of cycles is shown. The crack growth rate ( $da/dN$ ) is small in the beginning. However, as the crack increases the growth rate will increase exponentially. The failure occurs when the crack has reached its critical length  $a_c$  after  $N_f$  number of cycles. The critical length is reached when the SIF is equal to the fracture toughness, as shown in Figure 15.

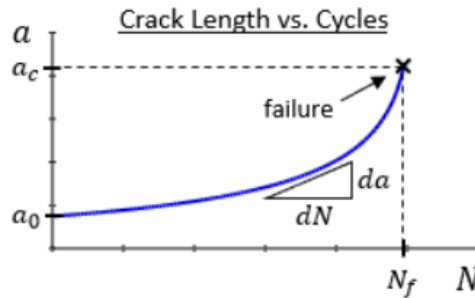


Figure 14: The crack size against the number of cycles [31]

As shown in Figure 15, the crack growth rate can be divided into three stage. In stage I, the crack growth rate is related to non-continuum mechanisms. The process is driven by [37]:

1. Grain size, precipitates, dislocation density, etc.
2. Mean stress and stress ratio
3. The environment
4. Surface damage initiation

Stage II is typically a straight line on a log-log plot of the crack growth rate and the stress intensity range. This line is often referred to as the Paris curve [31]. During this stage, beach marks and striations begin to form. Striations are microscopic fatigue characteristics. Furthermore, the progression of a stress cycle is indicated by a striation. The parameters of the Paris model will slightly depend on the parameters of stage I. In addition, the crack growth rate depends on the geometry and the load history, resulting in enhanced or delayed growth rates. [37]

In stage III, the crack growth rate will start to grow exponentially and as a result the material will eventually fail. The crack growth rate is high, due to the high SIF. This stage is often called the instability region. This stage depends on the same microstructural parameters as cited in stage I and the thickness of the specimen. [37]

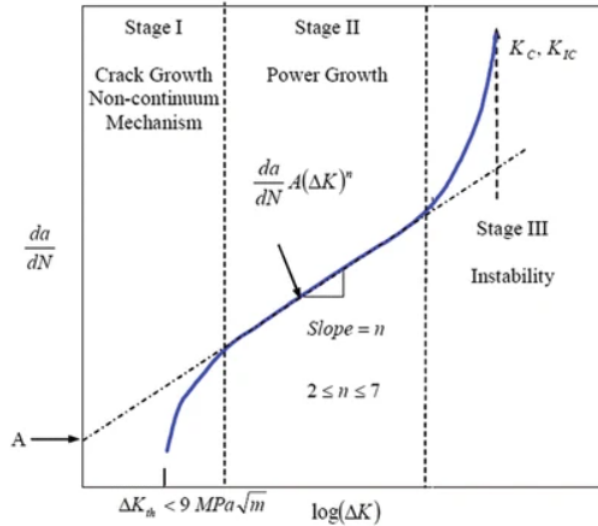


Figure 15: The crack growth rate against the stress intensity range [37]

The crack growth rate can be described with different equations. The general equation for the crack growth rate is the Paris model, equation 27, which describes stage II of the growth rate [37][31]. The  $C$  is the intercept constant, in Figure 15 the  $A$ . The  $n$  is the slope of the straight line of stage II. The  $n$  ranges from 2 to 8 or 9, but can be assumed to be 3 for steels [16].

$$\frac{da}{dN} = C (\Delta K)^n \quad (27)$$

In the Paris model, the stress ratio is not taken into account. However, the stress ratio,  $R$ , does affect the crack growth rate, as shown in Figure 16. In the Walker equation, equation 28, the stress ratio is taken into account. The  $\gamma$  is a material constant which indicates how strongly the crack growth rate depends on the stress ratio. For steels this value is often equal to 0.5, but can vary between 0.3 and 1. [31]

$$\frac{da}{dN} = C \left( \frac{1}{(1-R)^{1-\gamma}} \Delta K \right)^n \quad (28)$$



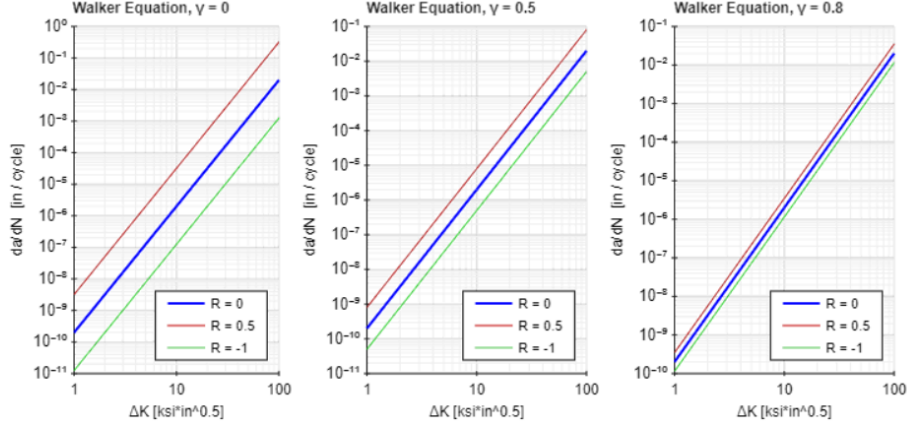


Figure 16: The effect of the stress ratio and the material constant  $\gamma$  [31]

In both the Paris model and the Walker model the effects of stage I and stage III are not taken into account. The NASGRO model, equation 29, takes these effects into account and also the crack closure effect. The  $p_N$  and  $q_N$  are coefficients that determine the growth rate in stage I and III, respectively. The  $\Delta K_{th}$  is the threshold SIF, which indicates when the growth rate will start to grow as shown in Figure 15. The critical SIF ( $K_c$ ) is the fracture toughness of the material. The  $f$  is the Newman crack closure function. [31]

$$\frac{da}{dN} = C \left( \left( \frac{1-f}{1-R} \right) \Delta K \right)^n \frac{\left( 1 - \frac{\Delta K_{th}}{\Delta K} \right)^{p_N}}{\left( 1 - \frac{K_{max}}{K_c} \right)^{q_N}} \quad (29)$$

The Newman crack closure function can be calculated with equation 30. The polynomial coefficients are given by equation 31. The  $\sigma_{max}$  is the maximum stress and  $S_{fl}$  the material flow strength. The material flow strength is the average of the ultimate and yield strength. The ratio between the maximum stress and material flow strength ( $\sigma_{max}/S_{fl}$ ) is in general 0.3 when using the NASGRO model. The plane stress/strain constraint factor ( $\alpha$ ) is 1 for plane stress conditions and for pure plain strain  $\alpha = \frac{1}{1-2\nu}$ , where  $\nu$  is the Poisson's ratio. [33][56]

$$f = \begin{cases} \max(R, A_0 + A_1 R + A_2 R^2 + A_3 R^3) & R \geq 0 \\ A_0 + A_1 R & -2 \leq R < 0 \end{cases} \quad (30)$$

$$\begin{cases} A_0 = (0.825 - 0.34\alpha + 0.05\alpha^2) \left( \cos \left( \frac{\pi \sigma_{max}}{2S_{fl}} \right) \right)^{\frac{1}{\alpha}} \\ A_1 = (0.415 - 0.071\alpha) \frac{\sigma_{max}}{S_{fl}} \\ A_2 = 1 - A_0 - A_1 - A_3 \\ A_3 = 2A_0 + A_1 - 1 \end{cases} \quad (31)$$

In the remaining part of this thesis, the Paris model will be used. The model will be used as it one of the most widely used models for the high cycle fatigue. However, even tough this model has its shortcomings, it does not take into account, for example, the plasticity which will impact the fatigue life.

## 2.6 Acoustic emission monitoring

Acoustic emission (AE) monitoring is an inspection method, where defects in the material are detected due to the release of ultrasonic stress waves. These stress waves originate from within the material itself and are not from external sources. AE monitoring is an useful and commonly used method for non-destructive testing. The advantage of using AE monitoring to collect data is that AE monitoring is a non-destructive testing method, so the test does not damage the material. [41]

The monitoring of the degradation in REBs can be done with several techniques such as lubrication analysis, strain and vibration monitoring, temperature monitoring, electrostatic monitoring and acoustic monitoring. Traditionally, strain and vibration monitoring is used in practice and research. Possible defects or imbalances are detected by changes in the dynamic structural response of the REB. Meaning, that strain and vibration monitoring is suitable for high speed bearings. However, for low speed this method will not be suitable due to the limited change in the structural response. For low speed, AE monitoring has shown good potential in previous research. [43]

AE signals are generated when a material, which is damaged or has defects, is under stress, this can be from a heavy load and/or from stresses induced due to temperature [41]. There are several different source which can generated AE signals, these are [23]:

1. Initiation/growth of cracks
2. Yielding
3. Bond and/or fiber failure
4. Delamination in composites

The AE signals can be measured, when the measured signal crosses the set threshold the signal will be taken into account for the monitoring. From these signals, multiple AE parameters can be derived, as shown in Figure 17. The counts of the waveform, is the amount of times the waveform crosses the set threshold. The duration of the signal is the time between the first and the last threshold crossing of the waveform. The risetime is the time it takes from the first threshold crossing to the amplitude (maximum of the waveform) of the waveform. The energy of the signal is defined as the area under the waveform and above the threshold. [45]

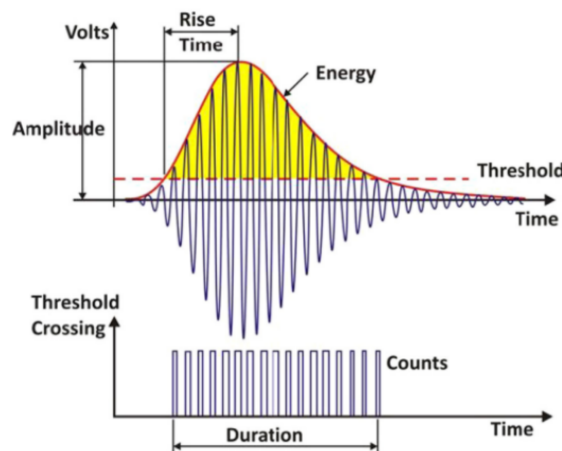


Figure 17: Acoustic emission parameters [47]

The condition of the REB can be estimated with the bearing condition index (BCI), equation 32. The BCI is derived from the sum of all the identified AE signal  $c_{k,q_i}$ , the signals which crossed the threshold, in the load cycles  $dN$ . Furthermore,  $K_s$  are the considered source mechanisms and  $Q$  the implemented sensor types. The  $k$  and  $q_i$  are the indices of these respectively.  $C_B$  can have an interval of (0,1], where the value of 1 indicates a pristine bearing and 0 a severely worn bearing. [43]

$$C_B = \frac{1}{1 + \sum_{q_i=1}^Q \sum_{k=1}^{K_s} \alpha_q \alpha_k \frac{dc_{k,q_i}}{dN}} \quad (32)$$

### 2.6.1 Acoustic emission based fracture model

Several researchers have shown that a relation exists between the fatigue crack growth behavior and the resulting AE. Several features of the AE signal are stochastically correlated with important fracture mechanics parameters, such as  $\Delta K$  and  $\frac{da}{dN}$ . The relation is similar to the Paris model shown in equation 27. For the AE relation the feature of the signal is correlated to  $\Delta K$ , as shown in equation 33. [6][8][9][18][24][29][38][40][45][55]

$$\frac{dParameter}{dN} = B (\Delta K)^p \quad (33)$$

The  $\frac{dParameter}{dN}$  is the rate of the used AE feature. The  $B$  is similar to the intercept constant  $C$  of the Paris model. The  $p$  is related to the slope constant  $n$  of the Paris model. Theoretically,  $p$  is equal to  $n + 2$ . However, due to the signal attenuation and the used filtering and settings of the system, the value of  $p$  will vary from this [45].

In the several researches, several different features of the AE were used to capture the behavior between the AE and the fracture mechanics parameters. The used features are:

1. Counts
2. Duration
3. Amplitude
4. Energy
5. Hits
6. Entropy

In most cases, the energy and counts were used. An example of the relation between the AE and the fracture mechanics of these two features is shown in Figure 18. In this thesis, the counts and hits will be used for the AE based fracture model. Since the hits are an important input for the BCI and the counts are closely related to the hits. [6][8][9][18][24][29][38][40][45][55]

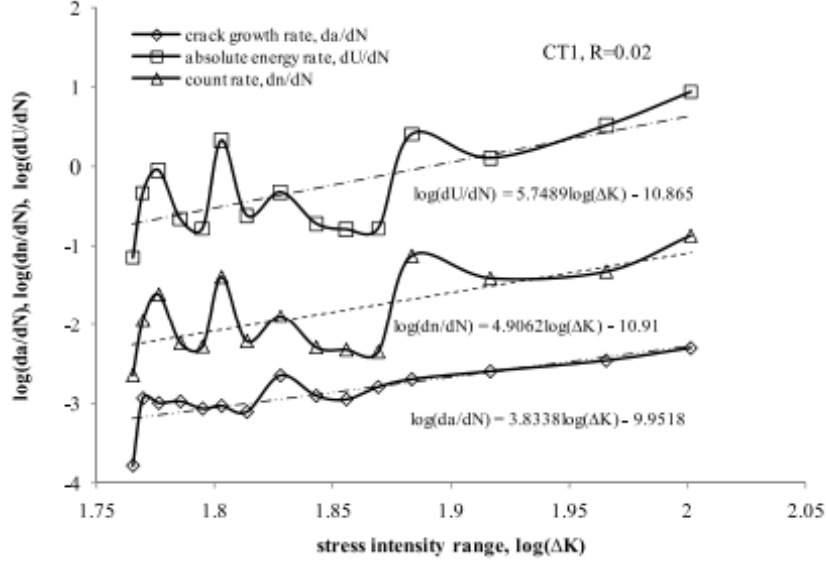


Figure 18: An example of the relation between acoustic emission and the fracture parameters [55]

The rate equation, equation 33, for the used emission parameter depends on the SIF. However, the rate of the counts/hits is measured and the SIF is one of the important properties to be calculated. So, by rewriting equation 33 to the form shown in equation 34, the SIF can be calculated based on the rate of the emission parameter.

In addition, by combining the Paris model, equation 27, and equation 34 an equation for the crack growth rate can be established. This equation is shown in equation 35. The  $D$  and  $q$  are newly introduced constants to simplify the equation.

$$\Delta K = \left(\frac{1}{B}\right)^{\frac{1}{p}} \left(\frac{dParameter}{dN}\right)^{\frac{1}{p}} \quad (34)$$

$$\frac{da}{dN} = C \left(\left(\frac{1}{B}\right)^{\frac{1}{p}} \left(\frac{dParameter}{dN}\right)^{\frac{1}{p}}\right)^n = \frac{C}{B^{\frac{n}{p}}} \left(\frac{dParameter}{dN}\right)^{\frac{n}{p}} = D \left(\frac{dParameter}{dN}\right)^q \quad (35)$$

The counts will be derived from the measured hits by using equation 36. Here the hits are multiplied with the factor  $c_{ave}$ . This factor takes two things into account, which are the length of the signal and the used sensor. The values of the  $c_{ave}$  are obtained by multiplying the length of the signal with the fundamental frequency of the sensor. In this thesis, three different sensors were used for the AE which are  $R6\alpha$ ,  $R15\alpha$  and  $WS\alpha$ , these are the same sensors used by B. Scheeren. The fundamental frequency of these sensors are  $60\text{ kHz}$ ,  $150\text{ kHz}$  and  $400\text{--}450\text{ kHz}$ , respectively. For the  $WS\alpha$ , a fundamental frequency of  $450\text{ kHz}$  will be used.

During this thesis a signal length of  $200\text{ }\mu\text{s}$  will be used for the  $c_{ave}$ . This length was chosen based on the obtained data by B. Scheeren and on Figure 19. Furthermore, (Rabiei & Modarres, 2013) stated that the signals related directly correlated to crack growth are the signals close to the maximum or peak load [38]. In addition, (Roberts & Talebzadeh, 2003a) stated that crack propagation is only related to the loading part of a loading cycle [40]. Meaning that an average value for the counts will be used during this thesis. In addition, the hits and counts will be averaged over the used sensors. The  $\alpha_q$  is used for this averaging. The values for the  $\alpha_q$  are shown in equation 37, these are for the  $R6\alpha$ ,  $R15\alpha$  and  $WS\alpha$ , respectively [43].

$$c = c_{ave}H, \quad c_{ave} = \begin{bmatrix} 12 \\ 30 \\ 90 \end{bmatrix} \quad (36)$$

$$\alpha_q = \begin{bmatrix} 1 \\ 3 \\ 1 \\ 3 \\ 3 \end{bmatrix} \quad (37)$$

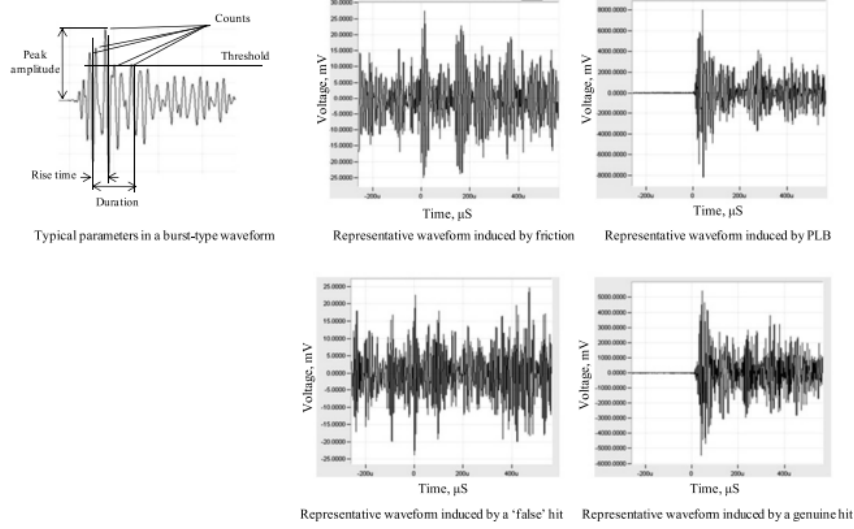


Figure 19: An example of different types of hits [55]

## 2.6.2 Parameters for acoustic emission based fracture model

As stated earlier, the slope parameter  $p$  depends on the slope parameter  $n$  of the Paris model, where  $p$  is theoretically equal to  $n + 2$ . In practise, this value will not be obtained, due to attenuation and filtering of the AE signals which are the result of inaccuracies in the measurement and processing of the data. Based on the results of (Roberts & Talebzadeh, 2003a) and (Yu et al., 2011a), which were for a S275 JR steel plate and ASTM A572 G50, respectively, it was opted to use  $p = n + 1$  instead [40][55].

For the intercept constant  $B$ , only limited information was available. Unfortunately, no information was found for the bearing steels used for this thesis. Meaning that an estimated guess needed to be made based on the available data. The estimated guess was based on the fitted values for  $B$  and  $C$  by (Yu et al., 2011a). In Figure 20, a scatterplot is shown of the intercept constant  $B$  against the Paris model intercept constant  $C$ . With the obtained data points, a trendline was made and with this trendline an estimated guess could be made for the intercept constant  $B$ .

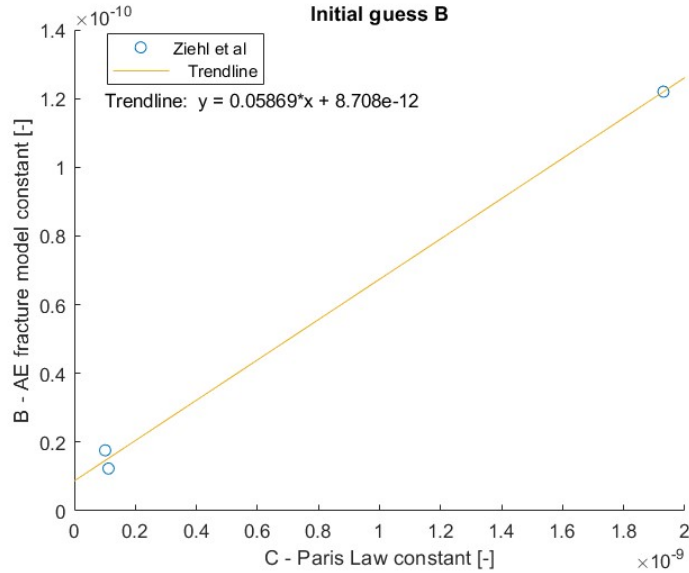


Figure 20: Data points for initial guess of  $B$  [55]

In table 3, the values used for the AE fracture model are shown. The values B. van den Ende used during his thesis for the Paris model will also be used during this thesis [16].

Table 3: Used parameter values for Paris model and acoustic emission model

Parameter	Value
$C$	$5.21 \cdot 10^{-13}$
$n$	3
$B$	$3.11 \cdot 10^{-13}$
$p$	4
$D$	$1.25 \cdot 10^{-3}$
$q$	0.75

## 2.7 Remaining useful life

The remaining useful life (RUL) of an object is a way to estimate the lifetime an object has until it will fail. The RUL estimation is based on the health of the object, the usage of the object and the future use of the object. When the object is no longer able to function properly, due to the degradation and/or a critical failure, the RUL of the object is reached. [1]

The RUL will be based on the Paris model, the AE-based fracture model and a Miner's rule-based formula. As stated, the RUL depends on the health, the usage and the future use of the object.

The usage of the object, in this case the bearing, will be captured via the link between the physical and virtual bearing. This link is in the form of data transport. The usage is estimated based on the force acting on the bearing, based on strain gauge values, the rotation of the bearing and the measured AE.

By using the Paris model and the AE-based model, the current state of the bearing can be calculated.

For the future use, an assumption is made. Which is that the future use can be estimated based on the average force.

The total number of load cycles the bearing can do until the bearing fails can be calculated with the Paris model. The failure of the bearing is assumed to happen when the fracture limit of the material is reached. By combining this assumption with the assumption for the future use and equation 23, the critical crack length can be calculated for the bearing, equation 38. The critical length will play a key part in estimating the number of load cycles the bearing has left. Since the Paris model describes the relation between the SIF and the crack growth rate.

The SIF is equal to the fracture limit when the bearing fails. So, by integrating the Paris model, equation 27, the total number of load cycles to failure can be calculated. The resulting equation for the number of load cycles to failure is shown in equation 39. For the full derivation see Appendix A - Derivation total number of load cycles to failure equation. In this equation, the  $N$  are the total number of load cycles to failure the bearing has done until the last data point and  $a$  the resulting crack length for the last data point. [37]

$$a_f = \frac{1}{\pi} \left( \frac{K_c}{\Delta\tau_{se}} \right)^2 \quad (38)$$

$$N_f = \left[ \frac{1}{C (\Delta\tau_{se})^n \pi^{\frac{n}{2}}} \left( \frac{-2}{n-2} \right) a^{-\frac{n}{2}+1} \right]_a^{a_f} + N \quad (39)$$

The RUL based on the Paris model and the AE model give the RUL in the number of load cycles. However, this value will not reflect the health of the bearing well. As a result, the RUL will be based on the linear damage rule proposed by Palmer and Miner. The Palmer-Miner's rule, commonly called the Miner's, is shown in equation 40. The Miner's rule uses the  $N_M$  number of load cycles an object can do subjected to a specific load and the number of load cycles done on that load level  $n_i$ . [13]

$$D_M = \sum \frac{n_i}{N_M} \quad (40)$$

For the RUL based on the Miner's rule three different forms will be used. These three forms are shown in equation 41, 42 and 43. The three different forms are used to investigate the influence of using the crack length, the remaining number of load cycles left and the difference in using a linear and quadratic form. In 5.1.5 Remaining useful life, the three different RUL forms will be compared to each other.

$$RUL = 1 - \frac{a}{a_f} \quad (41)$$

$$RUL = 1 - \frac{N}{N_f} \quad (42)$$

$$RUL = 1 - \left( \frac{N}{N_f} \right)^2 \quad (43)$$

# 3 Methodology

In this section the methodology of the DT for making the RUL prediction of the bearing is explained. The roadmap of the procedure is shown in Figure 23.

## 3.1 Input data

For the DT, input data is needed to make the RUL predictions. The input data consists of multiple different input files. These input files can be divided into two groups, which are the old data files and new data files.

The old data is data that is already been used for making the RUL predictions. In order to reduce the computational burden of the DT, the predictions are saved as MATLAB Data files. By saving the predictions, the DT only has to load those files instead of computing it every time. The old files consist of multiple different parameters which are: the position of the rollers, the force history acting on the bearing, the number of load cycles done, the SIF and the crack length.

The new data is the data that still has to be processed by the DT. The new data consists of multiple parameters which are: the rotations of the turret, the force acting on the bearing and the AE data.

The new data first needs to be converted and/or filtered. The data that is collected by the Aoka Mizu is in a file format that cannot be used directly by the DT. By using an inhouse code for reading the data, the data can be converted to a MATLAB Data file which can be used by the DT.

The force acting on the bearing also has to be filtered. As without filtering the resulting force is way to larger. The strain is measured at eight different sensor locations. The strains will be detrended, which will be used for calculating the force acting on the bearing.

The AE needs to be filtered first before the AE can be used. The filtering is used to get rid of background noise, which is not related to the failure/degradation of the bearing. The same filtering will be used as the one described by B. Scheeren in [43].

## 3.2 Determining load cycles

The bearing is divided into a number of grid cells. An example of the grid cell configuration for 16 cells is shown in Figure 21. The grid cell is as wide as the difference between the inner and outer diameter of the bearing. This width is used as a result of the assumption that the load is constant in the width direction, as a line load is used. The bearing will be divided into 1080 grid cells. For the load cycles done in the time frame of the data, two important things are needed; the position of the rollers and the rotations done in the time frame.



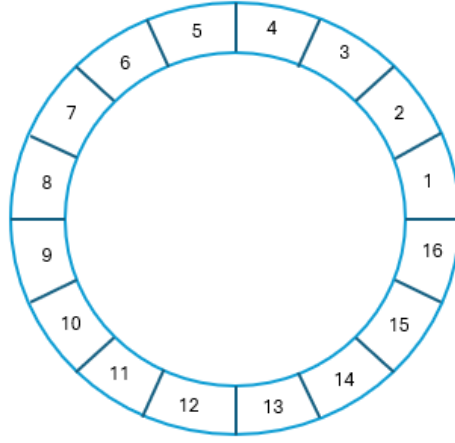


Figure 21: An example of the shape of the grid cells and how they are counted

The position of the rollers is difficult to know, as the starting position of the rollers is not known. Therefore, two assumptions for the position of the rollers were made. Being that the rollers have the same distance between them, which can be calculated with equation 44. In addition, the first roller starts in the first grid cell. Based on these assumptions, the starting position of the rollers is now known.

$$\Theta_r = \frac{2\pi}{Z} \quad (44)$$

As the ship rotates, the main bearing will also rotate meaning that the rollers will move to a new location. Based on the input data, the new location for every roller can be calculated simply by adding the difference in angle to the location of the previous location. An example of this movement is shown in Figure 22.

As the rollers move from one location to another, it passes over certain grid cells. By counting the number of times the rollers roll over one specific grid cell between the old location to the new location, the number of load cycles for moving to the new location is determined. In Figure 22, the old location is shown in black and the new location in red.

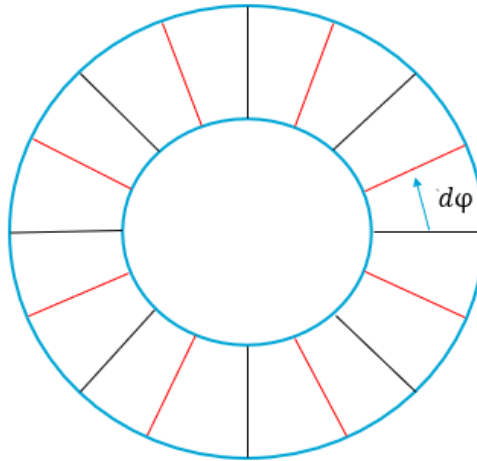


Figure 22: The movement of the rollers from their old location to their new location

### 3.3 Force on grid cell

The force on the bearing is measured at eight different sensor location, by measuring the strains. Each strain is converted into a force and multiplied with  $\frac{8}{Z}$ . The  $Z$  is the number of rollers the bearing has and the 8 is due to the fact that the force is measured at eight different locations around the circumference of the bearing.

By interpolating the force from one sensor location up to the next sensor location, the force acting on all grid cells can be determined. This is necessary as each grid cell is loaded in the timestep taken.

### 3.4 Stresses

Based on the distributed force over the grid cells, the stresses in the material can be determined. To be able to calculate the shear and normal stresses in the material, the Hertzian contact pressure is needed. The Hertzian contact pressure can be calculated with equation 14 and 16.

The normal and shear stresses both depend on the Hertzian contact pressure. The shear stress in the material can be calculated with equation 20. While the normal stress in the material can be calculated with equation 14 and 24 in combination with the depth of the maximum shear stress.

### 3.5 Fracture

The SIF will be based on both the Paris model, equation 23 and the AE model, equation 34. The SIF will be averaged over both models. Meaning that both models first calculate their SIF. These SIFs will then be averaged by using equation 45. When there is no AE data, the SIF will only be based on the Paris model.

$$\Delta K_{avg} = \frac{\Delta K_P}{2} + \frac{\Delta K_{AE}}{2} \quad (45)$$

As the SIF is now known, equation 27 can be used to calculate the new crack rate. The new crack size can be calculated with equation 46. Meaning that the crack growth rate is based on the averaged SIF. With the new crack size, for the Paris model, the SIF for the next data point can be calculated. Furthermore, the number of load cycles will be updated with equation 47. If the next point is still in the new data file, the loop will continue. However, when the next point is outside the new data file, the loop will be stopped and will go to the RUL prediction, as shown in the roadmap in Figure 23. The RUL prediction is only made when the SIF is still below the fracture limit and thus the bearing still has a RUL.

$$a_{i+1} = a_i + \Delta a \quad (46)$$

$$N_{i+1} = N_i + \Delta N \quad (47)$$



## 4 Linear bearing test

The results obtained for section 5.1 Linear bearing test are based on the data obtained from a linear bearing test done by Huisman Equipment. The test setup is shown in Figure 24. During the test, two linear bearings are subjected to fatigue damage. These bearings are positioned below and above the traveller. The bearing under the traveller had already reached its theoretical lifetime before the test started.

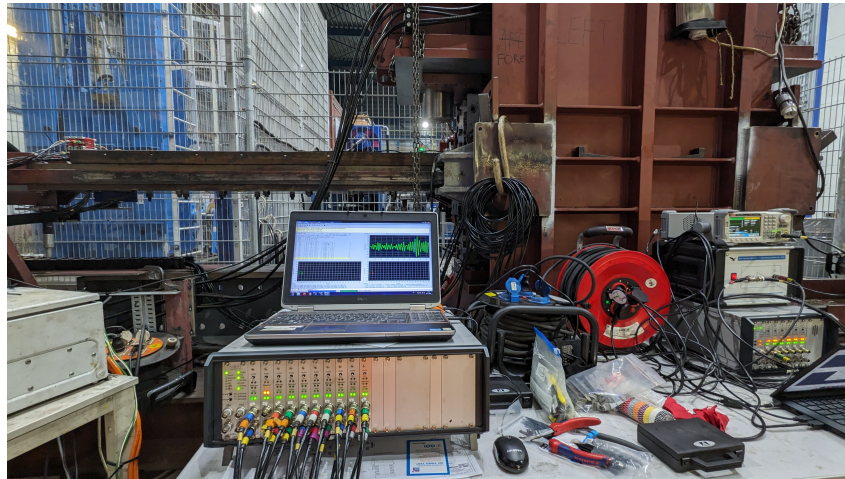


Figure 24: The test set-up for the linear bearing test done by Huisman Equipment

During the fatigue test, the AE is monitored. The monitoring was done at six different locations, shown in Figure 25. Each sensor location is depicted in yellow, the grey bar is the traveller and the red blocks contain the bearings. At each location, three different sensors were placed, which are the  $R6\alpha$ ,  $R15\alpha$  and  $WS\alpha$ . The sensor location of sensors A and B are varied between two locations during the test. These are on the side and on top of the traveller.

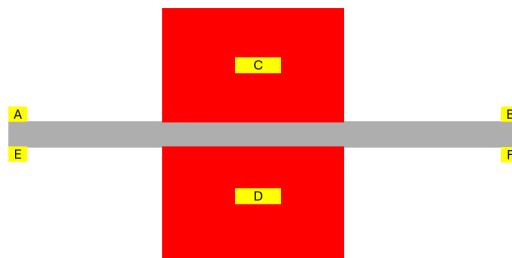


Figure 25: The six different sensor locations

In addition, the grease condition of the bearing and the velocity of the traveller is changed. The grease condition is varied between three different conditions, which is for bad grease conditions up to fully flashed clean grease conditions. The second condition is in between those two conditions. The velocity of the traveller varied between three different velocities.

In Figure 26, an example for the best grease condition and fastest velocity of the traveller is shown. Each test is divided into seven different blocks, shown as L1 up to L7. Where each block depicts the load level which is acting on the bearings. The load level L1 is the lowest load level and during the test the load is thus increased. The values of the different load levels are shown in table 4.

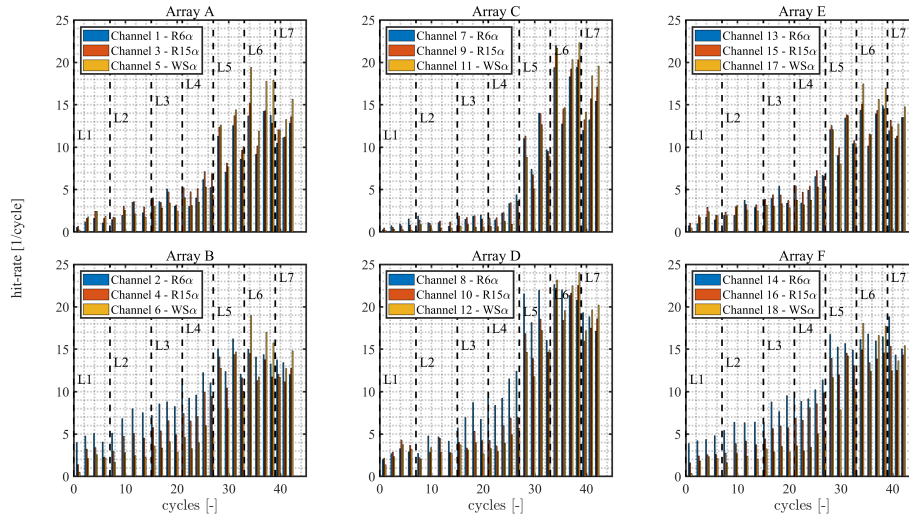


Figure 26: The hit-rates for the test 3-1-3

Table 4: The values for the different load levels

Load level	Value ( $kN$ )
L1	1450
L2	2925
L3	4375
L4	5850
L5	7300
L6	8775
L7	9050

# 5 Results and Discussion

## 5.1 Linear bearing test

In this section, the results based on the linear bearing test done by Huisman Equipment will be discussed.

### 5.1.1 Hits vs counts

As mentioned in 2.6.1 Acoustic emission based fracture model both the hits and the counts of the AE signal are used to determine the SIF based on the AE. Since the hits and counts are relatively similar to each other.

In Figure 27, the SIF based on the hits and counts are shown respectively. The constants for the hits were scaled to obtain similar results, as the hits are smaller in magnitude than the counts. Both the values and trend of both lines differ from each other. The SIF values obtained with the hits are smaller than the obtained with the counts. This is not a problem, as the intercept constant  $B$  can be changed in magnitude to cover up this difference.

However, the difference in trend cannot be changed by changing the values of the used parameters. One of these differences in trend can be seen in Location C between 10 and 15 machine cycles. The difference in trend between the hits and counts can be explained with the derivations of the counts. As shown in equation 36, the counts depend on the factor  $c_{ave}$ . This factor is larger for higher frequency. As a result, the higher frequencies will be more dominant in the counts than that they are for the hits. Therefore, the trend of the hits and counts is different.

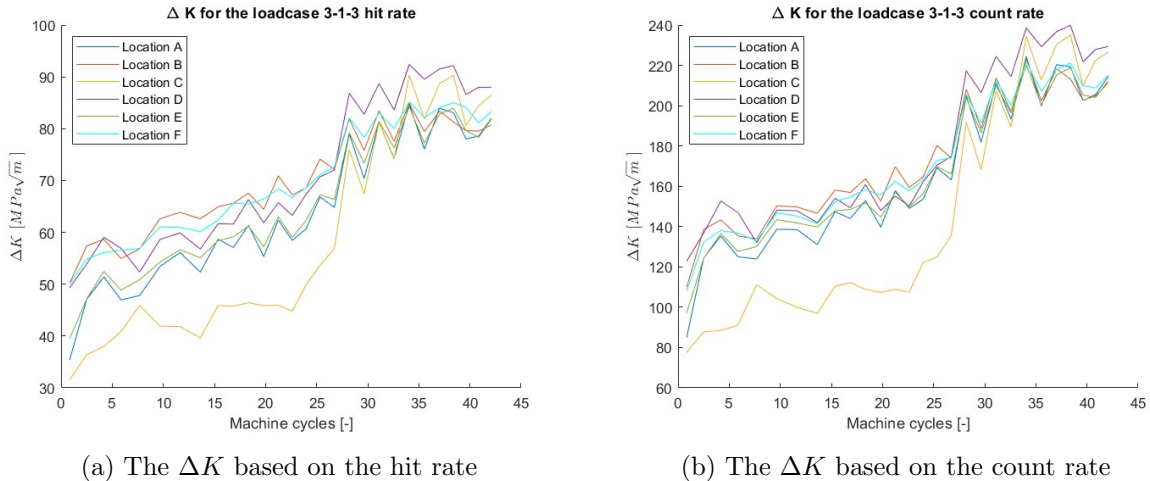


Figure 27: The  $\Delta K$  for both the count and hit rate

The obtained SIF for the hits and counts differ quite a lot, since the maximum SIFs are  $90 \text{ MPa}\sqrt{\text{m}}$  and  $250 \text{ MPa}\sqrt{\text{m}}$ , respectively. The hits resulted in lower SIFs than expected, since the lower bearing was already over its 100% theoretical lifetime. Therefore, it was expected that the obtained SIFs would be close or even higher than the fracture limit, for tough ductile metals the fracture limit is around  $150 \text{ MPa}\sqrt{\text{m}}$  [7]. Especially for the higher loads, it was expected

that the SIF would be higher than the fracture limit. However, the obtained SIF are lower than the fracture limit, while the count based SIF does exceed this limit. Therefore, the obtained values for the hits are expected to be too low.

The difference between Figures 27a and 27b is most probably due to a systematic error. This systematic error implies that  $B$  was not correctly chosen to represent the hit-based activity. The lack of representation is due to the used data being based on the counts. Therefore, the counts will be used in the remaining of this thesis.

### 5.1.2 Sensitivity study

The Paris model and the AE fracture model both depend on parameters, which are determined experimentally. Van den Ende, 2021 showed the effect of changes in the Paris model parameters had on the fatigue load to obtain the same amount of fatigue cycles for the base parameter case [16]. As, the parameters of the AE fracture model are determined based on experimental data of other materials than the used material, the sensitivity of the model is important to know.

In Figure 28, the sensitivity of the AE fracture model on the intercept constant  $B$  is shown. The  $B$  was varied between 80% and 120% of the value shown in table 3. The SIF slightly changes when the constant is not equal to the original value. However, the crack growth changes more significant than the SIF when the parameter is changed. The changes are the most significant when  $B$  is smaller than the original value of  $B$ . The crack growth rate is about 17.5% larger, which is a reasonable change.

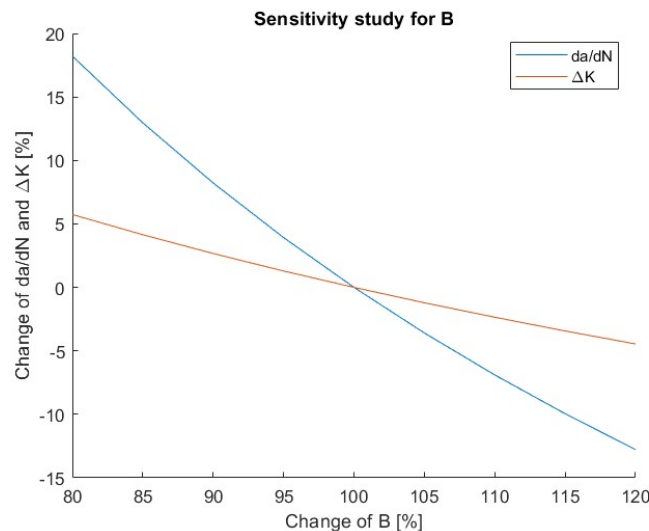


Figure 28: Sensitivity study of the intercept constant  $B$

In Figure 29, the sensitivity based on the slope exponent  $p$  is shown. The same as for Figure 28, the  $p$  was also varied between 80% and 120% of the value shown in table 3. The changes of the slope do influence both the SIF and the crack growth rate significantly. Like the intercept constant, the changes are the smallest when the parameter is greater than its original value. As the crack growth rate, for the case when  $p$  is 120% of its original value, is around 100% smaller than for the original value. While the crack growth rate is about 275 % larger than the original value when  $p$  is 85% of its original value. In addition, the case of 80% is not even plotted as the change was too large. Meaning that the results of the model heavily depend on the slope parameter  $p$ .

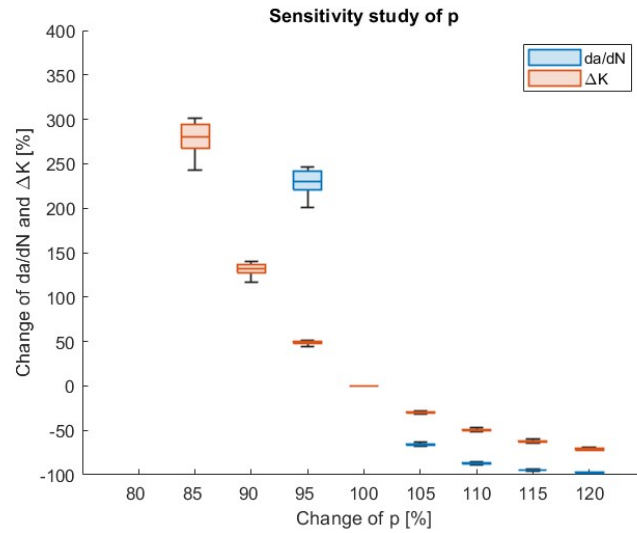
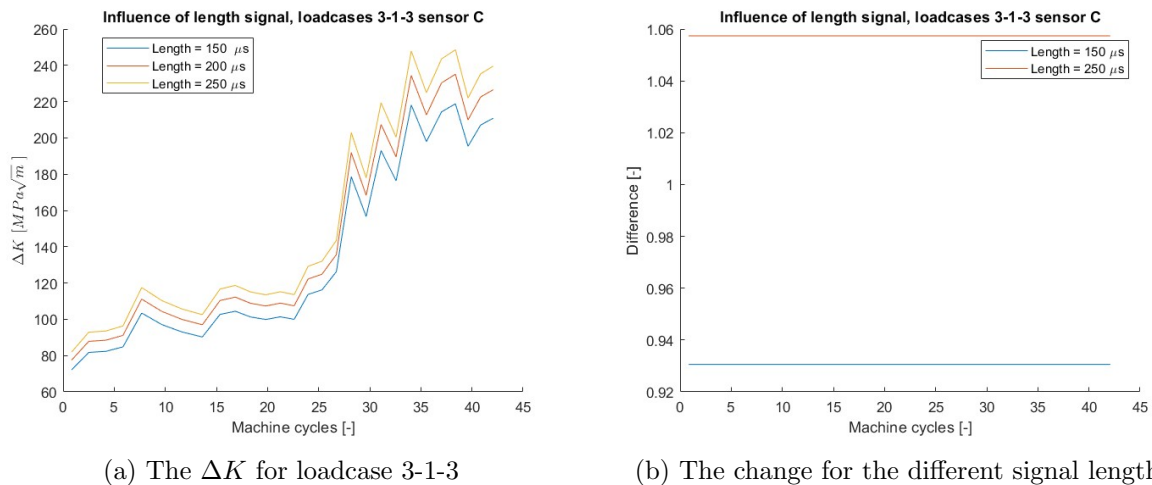


Figure 29: Sensitivity study of the slope exponent  $p$

### 5.1.3 Influence signal length

As mentioned in 2.6.1 Acoustic emission based fracture model, the counts are determined based on a signal length of  $200 \mu\text{s}$ . The length of the signal will influence the number of counts. Since, a smaller length will result in a lower number of counts and of course the other way around also holds. So, a longer signal length will result in a higher number of counts.

In Figure 30, the influence of the signal length is shown. For this plot, two different cases were considered, one being a smaller signal length of  $150 \mu\text{s}$  and the other being a larger signal length of  $250 \mu\text{s}$ .



(a) The  $\Delta K$  for loadcase 3-1-3

(b) The change for the different signal length

Figure 30: The influence of the signal length on the resulting  $\Delta K$

When the signal length is smaller, the resulting SIF is about 93% of the SIF calculated with the signal length of  $200 \mu\text{s}$ . Whereas, the SIF is about 106% for the larger signal length. Since, the changes in the SIF are small for the different signal lengths, the used signal length is considered to be valid.



#### 5.1.4 Acoustic emission model compared to the Paris model

As mentioned earlier, the linear bearing test was used to obtain these results. For the Paris model, some assumptions needed to be made. The main assumption was for the loading up to the part were the actual test started. For this loading, it is assumed that it was varied between load level L2 and L7. The resulting average load was close to load level L3.

For the number of cycles done by the lower bearing, another assumption was made. This assumption was that before the test started the bearing has done 1.7 million cycles. In Figure 31, the SIF based on the Paris model is shown for the lower bearing. After 1.7 million cycles, the SIF is close to the fracture limit, as the bearing below the traveller had already reached its theoretical lifetime.

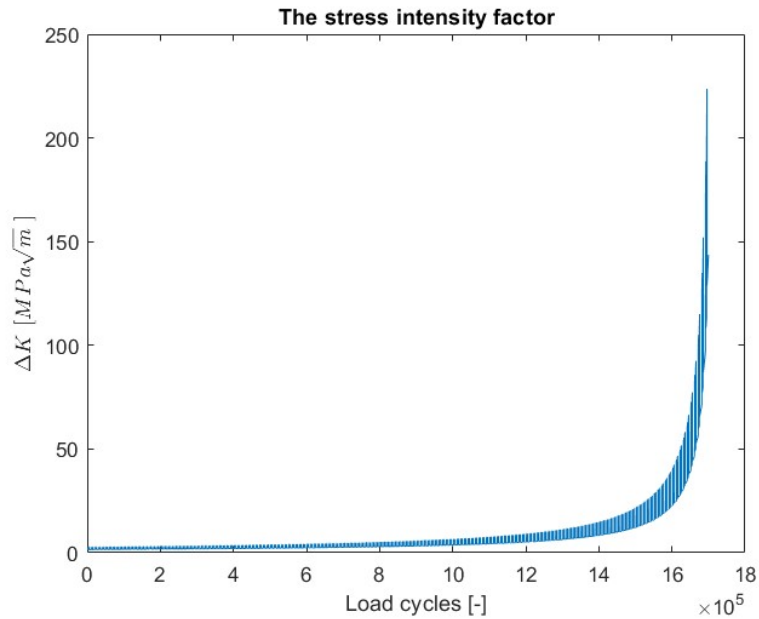


Figure 31: The growth of  $\Delta K$  over the load cycles done

In Figure 32, a plot is shown where both models are plotted. This plot was made for testcase 3-1-3, meaning that the test was operated with fully flashed grease and that the traveller was operating at the fastest speed. Furthermore, the sensors at location A and B were placed on top of the traveller.

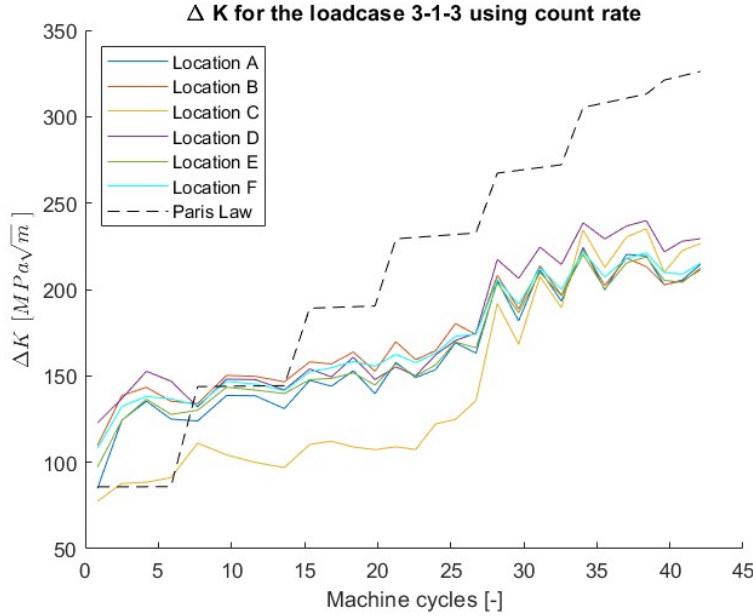


Figure 32: The  $\Delta K$  for both the Paris model as the acoustic emission model for testcase 3-1-3

For the Paris model, it can be observed that the line can be divided into seven blocks. Each block has its own slope. The difference in slope for the different block can be explained, as each block corresponds to another load level. So, the plot was made from L1 up to L7, the same as how the test was operated. Meaning that the increase in steepness of the slope is due to the increase in load and therefore an increase in the SIF.

For the AE-based fracture model, the increase in the SIF is less due to increase in load level. Furthermore, for the lower load levels until load level L4, a difference in SIF between sensor location C and all the other sensor locations is visible. This observation agrees with the hypothesis that the measured values of C would be lower than D. This is because, at the start of the entire test, the lower bearing, sensor location D, was already damaged more than the upper bearing, location C. The difference between the two different bearings decreases for the remaining load levels L5 up to L7.

In addition, the difference between the remaining sensor locations is small. Meaning that the sensors at location A, B, D, E and F have measured similar degradations.

When comparing the Paris model to the AE-based fracture model, several things can be noticed. To begin with, the slope of both models is different, which can be explained with the use of the equations 27 and 33 and the used parameters. The increase between the crack growth rate and the count rate both depend on the SIF. However, for both models the SIF is calculated differently, but the main difference is due to the different slope parameters used. As this parameter will have the most impact on the slope of both lines. The assumption for the slope parameter resulted in the different slope. However, when the slope is equal,  $p = n$ , the SIF based on AE will be much larger. Meaning that the used parameters need to be constructed carefully.

Furthermore, the obtained SIFs differ in magnitude from each other. For load level L1, the Paris model is lower than obtained values for the lower bearing by the AE model. As the value of the Paris model is close to the value of the upper bearing at sensor location C.

In addition, the values for the lower bearing match well for the load level L2. However, the SIFs obtained by the Paris model are higher than the ones obtained with the AE model for the load levels L3 and higher, because of the steeper slope of the Paris model.

In Figure 33, the comparison between the testcase 3-1-2 and the Paris model is shown. The main difference for the testcase is the operating velocity of the traveller, as it operates at a lower speed for this testcase. The main difference between the two tests is that for the testcase 3-1-2 the SIF values are little bit higher. Moreover, for the testcase 3-1-2, the trend of SIF is closer to the of the Paris model for the load levels L4 up to L7.

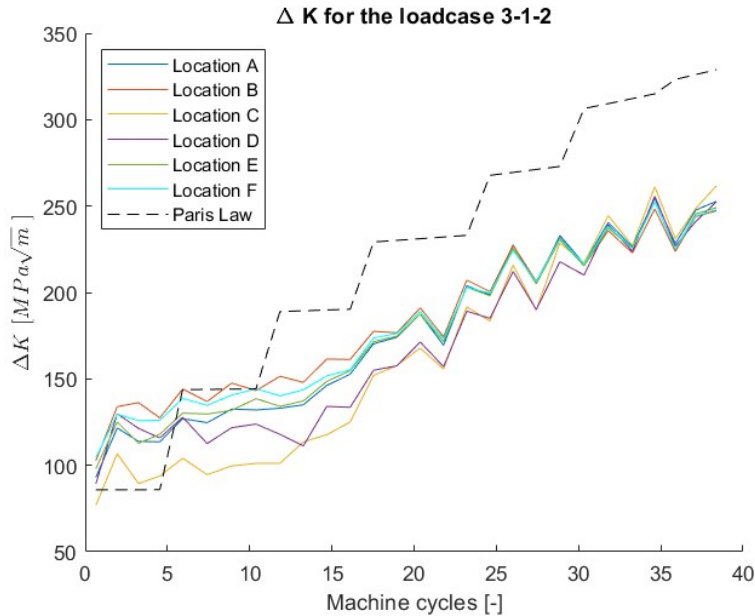


Figure 33: The  $\Delta K$  for both the Paris model as the acoustic emission model for testcase 3-1-2

In Figure 34, the comparison between the testcase 3-1-1 and the Paris model is shown. For this testcase, the traveller is operating at the lowest operating speed. The results of the testcase 3-1-1 are close to those of testcase 3-1-2. This means that the operating speed does not have much of an influence on the outcome of the AE model. This is a good observation, as the offshore bearings will obviously not operate at one constant speed.

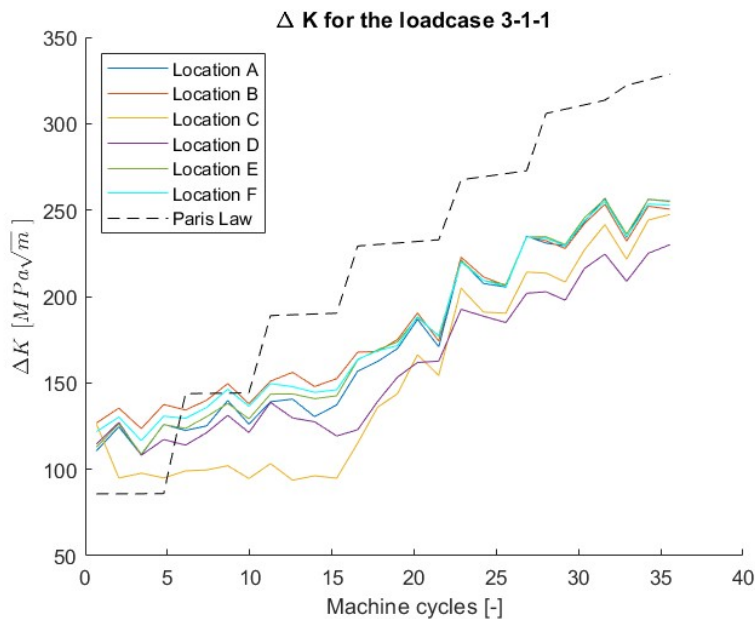


Figure 34: The  $\Delta K$  for both the Paris model as the acoustic emission model for testcase 3-1-1

### 5.1.5 Remaining useful life

As stated in 2.7 Remaining useful life, the RUL of the bearing is calculated in this thesis in three different ways. The RUL of these methods are calculated for the lower bearing of the linear bearing test. The results of these RUL 's are shown in Figure 35.

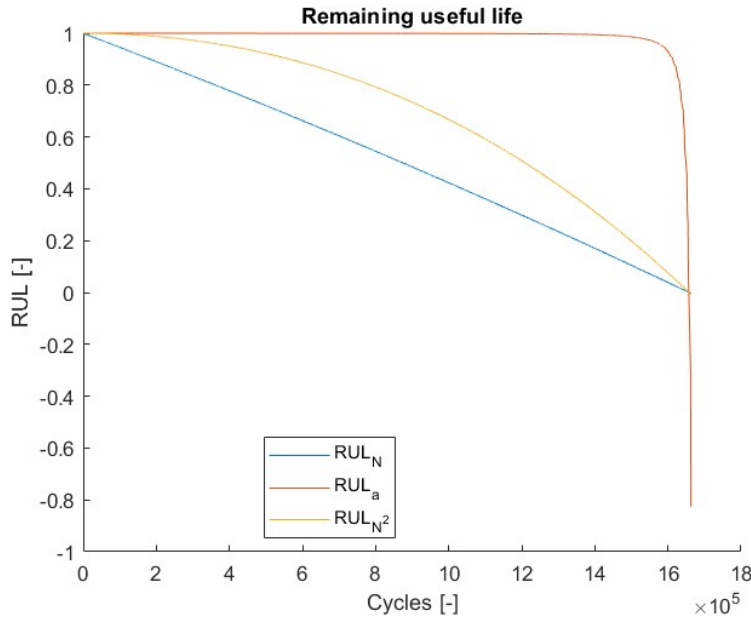


Figure 35: The comparison of different options for the RUL prediction

The RUL based on the crack length will not be a feasible option to use. As the RUL does not or almost not decline for the first 1.6 million cycles of the bearing. While, in the last 100,000 cycles, the entire RUL is used up. Meaning that it will not be useful to be able to prevent failure of the bearing in time and to reduce the down time of the operation.

For the RUL based on the number of cycles two options were used, one being linear (blue) and the other being quadratic (yellow). Both RUL 's decline when the number of cycles increases. The quadratic form declines less fast when the bearing is still in good state and declines faster when the state of the bearing decreases compared to the linear form.

The linear form will be used for the DT, as the linear decline makes it easier to make prediction for the bearing repair and or replacement. In addition, most papers use a linear form to describe the RUL, such as Meng et al. [34].

## 5.2 Aoka Mizu

The results shown in this section are based on Bluewater Energy Services 's vessel the Aoka Mizu. For the AE assumptions needed to be made, as the vessel does not have those sensors for measuring the AE. The AE data from the linear bearing test done by Huisman Equipment, described in [43], will be used for the data, as the bearing is comparable to the bearing of the Aoka Mizu. The main bearing of the Aoka Mizu consists of 8 segments, the segments ends are highlighted in the plots as a black line.

### 5.2.1 Timesteps in data

The influence of the timesteps between the different data points is investigated. As, the force is measured at a frequency of 10  $Hz$  and the rotation of the ship is measured with a frequency of 50  $Hz$ . Both the force and the rotations are measured continuously. The influence of the timestep is investigated based on the rotation of the turret, as the force on the bearing does not change rapidly over time, but rather slow. As a result, the limiting factor for the timestep will be the turret rotation, since the turret rotation changes in a smaller timeframe.

In Figure 36, the rotation of the turret is shown. The rotation data is based on four different timesteps, which are 0.2 seconds, 1 minute, 3 minutes and 30 minutes. Smaller timesteps than 0.2 seconds, are not investigated for the influence of the timesteps, as the change of the rotation will be in the range of the accuracy of the system for determining the rotation of the turret.

First, the timestep of the 30 minutes (purple line). This timestep does not capture the behaviour of the rotation of the vessel well. As, only two data points exists for the data file, resulting in a linear line. This linear trend does not follow the wavy pattern the turret is rotating in. So, the 30-minute timestep will not be used.

Second, the timestep of the 3 minutes (yellow line). This timestep does capture the behaviour of the rotation of the turret better than the 30-minute timestep. For this timestep, the trend starts to follow the wavy pattern of the rotating turret. However, the peaks of the 3-minute timesteps are lower than for the 0.2-seconds and 1-minute timesteps.

Third, the 1-minute timestep (orange line). Compared to the larger timesteps, the rotating behaviour of the turret is captured better, as the trend is close to the of the 0.2-seconds. The difference between the 1-minute and 0.2-seconds is small, as the peak values are more or less the same. Only the small peaks are not captured by the 1-minute timestep.

Lastly, the 0.2-second timestep (blue line). The rotating behaviour of the turret will not be captured better with timesteps smaller than the used 0.2-seconds. The main reason for this is the accuracy of determining the turret rotation. For the 0.2-seconds, there are already flat parts in the graph. Meaning that the rotation of the turret is smaller than the accuracy of the system. So, smaller timesteps will only increase the flat part in the graph.

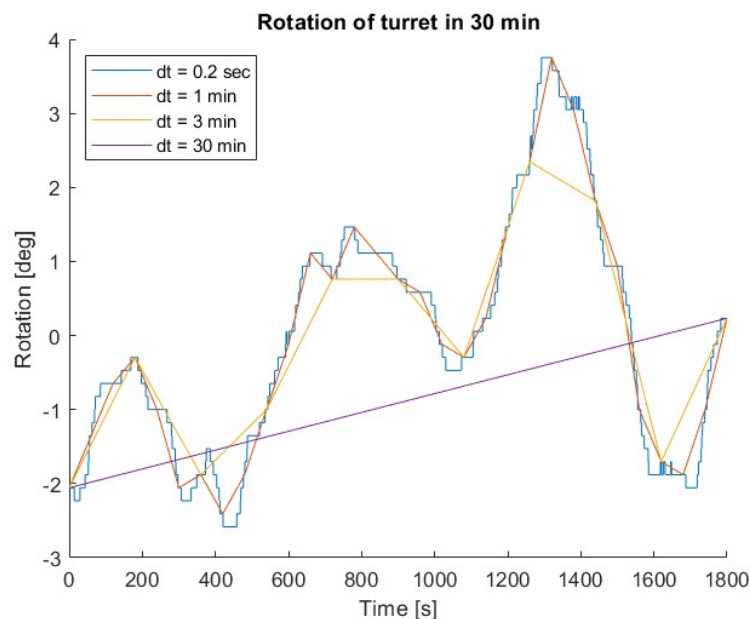


Figure 36: The rotations of the turret in half an hour

In Figure 37, a schematic overview of the bearing is given. In this overview, the difference between taking a 1-minute and 3-minute timestep for the number of load cycles for one month is shown. These load cycles are only determined based on the rotation data for one month. It can be seen that the bearing has been exposed to more than 30% more load cycles for the 1-minute timestep compared to the 3-minute timestep. This is a result of not capturing the peak values correctly, as shown in Figure 36.

In addition, the peak capturing is affected by the type of wave. As, there are short and longer waves. The short waves, being wind-generated waves, which can be wind sea, surface gravity waves and swell, have typically a period approximately of 30 or less seconds. While the longer waves have varying periods between 30 seconds up to several minutes. An example of these longer waves are infra-gravity waves. [20]

So, the timestep of 3 minutes is too long to capture the changes in the short-wave properties correctly. Resulting in the fact that the number of load cycles is estimated too low. Furthermore, the properties of the short waves can change within the 1-minute timestep. However, as can be seen in Figure 36, these changes do not result in drastically different rotations compared to the smaller timestep. So, for the remaining of the thesis a timestep of 1 minute will be used, as it captures the rotating behaviour well and will reduce the computational burden drastically compared to smaller timesteps. When comparing it to the 0.2-second timestep, the computational burden is reduced with a factor of 300.

The assumption to use the 1-minute timestep will affect the RUL prediction of the bearing. As the number of fatigue cycles counted will differ from the actual number of fatigue cycles performed. This difference is expected since the smaller timestep (dt of 0.2 seconds) oscillates around the used time step. This means that the real number of fatigue cycles will be larger compared to the number of fatigue cycles based on the 1-minute timestep. However, it is expected that the difference between the fatigue cycles will be small. Therefore, the assumption is assumed to be valid and will be used to reduce the computational burden.

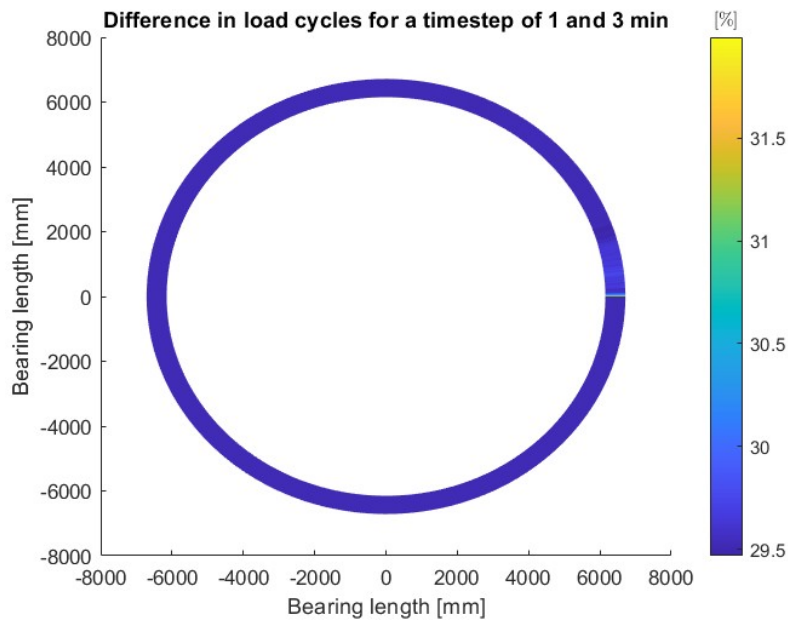


Figure 37: The difference in load cycles done for a timestep of 1 and 3 minutes in one month

## 5.2.2 Remaining useful life

In this section, the RUL of the bearing is calculated. The RUL is calculated in two different ways. For the first way, only the force and rotation data of the Aoka Mizu are used. Which means that the RUL is based solely on Paris model. For the second way, the DT's proposed methodology is used. This involves using the AE data in addition to the force and rotation data.

### Remaining useful life based on the Paris model

In Figure 38, the RUL prediction of the main bearing of the turret of the Aoka Mizu is shown. There are some interesting things to see in this figure. As it can be seen that there is a slightly dominant loading direction of the bearing. Meaning that at the field the combination of the wind, waves and current have a dominant direction. In Appendix B - RUL of bearing based on the Paris model, the same prediction was made, but with other limits for the plot. In Figure 54, the dominant loading direction is better visible.

Furthermore, the difference in the RUL is small, as the worst part is only about 2% worse than the best part of the bearing. Meaning that even though there is a dominant loading direction, the loads over the whole bearing are more or less similar.

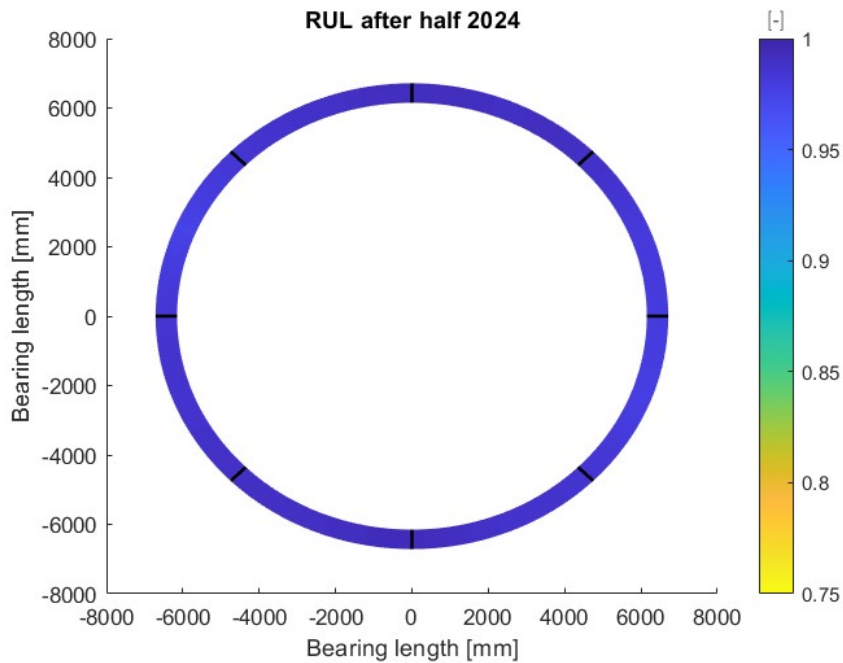


Figure 38: The RUL of the bearing of the Aoka Mizu in half 2024

In Figure 39, the development of the RUL prediction is shown. The prediction is divided into 6 parts, as the lines otherwise will overlap each other. The RUL prediction changes in slope. This change is biggest by going from 2019 to 2020. For the other years, the slope are minor.

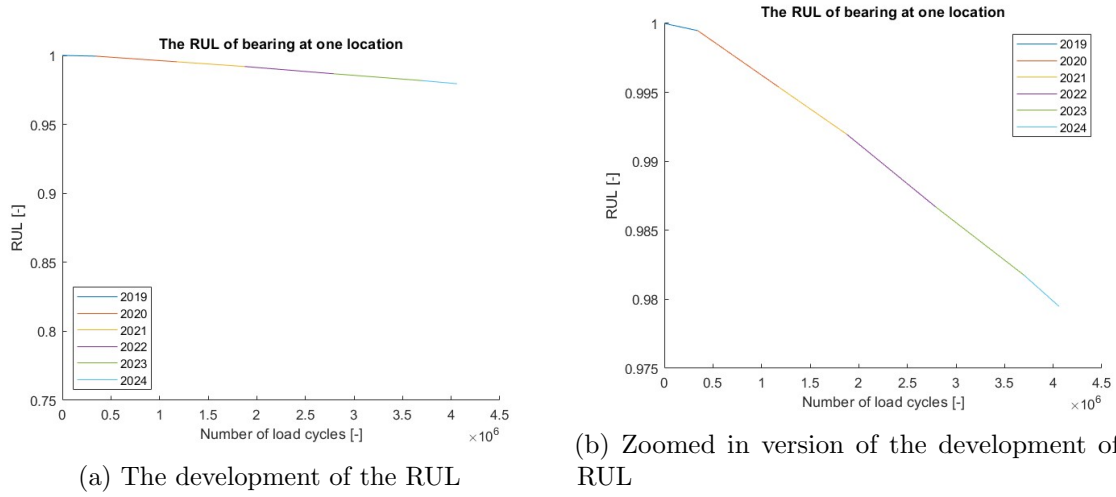


Figure 39: The RUL development of the RUL without AE

In addition, the loading for 2019 has to be the lowest, as the slope is the least steep of the six parts. As more and more force data is gathered, the changes in slope will become smaller and smaller. This is due to the fact that the RUL prediction is made based on the average of the load history of the bearing. In table 5, the predicted total number of load cycles to failure is shown, the same trend as in Figure 39 can be seen. Meaning that the predicted total is getting closer and closer to an equilibrium value.

So, the changes in loading will have the most impact on the first non-critical part of the bearing's lifetime prediction when the AE is not taken into account. However, as the bearing gets older, the average of the force will be less sensitive to small changes in the loading. Meaning that the RUL prediction without AE will reach an equilibrium for the prediction.

Table 5: The predicted total number of load cycles to failure

Year	Total number of load cycles to failure ( $N_f$ )
2019	$6.755 \cdot 10^8$
2020	$2.621 \cdot 10^8$
2021	$2.406 \cdot 10^8$
2022	$2.180 \cdot 10^8$
2023	$2.086 \cdot 10^8$
2024	$2.036 \cdot 10^8$

### Remaining useful life based on the proposed methodology

A run-to-failure experiment was done for a representative test set-up of a segment of a large-scale slew or turret bearing. This test set-up consisted of a double linear bearing, where the top chamber and bottom chamber are identical to each other, as the bottom chamber is a vertically mirrored copy of the top chamber. The AE was measured at four different positions in each chamber during the linear bearing test. The sensors were positioned on the nose raceway (L), support raceway (U), nose substructure (B) and the support substructure (A). The graphical representation of these sensor positions is shown in Figure 40. [44]



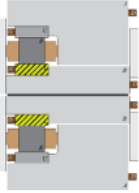
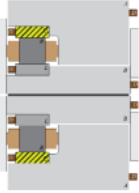
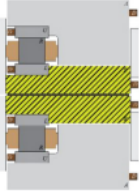
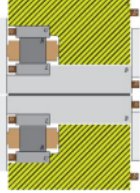
Specification	Nose raceway	Support raceway	Nose substructure	Support substructure
Low frequency: 40–100 kHz	Top: Channel 20 Bottom: Channel 2	Top: Channel 19 Bottom: Channel 1	Top: Channel 14 Bottom: Channel 8	Top: Channel 13 Bottom: Channel 7
Mid frequency: 95–180 kHz	Top: Channel 22 Bottom: Channel 4	Top: Channel 21 Bottom: Channel 3	Top: Channel 16 Bottom: Channel 10	Top: Channel 15 Bottom: Channel 9
High frequency: 180–580 kHz	Top: Channel 24 Bottom: Channel 6	Top: Channel 23 Bottom: Channel 5	Top: Channel 18 Bottom: Channel 12	Top: Channel 17 Bottom: Channel 11
Graphical representation of measurement location (indicated by hatching pattern)				

Figure 40: The sensor locations for the linear bearing [44]

For the bearing of the Aoka Mizu, four different AE sets are used. These sets are each based on one of the sensor locations. The data set are setup by placing the top chamber sensor on the top of the bearing and the bottom chamber sensor at the bottom of the bearing, as shown in Figure 41.

As the bearing is divided into multiple grid cells, it is necessary to interpolate the AE over the whole bearing. Meaning that for the right-hand side, the AE is interpolated from the bottom sensor to the top sensor. For the left-hand side, the AE is interpolated from the top sensor to the bottom sensor.

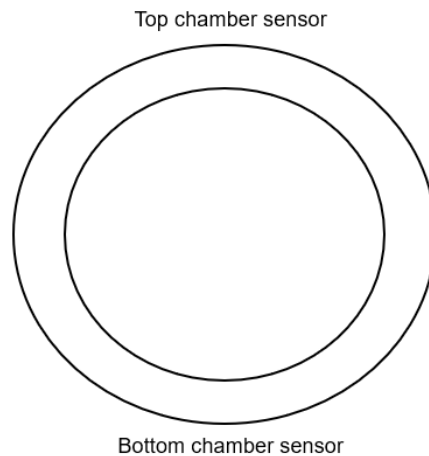


Figure 41: The placement of the sensors

The length of the AE measurement does not match with the length of the rotation and the force data. This problem was solved by interpolating the AE data. By using interpolation, the data sets were matched to have the same length. The AE data was interpolated from 0 cycles up to 24,250 cycles. The point of 24,250 cycles was chosen as this point is close to the number of cycles the bearing of the Aoka Mizu has done. The counts used for the RUL prediction are shown in Figure 42. The last AE data point is marked with a dotted line.

In addition, the AE data set needed to be scaled. As without scaling, the sum of the count rates was about 48,000 times larger than the of the original data. So, a scaling factor was added to the AE data set to ensure that the sum of the count rates was equal to each other. The scaling factor was calculated by dividing the original sum of counts by the sum of the interpolated AE data counts. This factor was then multiplied with the interpolated count.

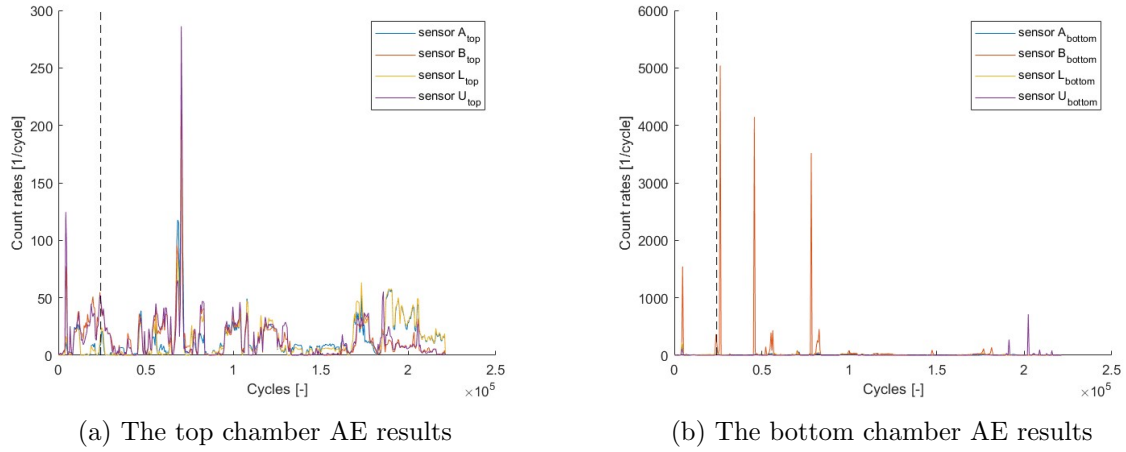


Figure 42: The AE data set of the entire linear bearing experiment

In Figure 43, the correlation between the Aoka Mizu data and the AE data is shown. The Aoka Mizu consists of operational and non-operational data. As the Aoka Mizu was modified and refit in Dubai during 2017 and 2018, in preparation for the operation at its new location [5]. The Aoka Mizu arrived at the field on 17<sup>th</sup> of March and was hooked up on the 19<sup>th</sup> of March [50].

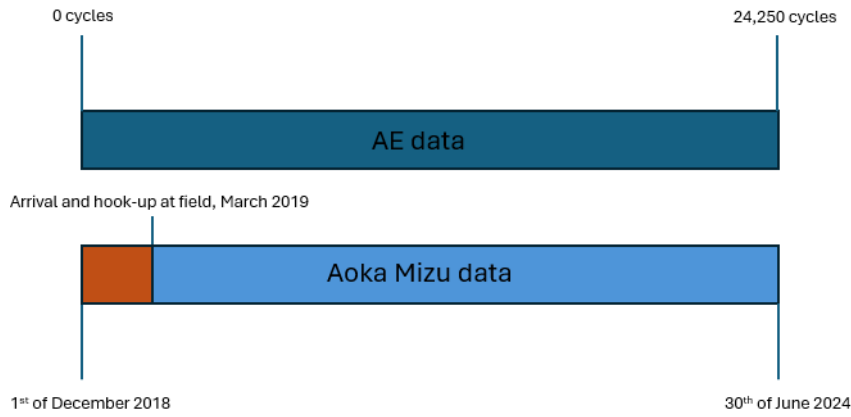


Figure 43: Graphical representation on how the AE data is related to the Aoku Mizu data

In Figure 44, the RUL prediction of the bearing, when AE is considered, is shown. This RUL was calculated based on the proposed methodology depicted in Figure 23. Meaning that both the AE model and the Paris model were used to obtain these results.

The calculated RUL is lower than the RUL solely based on the Paris model, shown in Figure 38. Based on this observation, it can be concluded that the AE influences the prediction. The RULs differ up to 10% , which can be considered as significant. Due to the AE model, the average SIF will be higher compared to only the Paris model. As the resulting SIFs from the AE model are for low counts relatively high, since the slope is not as steep as the of the Paris model. Therefore, the crack will grow faster in this stage. As a result, the SIF based on the Paris model will also start to increase more rapidly as this SIF depends on the crack length.

Furthermore, the used counts can also affect the results, since these counts were not measured at the Aoka Mizu itself. As the used counts were based on a run-to-failure experiment. Meaning that there is a possibility that the used counts were too high.

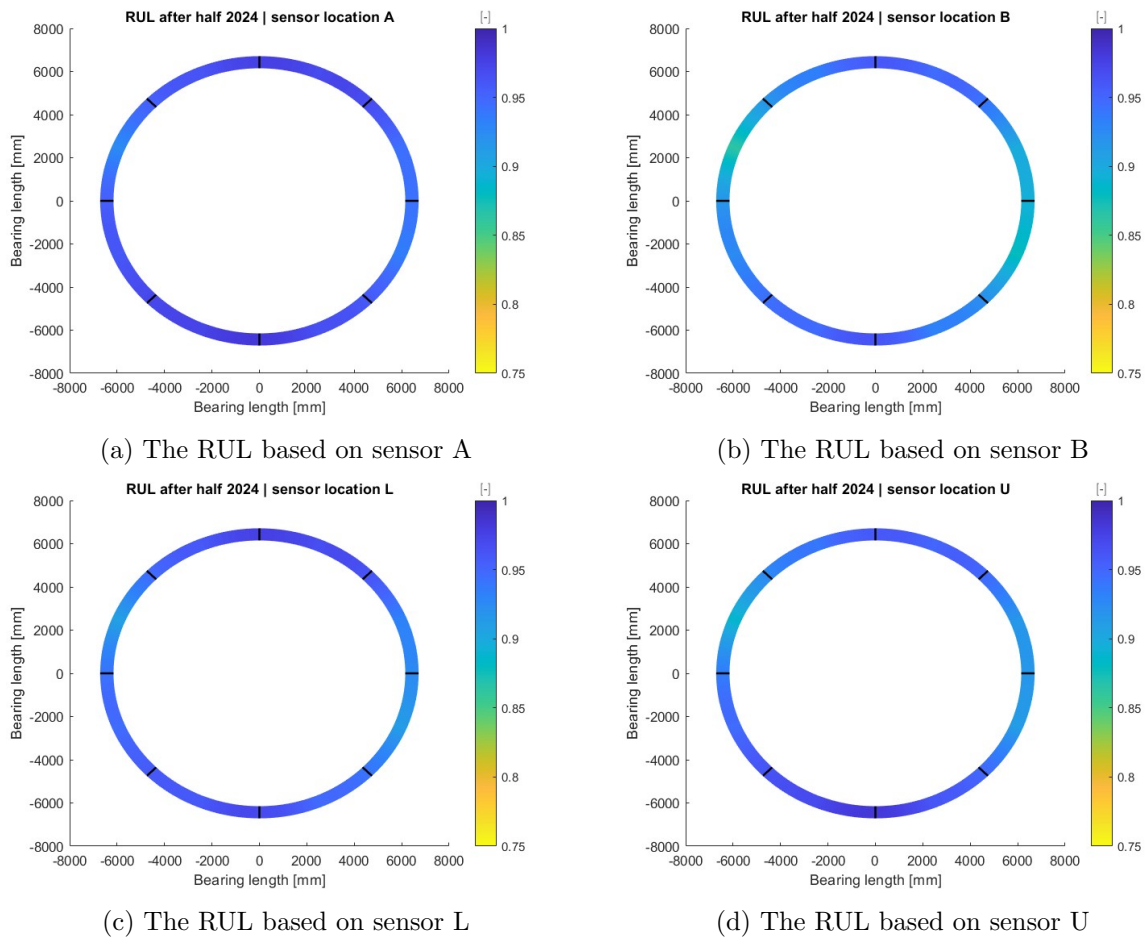


Figure 44: The RUL predictions based on the 4 sensor locations after half 2024

When comparing the different sensor locations to each other some interesting things can be noticed. The first thing to notice is that the sensor location at the nose substructure resulted in the worst RUL prediction. This was not expected since three out of the six channels were not working for these sensors at that location. As a result, no low frequency content was captured. So, therefore, it was expected to result in the 'best' RUL values.

The second observation is that the sensor location A was the closest to the Paris model results. As the RULs differ with a maximum of around 3% to each other. While the RULs for the other locations differ with around 5% up to 10%.

Furthermore, the results of sensor locations of the raceways (L and U) are relatively close to each other. While the locations at the substructure (A and B) do differ quite a lot from each other. Meaning that the sensor location will influence the prediction.

In Figure 45, the RUL development of the Paris model and the four sensor locations are at the most right side of the bearing is shown. The slope of the RUL based on the Paris model remains fairly constant. While the slope of the RUL prediction, where AE data is considered, does change over time. This means that the DT can correct the Paris model if the crack does not follow exactly the trend described by the Paris model.

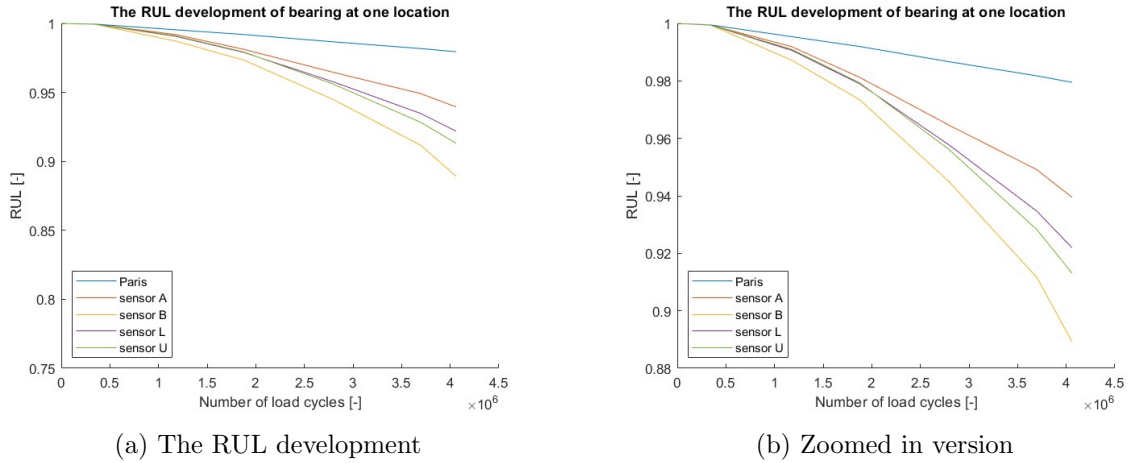


Figure 45: The RUL development at the most right side of the bearing

### Remaining useful life based on the AE model

The influence of the AE on the RUL prediction is investigated. This was done by calculating the SIF with only the AE. Therefore, the crack growth is only based on the AE model.

In Figure 46, the RUL prediction solely based on the AE is shown. The first thing to notice is that the RUL prediction based on the four different sensor locations are worse compared to the RUL based on the Paris model and the designed methodology. The RUL solely based on AE is at every location lower than the designed methodology. Meaning that the AE-based fracture model overestimates the crack growth rate compared to the Paris model. By using the designed methodology, the overestimation of the crack growth rate is less due to the averaging used between the SIFs.

Furthermore, the differences between the different sensors have become larger compared to the RUL results based on the designed methodology. The difference has become larger, as the overestimation of the crack growth rate is no longer reduced by the Paris law.

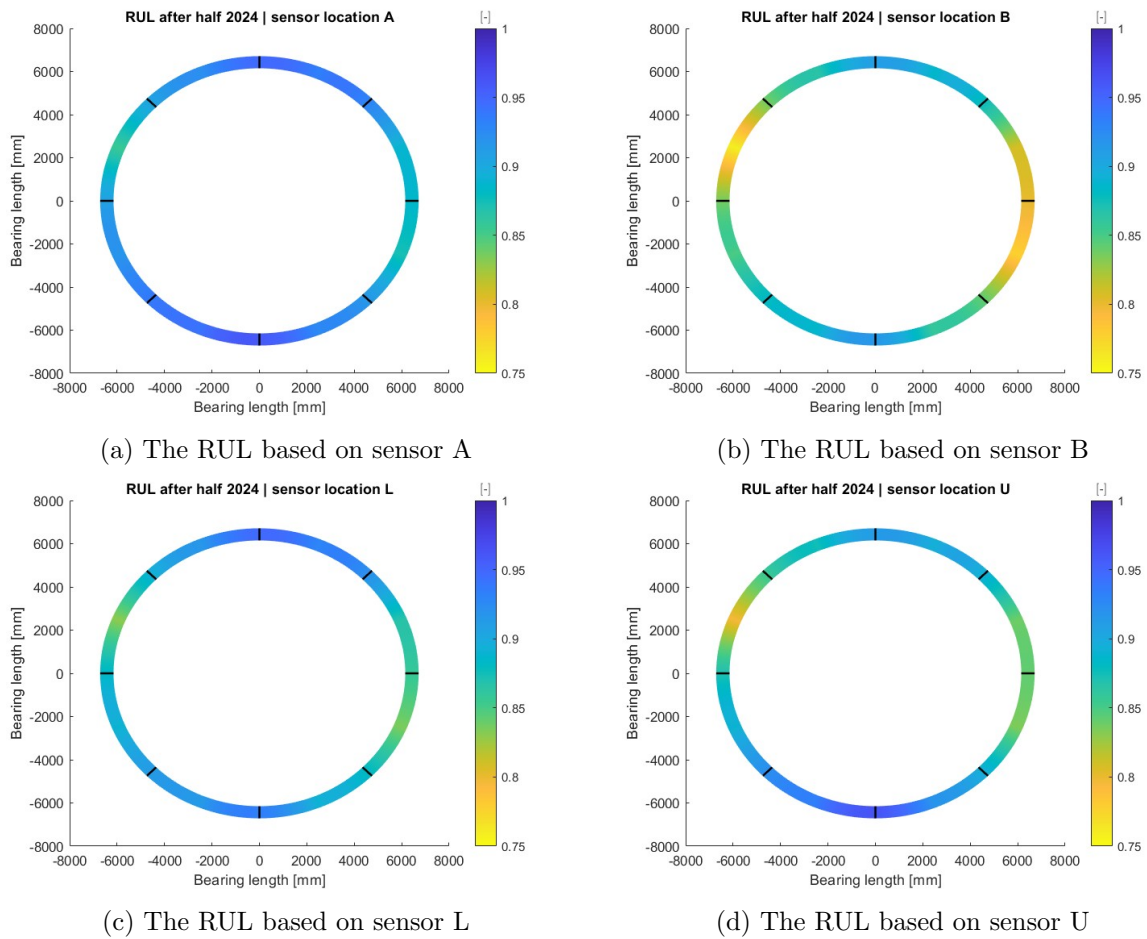


Figure 46: The RUL predictions based on AE of the 4 sensor locations after half 2024

In Figure 47, the development of the RUL predictions based on the Paris model, the designed methodology and the AE are shown. In Figure 47 only the sensor location U is shown, as the visibility would be poor when all the sensors were used in one plot. As the trends of the different sensors are similar to each other, it was opted to place the remaining results in Appendix C – Remaining useful life based on only AE. It can be seen that the difference between the Paris model, the designed methodology and the AE increase with the number of load cycles. The difference between the different models can be explained based on the crack growth rate, as the final RUL prediction is the same for the different models.

In the beginning of the life the bearing the crack is small and the measured count rate based on the AE is also small, as the bearing is still in good condition. Therefore, the difference between the different models is small. However, as the crack growth rate is larger for the AE model, the difference between the different models will become larger over time.

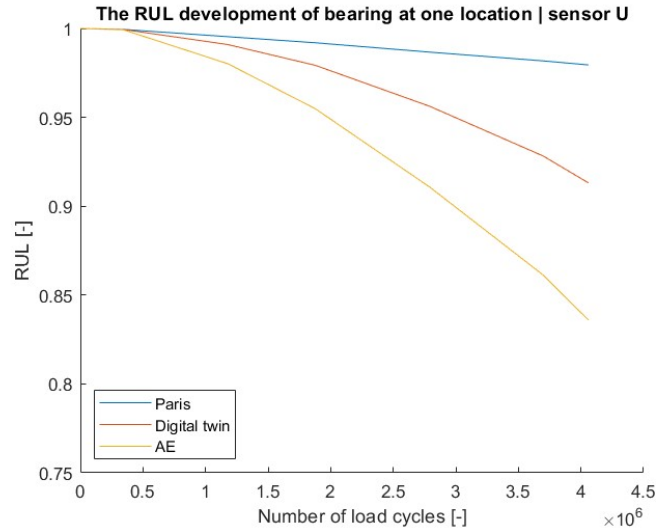


Figure 47: The RUL development based on only AE of sensor location U

### 5.2.3 Influence counts on Remaining useful life prediction

Since the sensors measure in noisy environments, the filtering of the AE signals is important. If this filtering is not done properly, other mechanisms, such as background noise, are considered for the crack growth rate. In this subsection, the influence of high counts is investigated. By using the entire AE data set of the linear bearing test, Figure 42, higher counts are taken into account, as the later stage of fatigue is now also considered.

In Figure 48, the resulting RUL prediction of the four sensors position for taking into account higher counts is shown. For this scenario, the RUL predictions are worse compared to the RUL predictions shown in Figure 44. The predictions are worse as the crack growth rate is higher due to the higher counts. Due to the higher crack growth rate, the resulting cracks will be larger which negatively impacts the RUL prediction.

Therefore, the AE data should be checked before it is used in the DT to minimize the effect of including faulty signals, such as friction and background noise, for the crack growth rate. Minimizing this effect reduces the probability of overestimating the RUL of the bearing. As a result, when the bearing is still in operational condition, it will not be replaced prematurely. The RUL prediction, for the higher counts, is about 10% lower than the prediction without the increased counts. The overestimation means that, according to the DT, the bearing should be replaced a few years earlier than necessary.

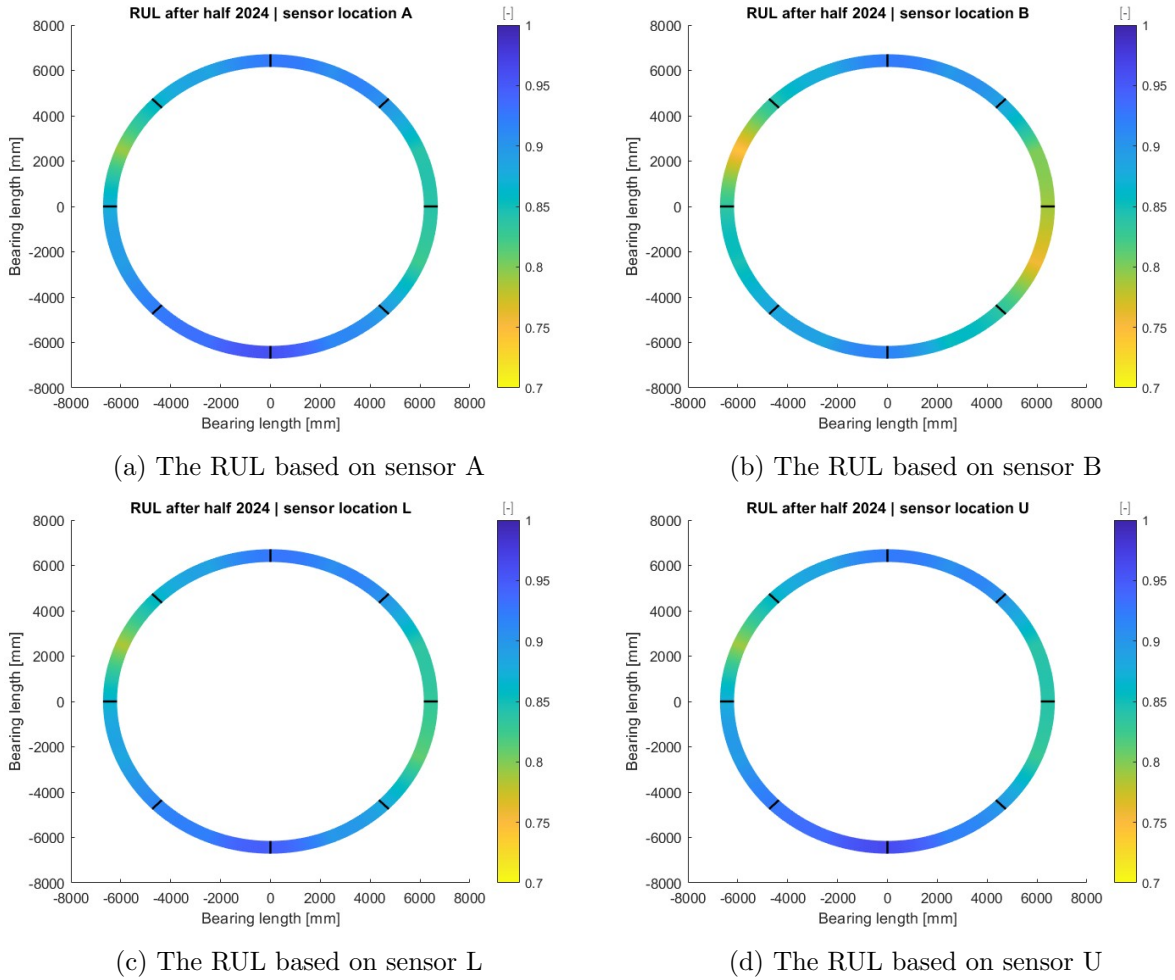


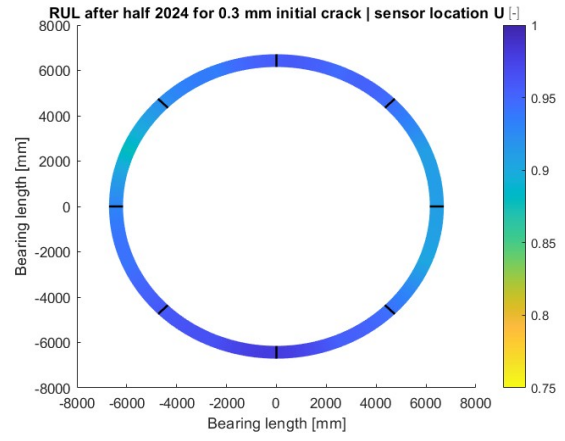
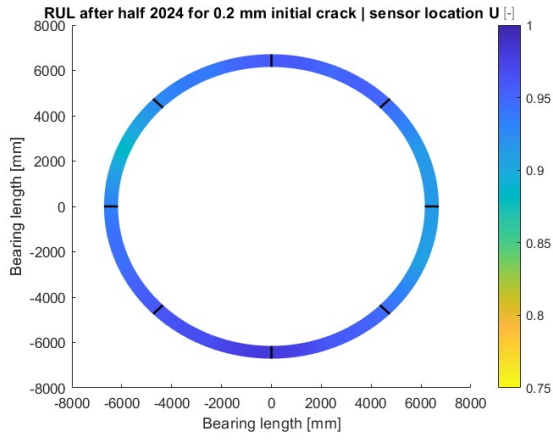
Figure 48: The RUL predictions based on higher counts for the sensor positions after half 2024

### 5.2.4 Sensitivity study

In section 5.1.2 Sensitivity study, the sensitivity of the AE-based fracture model was tested. In this section, the sensitivity of the RUL predictions to the crack size is investigated, as not every crack has the same initial crack size. For steel, the initial cracks size varies between 0.1 and 0.5 *mm* [39]. Therefore, the RUL prediction was conducted for an initial crack size of 0.1, 0.2, 0.3, 0.4 and 0.5 *mm*.

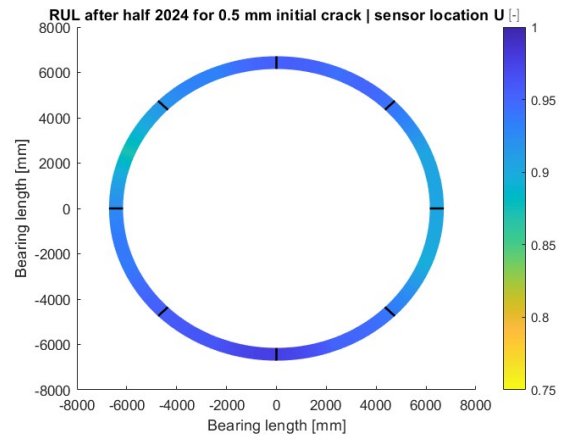
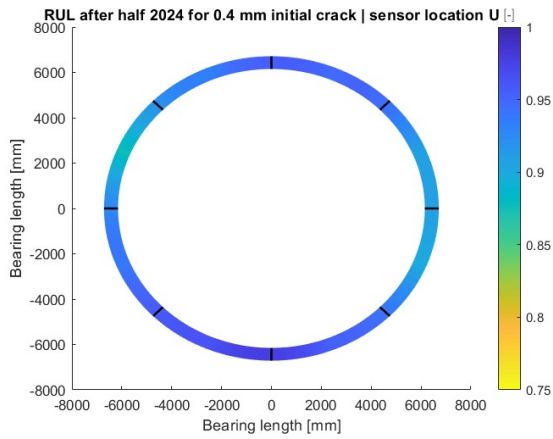
In Figure 49, the RUL predictions for the initial crack size of 0.2 to 0.5 *mm* is shown. Only sensor location U is shown in this section because the trend in the change in the RUL is the same for all four sensor locations. The figures for the other locations are shown in Appendix D – Sensitivity study initial crack size. In Figure 49, it can be seen that the RUL prediction becomes worse when the initial crack size increases. The RUL becomes worse as the model depends on the crack size. The SIF based on the Paris model will increase, as the SIF depends on the current crack size, equation 23. As a result, the crack growth rate will increase.

In addition, the AE-based fracture model indirectly depends on the initial crack size, since the used fracture models are averaged.  $\Delta K$  becomes larger when the initial crack size is increased. Since, the SIF based on AE does not change and the SIF based on the Paris model does become larger. As a result, the crack growth rate will increase due to the increased SIF. Therefore, the cracks will become larger at the end of the simulation for the increased initial crack size and the consumption of the RUL will be higher.



(a) The RUL based on an initial crack size of 0.2 mm

(b) The RUL based on an initial crack size of 0.3 mm



(c) The RUL based on an initial crack size of 0.4 mm

(d) The RUL based on an initial crack size of 0.5 mm

Figure 49: The RUL predictions based on different initial crack sizes for sensor location U after half 2024

In Figure 50, the development of the RUL predictions for the different initial crack sizes is shown. The obtained RUL predictions based on the different initial crack size is small, as the difference between the highest and the lowest RUL is only about 1%. A possible reason for this observation is that the crack growth is dominated by the AE-fracture model, where the dependence on the initial crack size is small compared to the Paris model. Van den Ende, 2021 showed that the initial crack size does influence the predictions based on the Paris model[16].



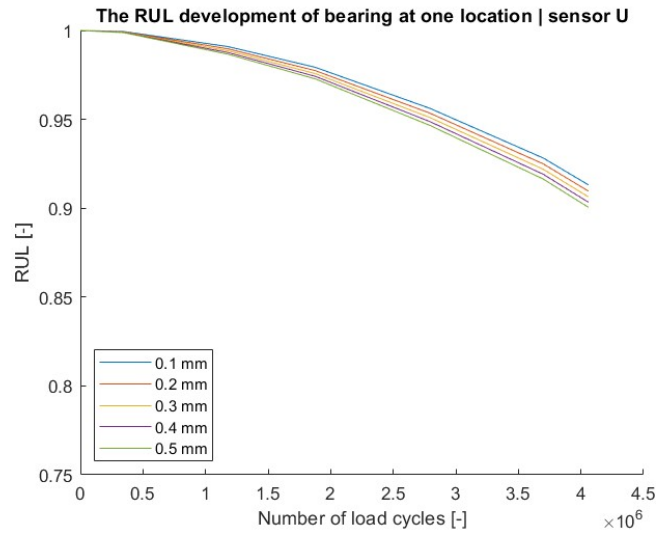


Figure 50: The development of the RUL for the different initial crack sizes for sensor location U

In Figure 51, the sensitivity of the RUL prediction to the initial crack size is shown. The box plot was made for the entire bearing, as the RUL is not constant over the entire bearing. The DT is not sensitive to changes in the initial crack size, as the changes in the RUL predictions are small.

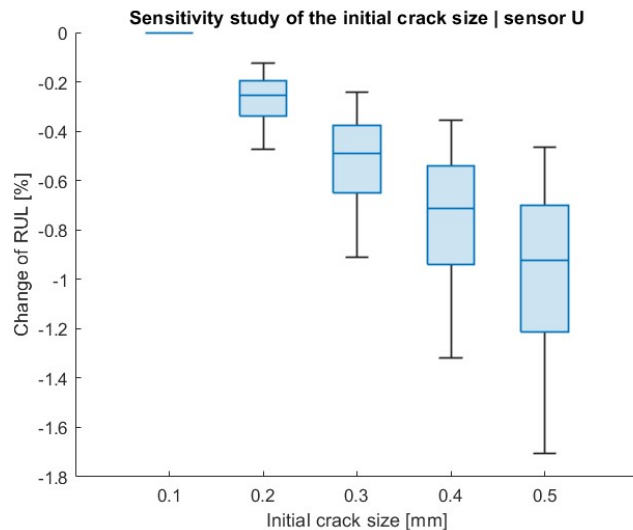


Figure 51: The sensitivity of the RUL prediction to the initial crack size for sensor location U

### 5.2.5 Influence AE interval

In this section the influence of the AE interval on the RUL prediction is discussed. Condition monitoring can be done in different ways, as the monitoring can be continuous and discontinuous. For the discontinuous monitoring, the interval will play an important role in the prediction. As the interval will affect the RUL prediction, four different intervals are used to investigate the effect on the prediction. These intervals will be 2, 4, 8 and 16 weeks, where the condition is only measured once per year, starting from January 1<sup>st</sup>.

In Figure 52, the RUL prediction based on the different measuring AE intervals is shown. As the trend of the RUL prediction is the same for all the sensor locations, only sensor location

U is discussed here. The other locations are shown in Appendix E - Influence AE interval. In Figure 52, it can be seen that the RUL prediction becomes worse when the AE interval increases. As stated earlier, the DT prediction for the RUL is dominated by the prediction made by the AE model. Meaning that the prediction made will start to deviate more from the prediction made by Paris model, when the AE interval is increased.

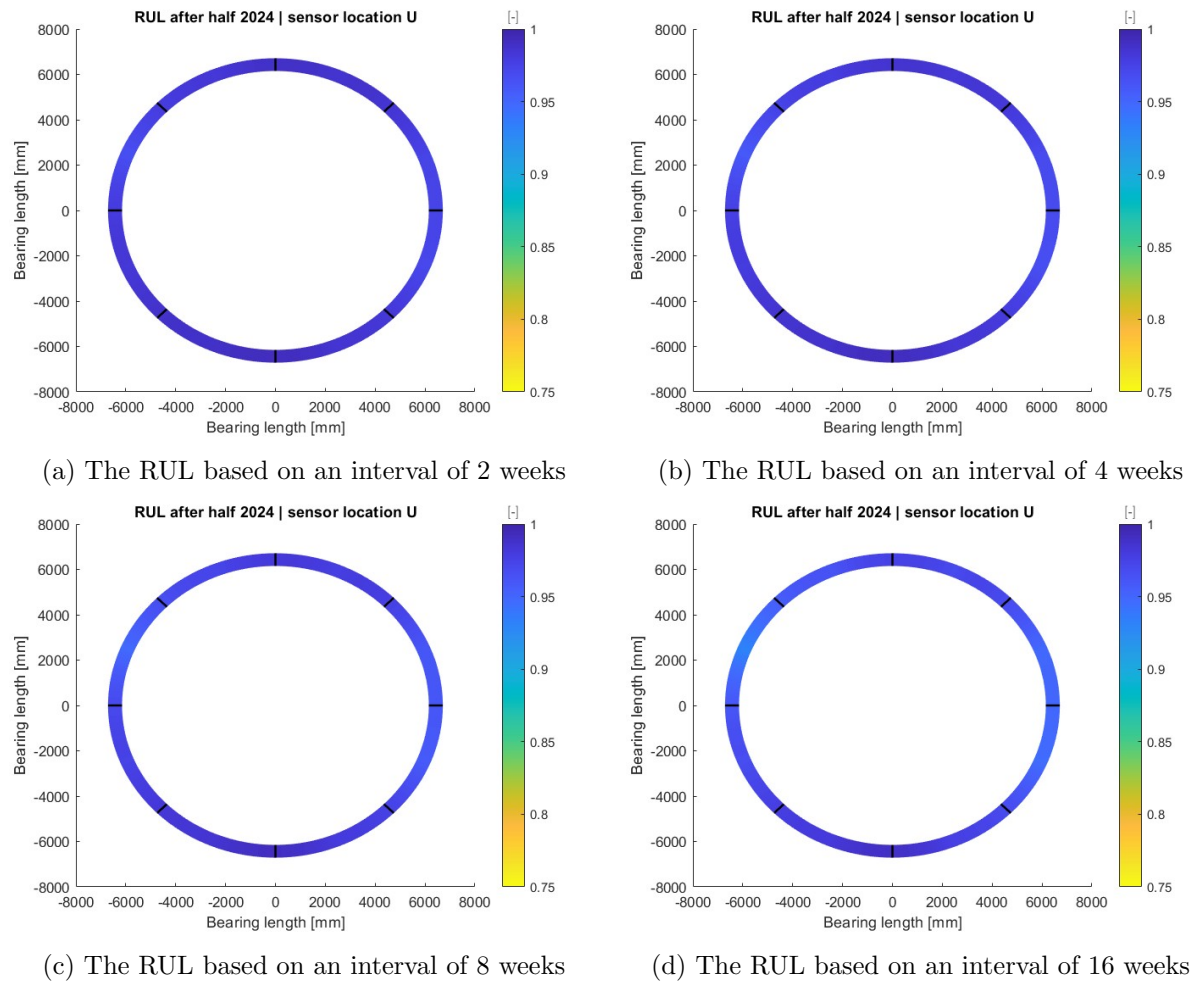


Figure 52: The RUL predictions based on different AE intervals for sensor location U after half 2024

In Figure 53, the RUL development is shown based on the different measuring AE intervals. For this figure, the prediction made with continuous monitoring is added, as all previous obtained results were based on continuous AE data. It can be seen that RUL prediction based on the 2 week interval is about 6% higher than the one based on the continuous AE data. This difference is a noticeable difference. Therefore, it is advised to use continuous monitoring, as the degradation of the bearing will be captured more accurately than when the AE data is measured in intervals.

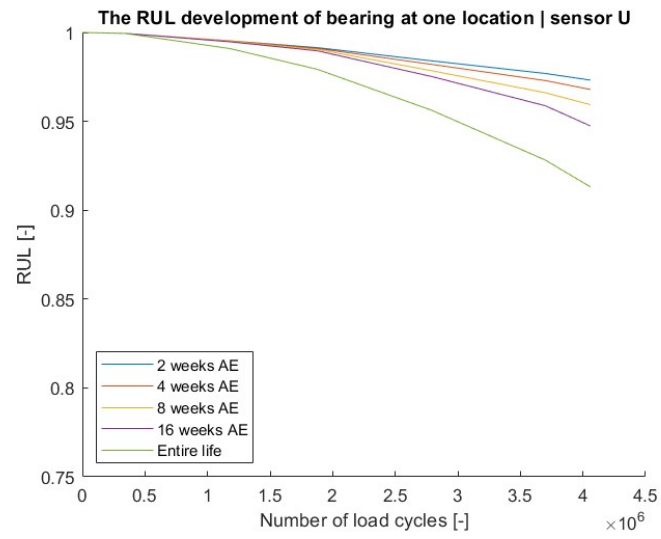


Figure 53: The RUL development for the different AE intervals for sensor location U

## 6 Conclusion and Recommendations

In this chapter, the conclusion of this thesis will be given. In addition, the recommendations for future work are given. Where the main research question is given below and will be answered. How can a digital twin be developed to predict the remaining useful life of a highly-loaded low-speed roller bearing?

DTs are used in many different sectors. As a result, there are many different types of DTs. In this thesis, three main different types of DTs have been considered. Those are the data-driven, physics-based and the hybrid type of DT. Each of these type of DT has its own advantages and disadvantages. The physics-based DT is the preferred option as its interpretability is higher compared to the other DT types. This interpretability out weights the advantage of the other DT types, which is finding good non-linear relations between the data and RUL.

The DT uses two different types of models for calculating the RUL. One model is based on a theoretical model and the other one uses the AE data. Based on the previous study done by B. van den Ende, it was opted to use the Paris model for the theoretical model. The SIF for the Paris model will be calculated for the subsurface originated cracks, as the SIF is larger compared to the surface originated cracks. The AE model is similar to the Paris model, as a similar relation between the rate of the AE parameter and the SIF exist as for the crack rate and the SIF based on the Paris model.

The parameter used for the AE model will be the counts. As the AE input data is given in hits, and counts are similar to hits. Hits will not be used since the obtained constants for the AE model were derived from count data and the AE model is highly sensitive. In addition, the obtained SIF based on the hits were lower than the SIF based on the counts, which were closer to the fracture limit for all the load levels, shown in Figure 27.

Both models were compared to each other, as shown in Figures 32 up to 34, to see if both models resulted in similar results. Based on those graphs, the SIF for the Paris model will be a little bit higher than the of AE model. In addition, for lower operating speed the difference in SIFs becomes less. So, both models yield similar results and can therefore be combined for calculating the crack growth.

The RUL prediction is based on the (final) crack size and the (total) number of load cycles. For this prediction, three different forms were considered, shown in Figure 35. The conclusion can be made that the linear form will be the most useful form, as the consumption of the lifetime is linear in the largest part of its lifetime, due to the stage II degradation takes the longest time, which makes it easier to schedule the replacement/repair of the bearing in time.

The development of the RUL prediction for the linear bearing, Figure 35, was only based on two different load levels. In Figure 39, the RUL prediction solely based on the Paris model, the effect of the load and the loading history is shown. It can be concluded that the predictions in the early stage have the possibility of over predicting the lifetime, due to the smaller loading history. However, this over prediction will not have significant impact, as the bearing will still be in good condition.

The computational burden of the DT can be reduced by increasing the timestep taken between the two measurement points. By changing the timestep, the accuracy is also changed.

Based on the rotation data shown in Figures 36 and 37, it was opted to go for a timestep of one minute. The computational time is significantly reduced with a factor of 300 compared to the 0.2-second timestep without losing the rotation behaviour due to changes in the short waves.

When DT uses both the AE model and Paris model, the resulting RUL prediction is lower than the prediction based solely on Paris model. The AE model overestimate the crack growth rate in the first part of the bearing life. While in the later phase, the AE model will underestimate the crack growth rate. Therefore, combining the AE model with the Paris model has a good potential.

The condition input for the DT can be measured continuous and discontinuous. By measuring the AE discontinuous the RUL prediction varied from the continuous based prediction. The discontinuous prediction results in higher values for the RUL. The AE interval of the discontinuous measured also influenced the prediction, as the RUL decreased for larger AE intervals. Meaning that the measurement of the condition will influence the RUL prediction. Therefore, it is advised to use continuous condition monitoring for the DT for the best predictions.

So, to conclude, it is possible to develop a DT which combines a theoretical fatigue model with experimental data to make RUL predictions for a highly loaded low-speed roller bearing. *However, the DT is not yet a fixed and usable figure, as the DT is based on experiments and is not yet validated.*

## 6.1 Recommendations

For future work, the used constants will need to be derived more accurate, based on a compact tension test, where the SIF, crack size and the resulting AE is monitored. As the used constants for this research were based on experimental data of two different types of steel due to the lack of experimental data available online. In addition, the constants depend on the used filtering for the AE. Combining this with the sensitivity of model, shown in Figures 28 and 29, the results can be affected by the used constants.

In addition, for the derivation of the constants, it will be advised to derive them for multiple different bearing steels to make more accurate predictions for different types of bearings.

Furthermore, the Paris constants need to be checked as well. Since, the used constants were for steel and there are multiple different types of steel. As a result, the different types will have different material properties. So, based on the compact tension test, the constants can be ensured to capture the degradation trend right.

Multiple test samples should be used for the compact tension test, as there will be some variability and scatter in the data.

There are multiple different models which are used to predict the fatigue life of a material. In this thesis, the Paris model and an AE model were used to predict the failure of a bearing. It will be advised to compare higher order fidelity models to the used approach in this thesis to see the difference in the prediction.

In the original plan, another case study was conducted. This case study was based on duration test done for a bearing which had consumed 40% of its theoretical lifetime before the duration test started. For this test, all input data for the DT is known except for the data before the test. However, it can be a useful case study to investigate further the accuracy of the RUL predictions as the failure time of the bearing is known.

Furthermore, in this thesis, only the test case of good lubrication was used, as the bearing

operates in good lubrication state most of the time. However, as the bearing degrades, the lubrication will become more contaminated with (hard) particles due to the degradation of the bearing. In addition, the lubrication can also be contaminated with fluids due to the failure of a sealing. The contamination of the lubrication will influence the degradation process of the bearing. So, for future work, it will be useful to expand the DT with the lubrication data. Meaning that a lubrication model needs to be established and combined with the theoretical and AE model.

At last, another case study where the proposed methodology of the DT can be tested is based on the linear bearing experiment done by B. Scheeren and Huisman described in [43] and [44]. As for this experiment, the bearing start in a pristine state and is run up to failure. In addition, all the needed information for the DT is available. Therefore, the used assumption of the DT can be tested.

# References

- [1] Ada mode, *How to calculate the remaining useful life (rul) of industrial assets*. [Online]. Available: <https://ada-mode.com/blog/how-to-calculate-remaining-useful-life/>.
- [2] Altair Inspire Form, *Cyclic hardening*. [Online]. Available: [https://help.altair.com/form/en\\_us/topics/form/reference/cyclic\\_hardening\\_r.htm](https://help.altair.com/form/en_us/topics/form/reference/cyclic_hardening_r.htm).
- [3] BayernCollab, *Hertzian Theory of Contact - ZFP - BayernCollab*. [Online]. Available: <https://collab.dvb.bayern/display/TUMzfp/Hertzian+Theory+of+Contact>.
- [4] Bluewater Energy Services, *Aoka Mizu - Bluewater Energy Services*, Jun. 2019. [Online]. Available: <https://www.bluewater.com/floating-production/fpso-fleet/aoka-mizu/>.
- [5] Bluewater Energy Services, *Aoka Mizu - Bluewater Energy Services*, Jun. 2019. [Online]. Available: <https://www.bluewater.com/floating-production/fpso-fleet/aoka-mizu/>.
- [6] M. Chai, X. Hou, Z. Zhang, and Q. Duan, "Identification and prediction of fatigue crack growth under different stress ratios using acoustic emission data," *International journal of fatigue*, vol. 160, p. 106 860, Jul. 2022. DOI: [10.1016/j.ijfatigue.2022.106860](https://doi.org/10.1016/j.ijfatigue.2022.106860). [Online]. Available: <https://doi.org/10.1016/j.ijfatigue.2022.106860>.
- [7] Chemeurope, *Fracture toughness*. [Online]. Available: [https://www.chemeurope.com/en/encyclopedia/Fracture\\_toughness.html](https://www.chemeurope.com/en/encyclopedia/Fracture_toughness.html).
- [8] C. Chen, X. Chen, and S. Guo, "Experimental study on acoustic emission characteristic of fatigue crack growth of self-compacting concrete," *Structural control & health monitoring/Structural control and health monitoring*, vol. 26, no. 4, e2332, Feb. 2019. DOI: [10.1002/stc.2332](https://doi.org/10.1002/stc.2332). [Online]. Available: <https://doi.org/10.1002/stc.2332>.
- [9] H.-L. Chen and J.-H. Choi, "Acoustic Emission Study of Fatigue cracks in materials used for AVL B," *Journal of nondestructive evaluation*, vol. 23, no. 4, pp. 133–151, Dec. 2004. DOI: [10.1007/s10921-004-0820-6](https://doi.org/10.1007/s10921-004-0820-6). [Online]. Available: <https://doi.org/10.1007/s10921-004-0820-6>.
- [10] A. Cheng, N.-Z. Chen, and P. Yang, "An energy principles based model for fatigue crack growth prediction," *International Journal of Fatigue*, vol. 128, p. 105 198, Nov. 2019. DOI: [10.1016/j.ijfatigue.2019.105198](https://doi.org/10.1016/j.ijfatigue.2019.105198). [Online]. Available: <https://doi.org/10.1016/j.ijfatigue.2019.105198>.
- [11] E. Ciulli, A. Betti, and P. Forte, "The applicability of the Hertzian formulas to point contacts of spheres and spherical caps," *Lubricants*, vol. 10, no. 10, p. 233, Sep. 2022. DOI: [10.3390/lubricants10100233](https://doi.org/10.3390/lubricants10100233). [Online]. Available: <https://www.mdpi.com/2075-4442/10/10/233>.
- [12] N. De Laurentis, A. Kadiric, P. M. Lugt, and P. Cann, "The influence of bearing grease composition on friction in rolling/sliding concentrated contacts," *Tribology International*, vol. 94, pp. 624–632, Feb. 2016. DOI: [10.1016/j.triboint.2015.10.012](https://doi.org/10.1016/j.triboint.2015.10.012). [Online]. Available: <https://www.sciencedirect.com/science/article/pii/S0301679X15004612>.
- [13] E. Edge and E. E. Llc, *Miner's Rule Linear damage rule*. [Online]. Available: [https://www.engineersedge.com/material\\_science/miners\\_rule\\_linear\\_damage\\_rule\\_15356.htm](https://www.engineersedge.com/material_science/miners_rule_linear_damage_rule_15356.htm).

- [14] I. El-Thalji and E. Jantunen, “A descriptive model of wear evolution in rolling bearings,” *Engineering Failure Analysis*, vol. 45, pp. 204–224, Oct. 2014. DOI: [10.1016/j.engfailanal.2014.06.004](https://doi.org/10.1016/j.engfailanal.2014.06.004). [Online]. Available: <https://doi.org/10.1016/j.engfailanal.2014.06.004>.
- [15] emweb, *Beams with axial loads*. [Online]. Available: <http://emweb.unl.edu/NEGAHBAN/Em325/16-Mohr's-circle/Mohr's%20circle.htm>.
- [16] B. van den Ende, “Load Capacity of Low Speed Steel Wheels,” Master thesis, Technische Universiteit Delft, 2021.
- [17] J. Halme and P. Andersson, “Rolling contact fatigue and wear fundamentals for rolling bearing diagnostics - state of the art,” *Proceedings of the Institution of Mechanical Engineers, Part J: Journal of Engineering Tribology*, vol. 224, no. 4, pp. 377–393, Apr. 2010. DOI: [10.1243/13506501jet656](https://doi.org/10.1243/13506501jet656). [Online]. Available: <https://doi.org/10.1243/13506501jet656>.
- [18] Z. Han, H. Luo, Y. Zhang, and J. Cao, “Effects of micro-structure on fatigue crack propagation and acoustic emission behaviors in a micro-alloyed steel,” *Materials science and engineering. A, Structural materials: properties, microstructures and processing/Materials science & engineering. A, Structural materials: properties, microstructure and processing*, vol. 559, pp. 534–542, Jan. 2013. DOI: [10.1016/j.msea.2012.08.138](https://doi.org/10.1016/j.msea.2012.08.138). [Online]. Available: <https://doi.org/10.1016/j.msea.2012.08.138>.
- [19] Heerema Marine Contractors, *AEGIR | Heerema*. [Online]. Available: <https://www.heerema.com/fleet/aegir>.
- [20] L. H. Holthuijsen, *Waves in oceanic and coastal waters*. Cambridge University Press, Jan. 2007. DOI: [10.1017/cbo9780511618536](https://doi.org/10.1017/cbo9780511618536). [Online]. Available: <https://doi.org/10.1017/cbo9780511618536>.
- [21] IBM, *What is Deep Learning? | IBM*. [Online]. Available: <https://www.ibm.com/topics/deep-learning>.
- [22] International standard ISO 281:2007, “Rolling bearings - Dynamic load ratings and rating life,” International Organization for Standardization ISO, Tech. Rep., 2007.
- [23] T. Jayakumar and C. K. Mukhopadhyay, *NDT techniques: Acoustic emission*. Elsevier, Jan. 2016. DOI: [10.1016/b978-0-12-803581-8.02682-5](https://www.sciencedirect.com/topics/chemistry/acoustic-emission#:~:text=The%20sources%20of%20AE%20are,used%20to%20predict%20material%20failure..). [Online]. Available: <https://www.sciencedirect.com/topics/chemistry/acoustic-emission#:~:text=The%20sources%20of%20AE%20are,used%20to%20predict%20material%20failure..>
- [24] J. Kumar, S. Ahmad, C. Mukhopadhyay, T. Jayakumar, and V. Kumar, “Acoustic emission studies for characterization of fatigue crack growth behavior in HSLA steel,” *Nondestructive testing and evaluation*, vol. 31, no. 1, pp. 77–96, Aug. 2015. DOI: [10.1080/10589759.2015.1070850](https://doi.org/10.1080/10589759.2015.1070850). [Online]. Available: <https://doi.org/10.1080/10589759.2015.1070850>.
- [25] M. E. Laithy, L. Wang, T. J. Harvey, and B. Vierneusel, “Re-investigation of dark etching regions and white etching bands in SAE 52100 bearing steel due to rolling contact fatigue,” *International Journal of Fatigue*, vol. 136, p. 105 591, Jul. 2020. DOI: [10.1016/j.ijfatigue.2020.105591](https://doi.org/10.1016/j.ijfatigue.2020.105591). [Online]. Available: <https://doi.org/10.1016/j.ijfatigue.2020.105591>.
- [26] J.-L. Lemaître, *A course on damage mechanics*. Springer, Jan. 1996. DOI: [10.1007/978-3-642-18255-6](https://doi.org/10.1007/978-3-642-18255-6). [Online]. Available: <https://doi.org/10.1007/978-3-642-18255-6>.
- [27] J.-L. Lemaître and J. Chaboche, *Mechanics of solid materials*. Springer, Feb. 1990. DOI: [10.1017/cbo9781139167970](https://doi.org/10.1017/cbo9781139167970). [Online]. Available: <https://doi.org/10.1017/cbo9781139167970>.



- [28] Z. Liu and L. Zhang, “A review of failure modes, condition monitoring and fault diagnosis methods for large-scale wind turbine bearings,” *Measurement*, vol. 149, p. 107002, Jan. 2020. DOI: [10.1016/j.measurement.2019.107002](https://doi.org/10.1016/j.measurement.2019.107002). [Online]. Available: <https://doi.org/10.1016/j.measurement.2019.107002>.
- [29] Y. Luo and A. Marfo, “Qualitative analysis of fatigue crack behavior in welded connection using acoustic emission technique,” *Journal of Civil Engineering and Construction Technology*, vol. 8, no. 1, pp. 1–10, Jan. 2017. DOI: [10.5897/jcect2016.0407](https://doi.org/10.5897/jcect2016.0407). [Online]. Available: <https://academicjournals.org/journal/JCECT/article-full-text/06383BC63114>.
- [30] MaintWorld, *The three mistakes of bearing lubrication*. [Online]. Available: <https://www.maintworld.com/Applications/The-Three-Mistakes-of-Bearing-Lubrication>.
- [31] MechaniCalc, *Fatigue Crack growth* | *MechaniCalc*. [Online]. Available: <https://mechanicalc.com/reference/fatigue-crack-growth>.
- [32] MechaniCalc, *Fracture Mechanics* | *MechaniCalc*. [Online]. Available: <https://mechanicalc.com/reference/fracture-mechanics#stress-intensity-factor>.
- [33] M. A. Meggiolaro and J. T. P. De Castro, “On the dominant role of crack closure on fatigue crack growth modeling,” *International Journal of Fatigue*, vol. 25, no. 9-11, pp. 843–854, Sep. 2003. DOI: [10.1016/s0142-1123\(03\)00132-4](https://doi.org/10.1016/s0142-1123(03)00132-4). [Online]. Available: [https://doi.org/10.1016/s0142-1123\(03\)00132-4](https://doi.org/10.1016/s0142-1123(03)00132-4).
- [34] W. Meng, Y. Wang, X. Zhang, S. Li, X. Bai, and L. Hou, “Prediction of fault evolution and remaining useful life for rolling bearings with spalling fatigue using digital twin technology,” *Applied Intelligence*, vol. 53, no. 23, pp. 28611–28626, Oct. 2023. DOI: [10.1007/s10489-023-05010-8](https://doi.org/10.1007/s10489-023-05010-8). [Online]. Available: <https://doi.org/10.1007/s10489-023-05010-8>.
- [35] R. Minerva, G. M. Lee, and N. Crespi, “Digital Twin in the IoT Context: A Survey on Technical Features, Scenarios, and Architectural Models,” *Proceedings of the IEEE*, vol. 108, no. 10, pp. 1785–1824, Oct. 2020. DOI: [10.1109/jproc.2020.2998530](https://doi.org/10.1109/jproc.2020.2998530). [Online]. Available: <https://doi.org/10.1109/jproc.2020.2998530>.
- [36] R. L. Norton and Worcester Polytechnic Institute, *MACHINE DESIGN: An Integrated Approach*, 4th ed. Pearson Education, 2011, vol. 436.
- [37] N. Pérez, *Fatigue crack growth*. Springer, Aug. 2016, pp. 327–372. DOI: [10.1007/978-3-319-24999-5\\_{\\_}9](https://doi.org/10.1007/978-3-319-24999-5_{_}9). [Online]. Available: [https://doi.org/10.1007/978-3-319-24999-5\\_9](https://doi.org/10.1007/978-3-319-24999-5_9).
- [38] M. Rabiei and M. Modarres, “Quantitative methods for structural health management using in situ acoustic emission monitoring,” *International journal of fatigue*, vol. 49, pp. 81–89, Apr. 2013. DOI: [10.1016/j.ijfatigue.2012.12.001](https://doi.org/10.1016/j.ijfatigue.2012.12.001). [Online]. Available: <https://doi.org/10.1016/j.ijfatigue.2012.12.001>.
- [39] D. Radaaj, *Fracture mechanics approach for assessment of fatigue strength of seam welded joints*. Jan. 1990, pp. 277–298. DOI: [10.1533/9781845698751.277](https://doi.org/10.1533/9781845698751.277). [Online]. Available: <https://www.sciencedirect.com/science/article/pii/B9781855730045500131?via%3Dihub>.
- [40] T. Roberts and M. Talebzadeh, “Acoustic emission monitoring of fatigue crack propagation,” *Journal of constructional steel research*, vol. 59, no. 6, pp. 695–712, Jun. 2003. DOI: [10.1016/s0143-974x\(02\)00064-0](https://doi.org/10.1016/s0143-974x(02)00064-0). [Online]. Available: [https://doi.org/10.1016/s0143-974x\(02\)00064-0](https://doi.org/10.1016/s0143-974x(02)00064-0).
- [41] F. Sa, *Acoustic Emission Testing: a guide*. [Online]. Available: <https://www.flyability.com/acoustic-emission-testing>.
- [42] F. Sadeghi, B. Jalalahmadi, T. S. Slack, N. Raje, and N. K. Arakere, “A review of rolling contact fatigue,” *Journal of tribology*, vol. 131, no. 4, Sep. 2009. DOI: [10.1115/1.3209132](https://doi.org/10.1115/1.3209132). [Online]. Available: <https://doi.org/10.1115/1.3209132>.

- [43] B Scheeren, “ON ACOUSTIC EMISSION CONDITION MONITORING OF HIGHLY-LOADED LOW-SPEED ROLLER BEARINGS,” Ph.D. dissertation, Technische Universiteit Delft, 2023.
- [44] B. Scheeren, M. L. Kaminski, and L. Pahlavan, “Acoustic emission monitoring of naturally developed damage in large-scale low-speed roller bearings,” *Structural Health Monitoring*, vol. 23, no. 1, pp. 360–382, May 2023. DOI: [10.1177/14759217231164912](https://doi.org/10.1177/14759217231164912). [Online]. Available: <https://doi.org/10.1177/14759217231164912>.
- [45] S. Shi, G. Wu, H. Chen, and S. Zhang, “Acoustic emission monitoring of fatigue crack growth in Hadfield Steel,” *Sensors*, vol. 23, no. 14, p. 6561, Jul. 2023. DOI: [10.3390/s23146561](https://doi.org/10.3390/s23146561). [Online]. Available: <https://doi.org/10.3390/s23146561>.
- [46] D. Shutin, M. A. Bondarenko, R. Polyakov, I. Stebakov, and L. Savin, *Prediction of remaining useful life of passive and adjustable fluid film bearings using Physics-Based models of their degradation*. Springer, Aug. 2023, pp. 211–223. DOI: [10.1007/978-3-031-40455-9\\_17](https://doi.org/10.1007/978-3-031-40455-9_17). [Online]. Available: [https://doi.org/10.1007/978-3-031-40455-9\\_17](https://doi.org/10.1007/978-3-031-40455-9_17).
- [47] S Song, “Feasibility of locally-coupled elasto-plastic damage modeling for remaining life prediction of low-speed damaged roller bearings under heavy loading condition,” Master thesis, Technische Universiteit Delft, 2021.
- [48] Studysmarter, *Fatigue crack initiation: propagation, high cycle mechanism*. [Online]. Available: <https://www.studysmarter.co.uk/explanations/engineering/materials-engineering/fatigue-crack-initiation/>.
- [49] TedAI, *End-to-End learning*. [Online]. Available: <https://www.ai-event.ted.com/glossary/end-to-end-learning#:~:text=In%20end%2Dto%2Dend%20learning,these%20features%20to%20make%20predictions..>
- [50] O. E. Today and O. E. Today, *Aoka Mizu FPSO hook-up: Third time’s the charm for Hurricane Energy*, Apr. 2020. [Online]. Available: <https://www.offshore-energy.biz/aoka-mizu-fpso-hook-up-third-times-the-charm-for-hurricane-energy/>.
- [51] TriboNet, *Hertzian contact equations for elliptical, spherical and cylindrical contacts - About Tribology*. [Online]. Available: <https://www.tribonet.org/wiki/hertz-equations-for-elliptical-spherical-and-cylindrical-contacts/>.
- [52] TriboNet, *Hertzian contact theory – About Tribology*. [Online]. Available: <https://www.tribonet.org/wiki/hertz-contact-theory/>.
- [53] J. Wang, Y. Li, R. X. Gao, and F. Zhang, “Hybrid physics-based and data-driven models for smart manufacturing: Modelling, simulation, and explainability,” *Journal of Manufacturing Systems*, vol. 63, pp. 381–391, Apr. 2022. DOI: [10.1016/j.jmsy.2022.04.004](https://doi.org/10.1016/j.jmsy.2022.04.004). [Online]. Available: <https://doi.org/10.1016/j.jmsy.2022.04.004>.
- [54] Q. J. Wang and D. Zhu, *Hertz Theory: Contact of ellipsoidal surfaces*. Springer, Jan. 2013, pp. 1647–1654. DOI: [10.1007/978-0-387-92897-5\\_493](https://doi.org/10.1007/978-0-387-92897-5_493). [Online]. Available: [https://doi.org/10.1007/978-0-387-92897-5\\_493](https://doi.org/10.1007/978-0-387-92897-5_493).
- [55] J. Yu, P. Ziehl, B. Zárate, and J. Caicedo, “Prediction of fatigue crack growth in steel bridge components using acoustic emission,” *Journal of constructional steel research*, vol. 67, no. 8, pp. 1254–1260, Aug. 2011. DOI: [10.1016/j.jcsr.2011.03.005](https://doi.org/10.1016/j.jcsr.2011.03.005). [Online]. Available: <https://doi.org/10.1016/j.jcsr.2011.03.005>.
- [56] W. Zhang, Q. Wang, X. Li, and J. He, “A simple fatigue life prediction algorithm using the modified NASGRO equation,” *Mathematical Problems in Engineering*, vol. 2016, pp. 1–8, Jan. 2016. DOI: [10.1155/2016/4298507](https://doi.org/10.1155/2016/4298507). [Online]. Available: <https://www.hindawi.com/journals/mpe/2016/4298507/>.

# A Appendix A - Derivation total number of load cycles to failure equation

By rewriting the Paris model, equation 48 to the form shown in equation 49, an equation for the number of load cycles can be established. By taking the integral on both sides from the pristine state up to the failure state. This results in equation 50.

$$\frac{da}{dN} = C (\Delta K)^n \quad (48)$$

$$dN = \frac{da}{C (\Delta K)^n} \quad (49)$$

$$N_f = \int_{a_0}^{a_f} \frac{da}{C (\Delta K)^n} \quad (50)$$

The integration can be divided into two parts, as shown in equation 51. The part that is integrating the part from the pristine state to the crack length for the last data point is simply equal to the number of load cycles  $N$ . So equation 51 simplifies to equation 52.

$$N_f = \int_a^{a_f} \frac{da}{C (\Delta K)^n} + \int_{a_0}^a \frac{da}{C (\Delta K)^n} \quad (51)$$

$$N_f = \int_a^{a_f} \frac{da}{C (\Delta K)^n} + N \quad (52)$$

For the integration, first the equation for the stress intensity factor, equation 53 has to be substituted in. By doing the substitution equation 54 is obtained. In this equation, all the terms are sorted to see the dependence on the crack length. The equation for the total number of load cycles to failure is obtained by integrating equation 54, the obtained equation is shown in equation 55

$$\Delta K = Y \tau_{se} \sqrt{\pi a} \quad (53)$$

$$N_f = \int_a^{a_f} \frac{da}{C (\tau_{se} \sqrt{\pi a})^n} + N = \int_a^{a_f} \frac{1}{C (\tau_{se} \sqrt{\pi})^n} \cdot a^{-\frac{n}{2}} da + N \quad (54)$$

$$N_f = \left[ \frac{1}{C (\tau_{se} \sqrt{\pi})^n} \cdot \left( \frac{-2}{n-2} \right) a^{-\frac{n}{2}+1} \right]_a^{a_f} + N \quad (55)$$

# B Appendix B - RUL of bearing based on the Paris model

In Figure 54, the RUL prediction of the bearing is shown. This prediction was solely based on the Paris model. The difference with Figure 38 is the used limits for the colorbar. Figure 54 is has a higher limit value, to see the differences in the degradation.

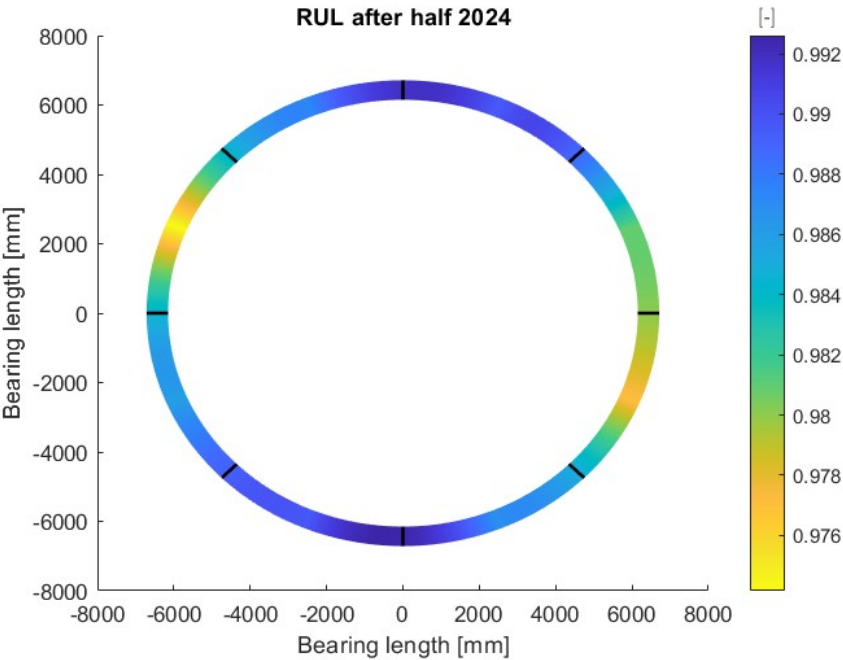


Figure 54: The RUL of the bearing of the Aoka Mizu in half 2024

# C Appendix C - Remaining useful life based on only AE

In this appendix, the RUL development based on sensor locations A,B and L is shown.

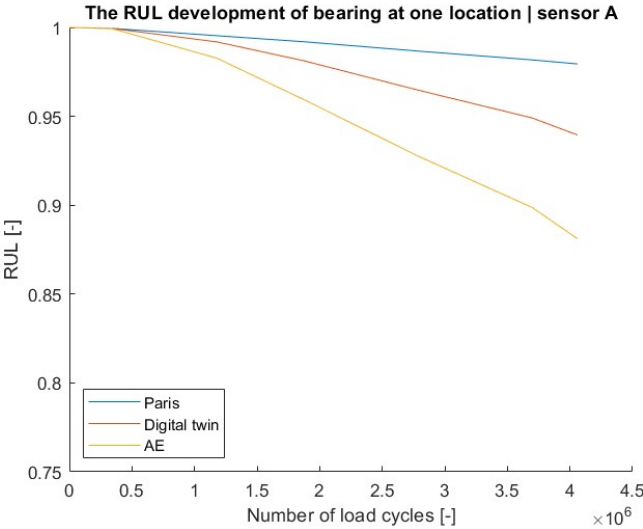


Figure 55: The RUL development based on only AE of sensor location A

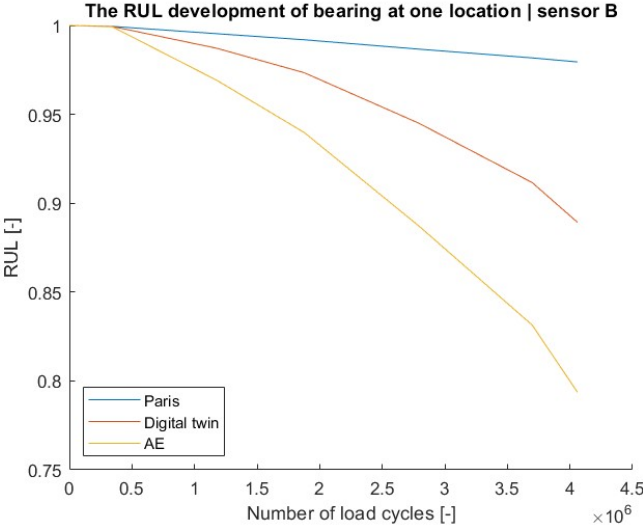


Figure 56: The RUL development based on only AE of sensor location B

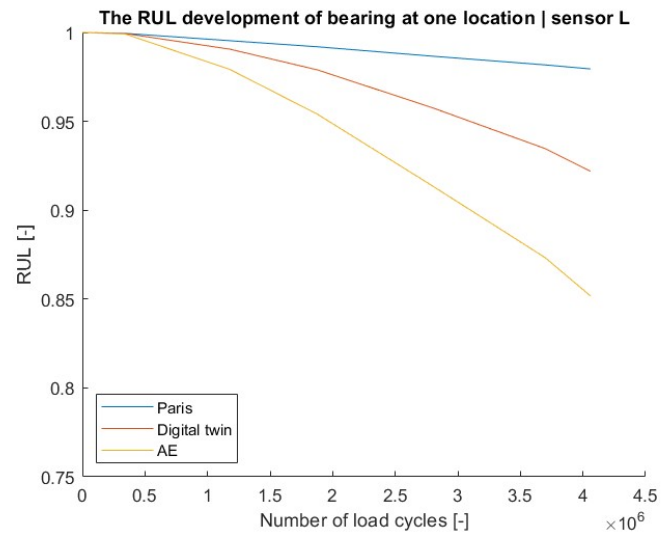
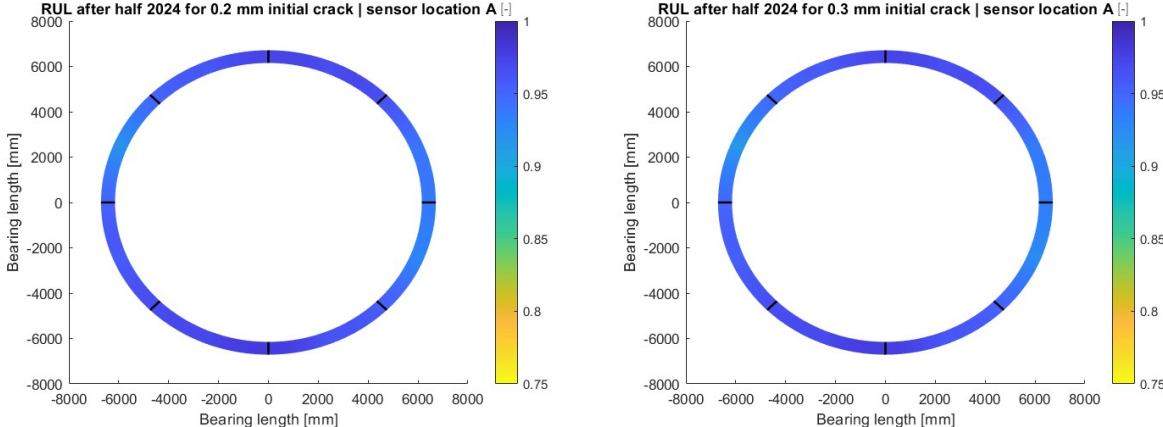


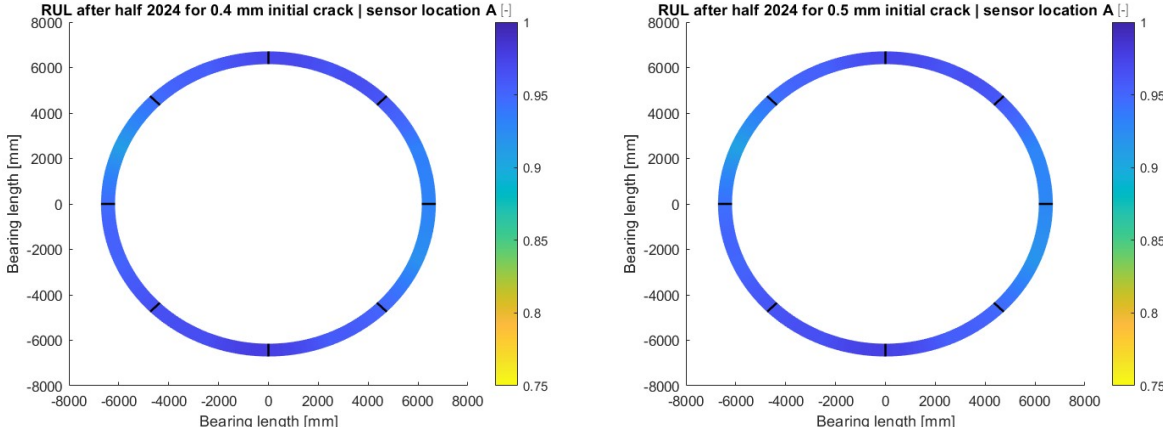
Figure 57: The RUL development based on only AE of sensor location L

# D Appendix D - Sensitivity study

In this Appendix, the remaining figures of chapter 5.2.4 Sensitivity study are shown. In Figures 58 to 60, the RUL predictions for the different initial crack sizes are shown for the sensor locations A,B and L, respectively.

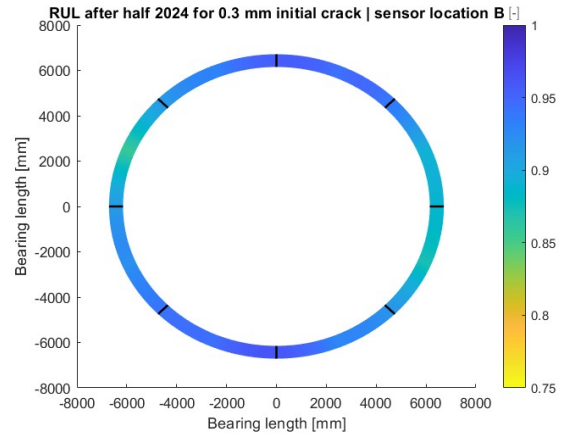
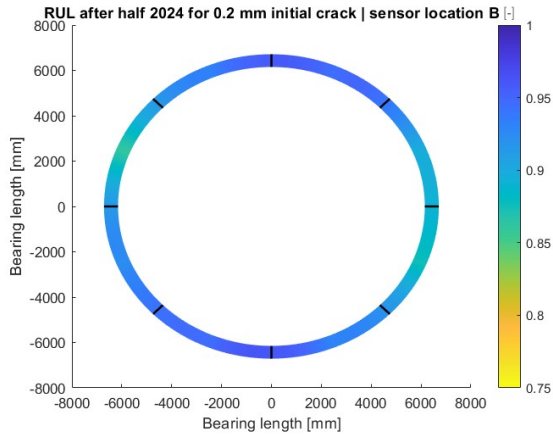


(a) The RUL based on an initial crack size of 0.2 mm (b) The RUL based on an initial crack size of 0.3 mm



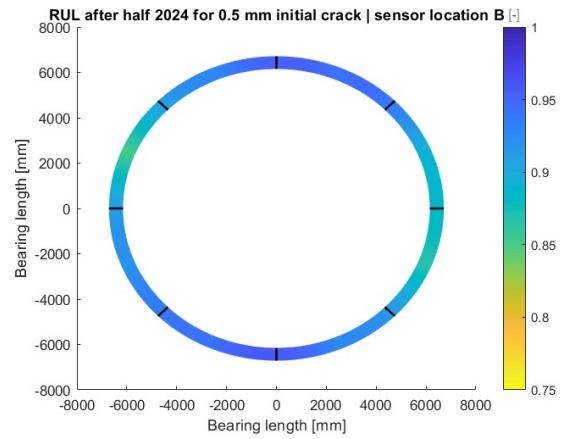
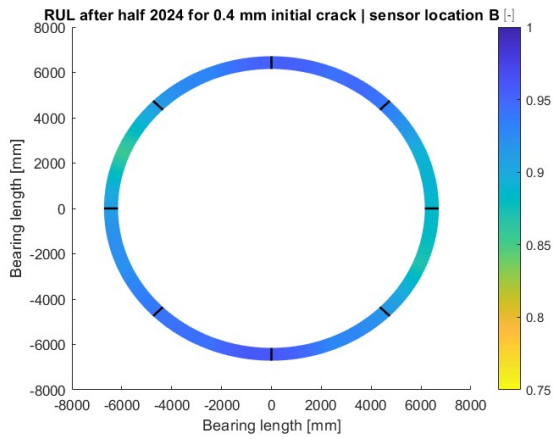
(c) The RUL based on an initial crack size of 0.4 mm (d) The RUL based on an initial crack size of 0.5 mm

Figure 58: The RUL predictions based on different initial crack sizes for sensor location A after half 2024



(a) The RUL based on an initial crack size of 0.2 mm

(b) The RUL based on an initial crack size of 0.3 mm

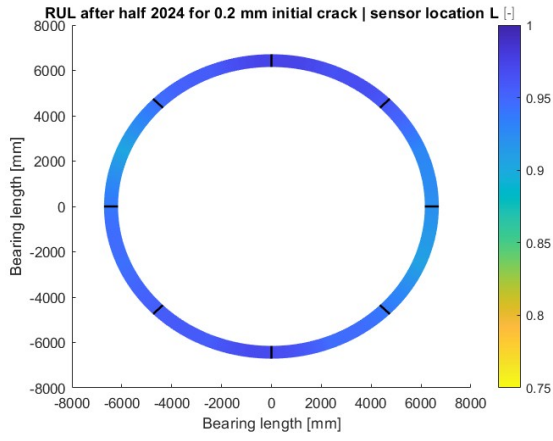


(c) The RUL based on an initial crack size of 0.4 mm

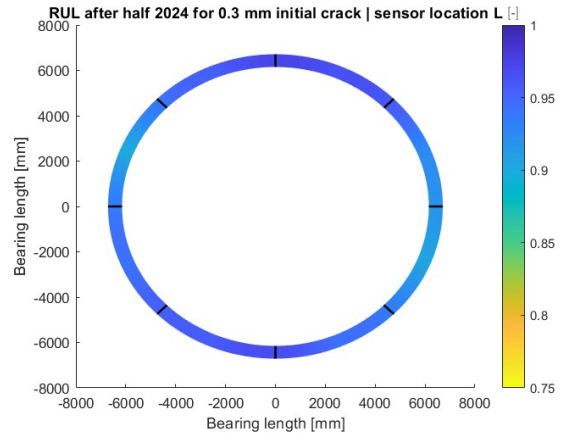
(d) The RUL based on an initial crack size of 0.5 mm

Figure 59: The RUL predictions based on different initial crack sizes for sensor location B after half 2024

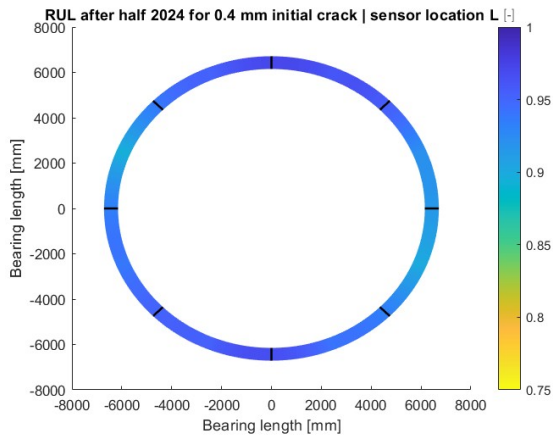




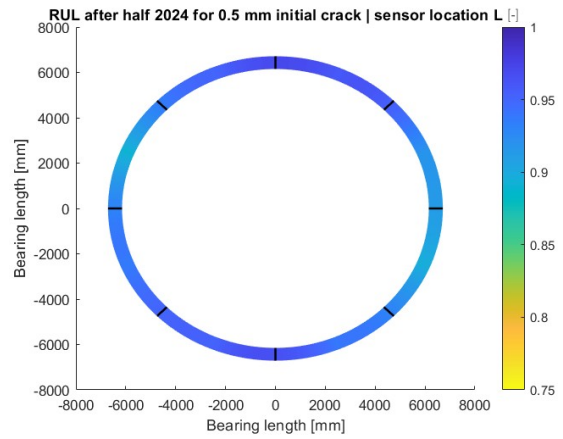
(a) The RUL based on an initial crack size of 0.2 mm



(b) The RUL based on an initial crack size of 0.3 mm



(c) The RUL based on an initial crack size of 0.4 mm



(d) The RUL based on an initial crack size of 0.5 mm

Figure 60: The RUL predictions based on different initial crack sizes for sensor location L after half 2024

In Figures 61 to 63, the RUL development is shown for the different initial crack sizes for the sensor locations A, B and L, respectively.

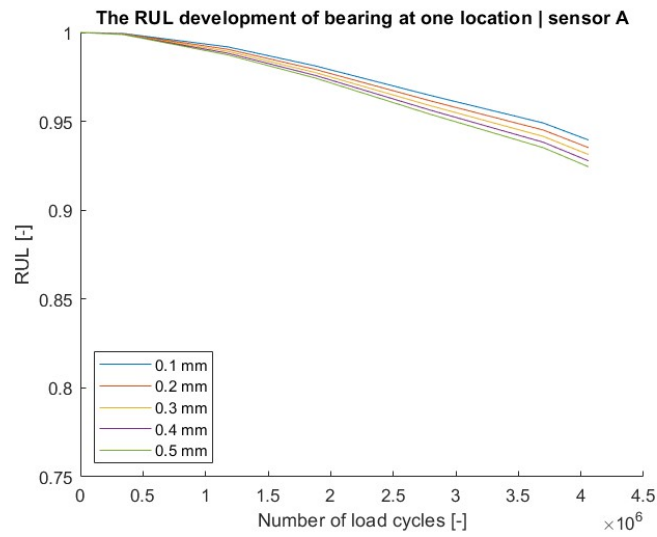


Figure 61: The development of the RUL for the different initial crack sizes for sensor location A

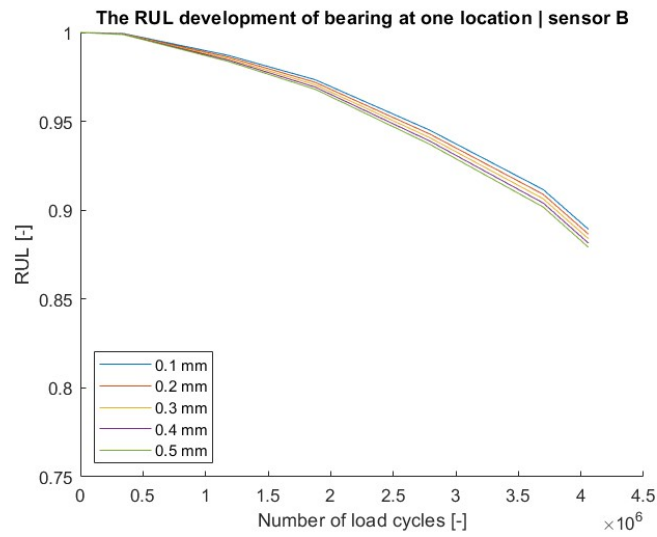


Figure 62: The development of the RUL for the different initial crack sizes for sensor location B

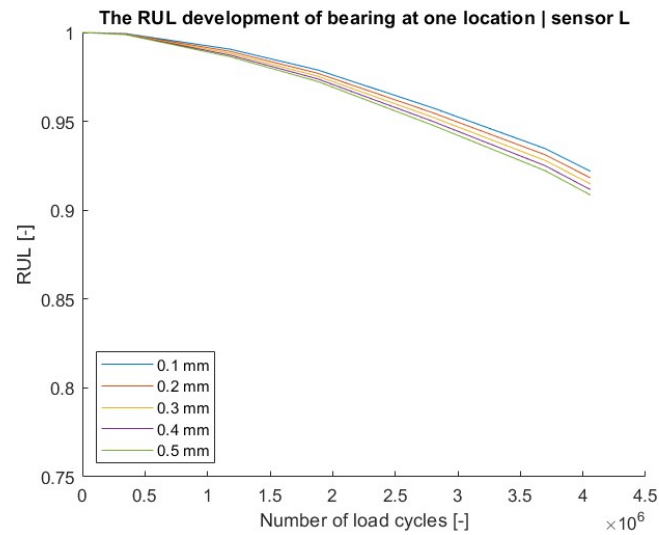


Figure 63: The development of the RUL for the different initial crack sizes for sensor location L

In Figures 64 to 66, the sensitivity of the RUL prediction to the initial crack size for sensor locations A, B and L are shown, respectively.

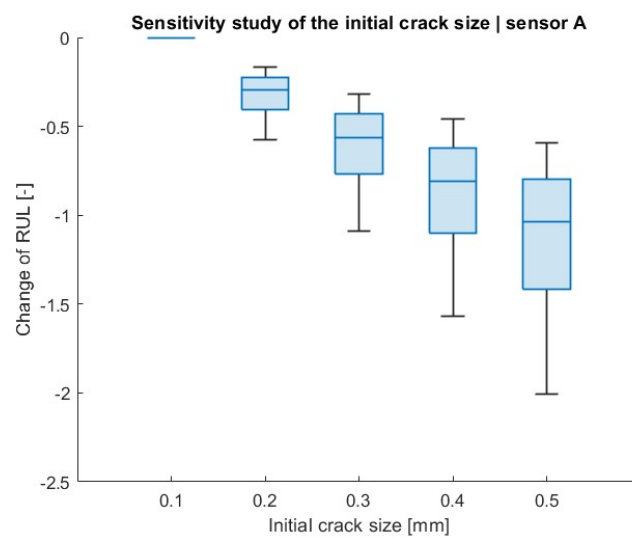


Figure 64: The sensitivity of the RUL prediction to the initial crack size for sensor location A

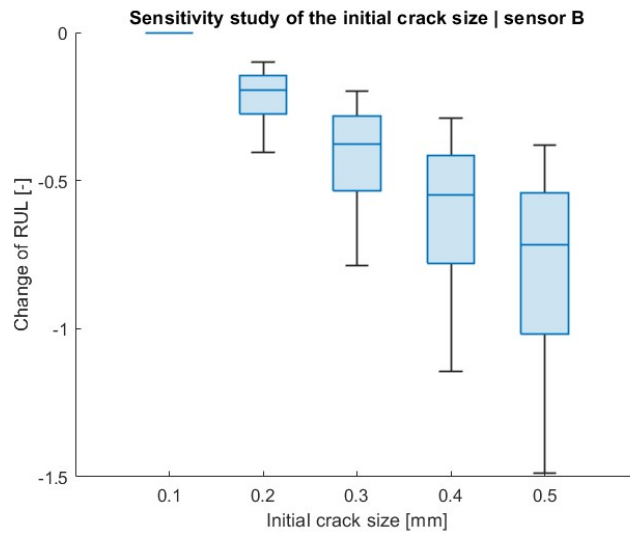


Figure 65: The sensitivity of the RUL prediction to the initial crack size for sensor location B

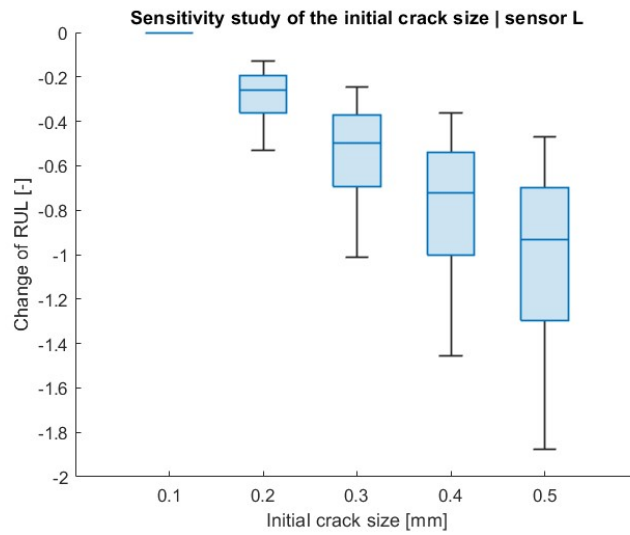


Figure 66: The sensitivity of the RUL prediction to the initial crack size for sensor location L

# E Appendix E - Influence AE interval

In this appendix, the remaining figures for the different sensor locations are shown for the chapter 5.2.5 Influence AE interval. In Figures 67 to 69, the RUL prediction is shown for the different AE intervals for the sensor locations A,B and L, respectively.

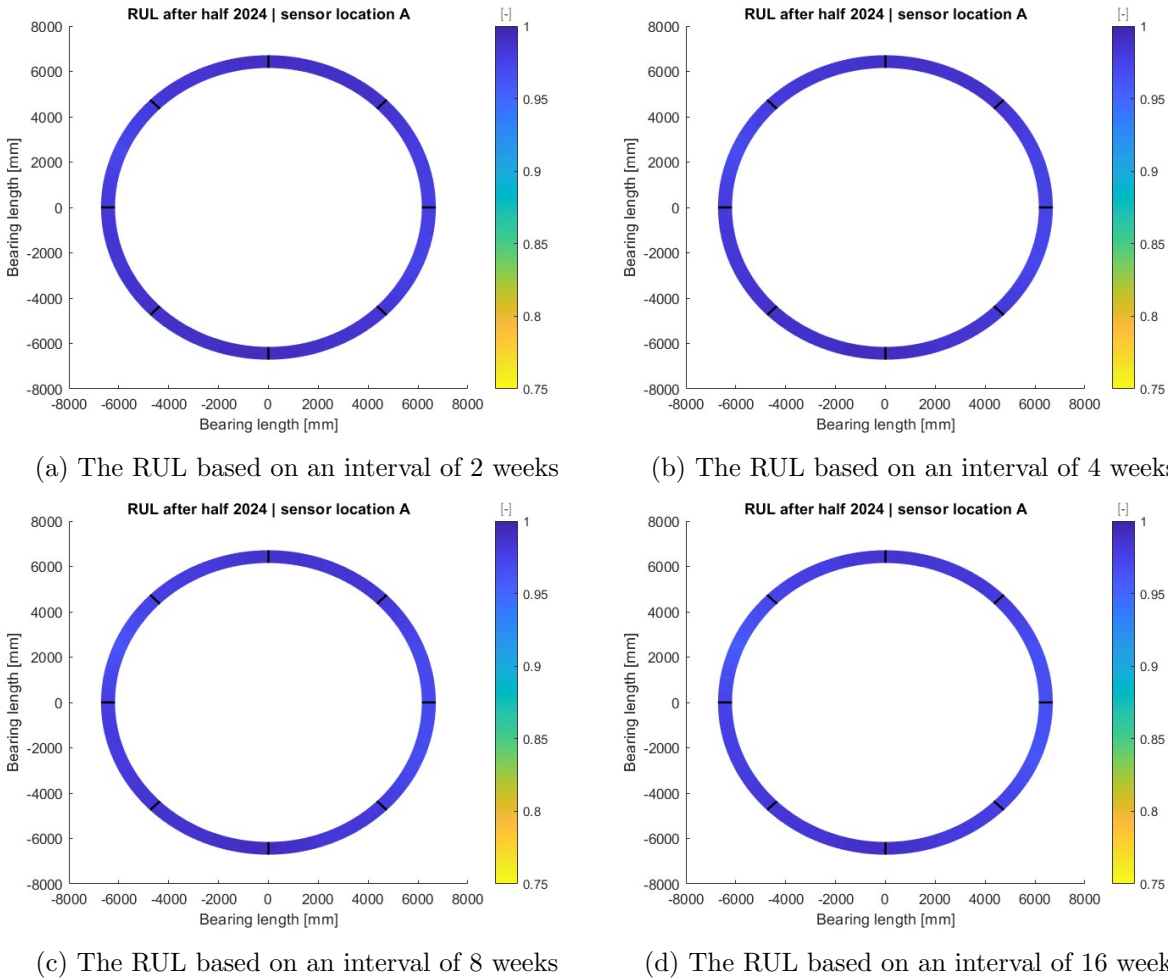
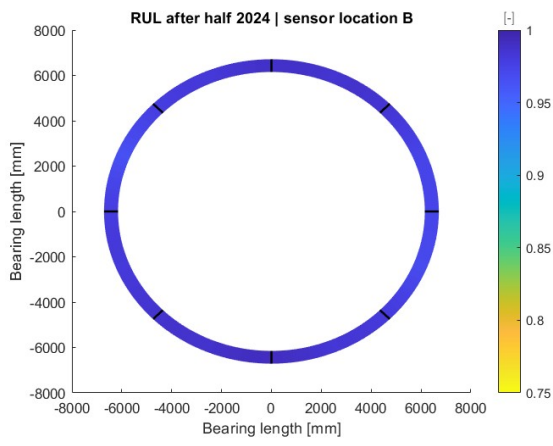
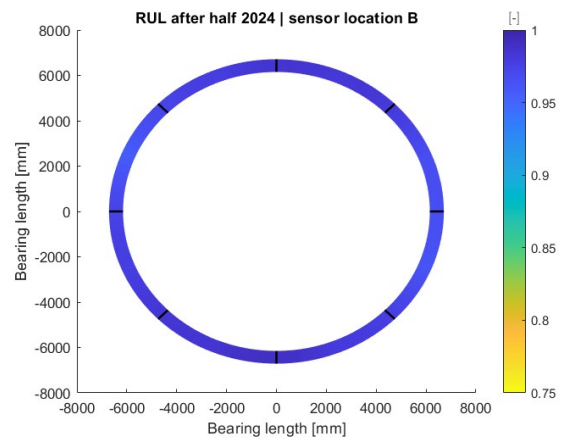


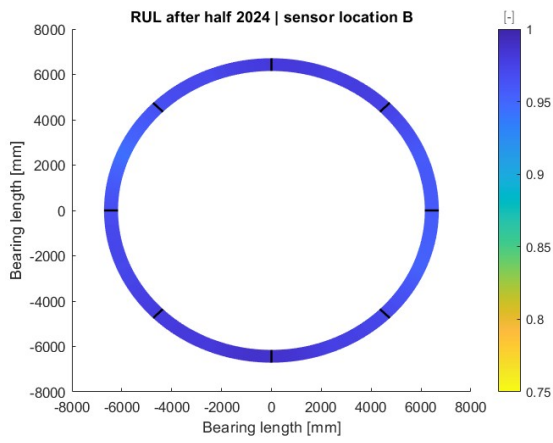
Figure 67: The RUL predictions based on different AE intervals for sensor location A after half 2024



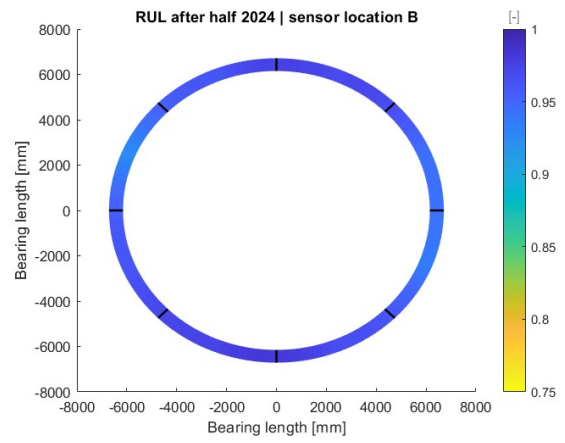
(a) The RUL based on an interval of 2 weeks



(b) The RUL based on an interval of 4 weeks

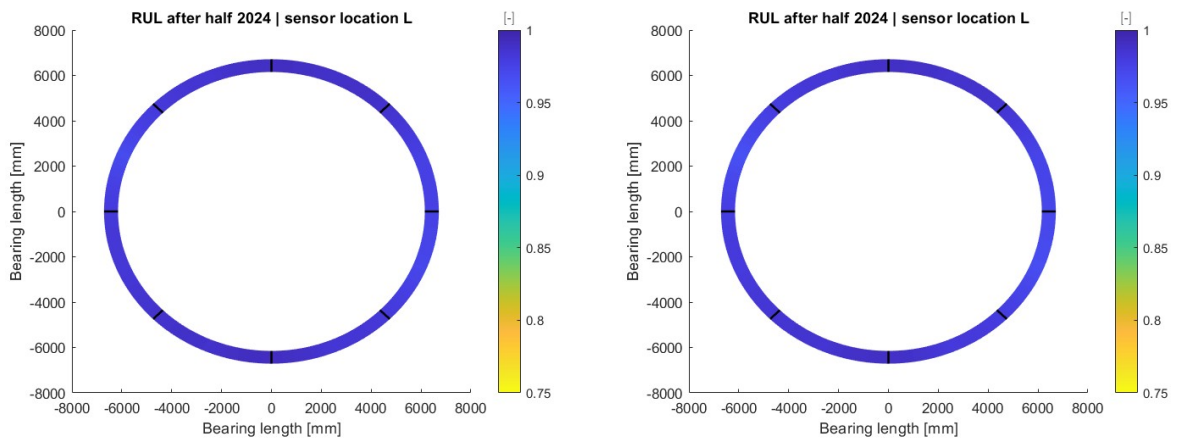


(c) The RUL based on an interval of 8 weeks



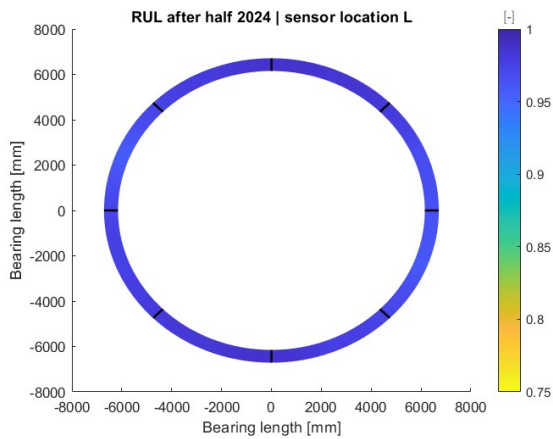
(d) The RUL based on an interval of 16 weeks

Figure 68: The RUL predictions based on different AE intervals for sensor location B after half 2024

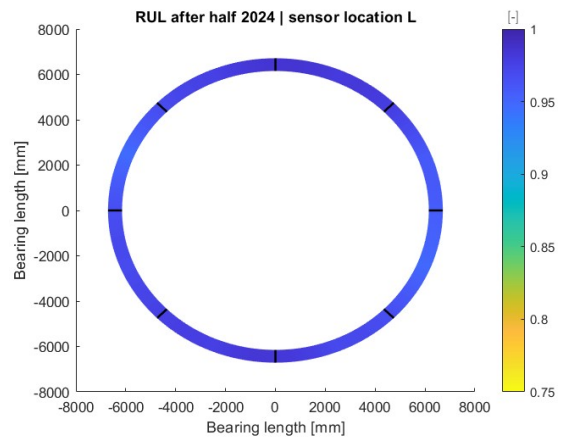


(a) The RUL based on an interval of 2 weeks

(b) The RUL based on an interval of 4 weeks



(c) The RUL based on an interval of 8 weeks



(d) The RUL based on an interval of 16 weeks

Figure 69: The RUL predictions based on different AE intervals for sensor location L after half 2024

In Figures 70 to 72, the RUL development for the different AE intervals are shown for the sensor locations A,B and L, respectively.

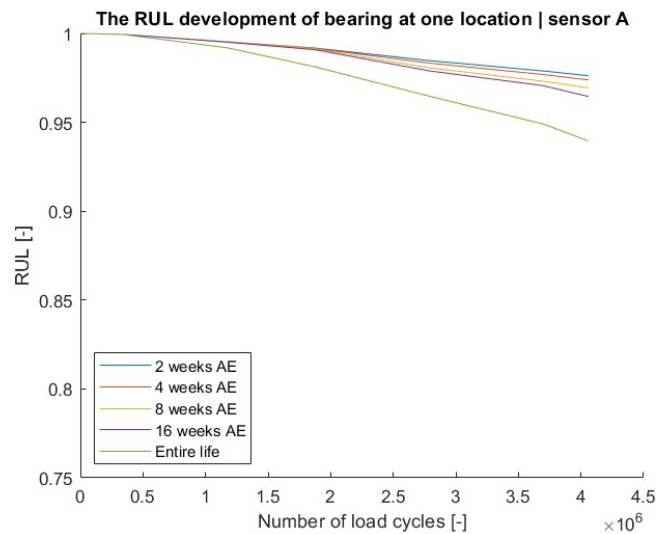


Figure 70: The RUL development for the different AE intervals for sensor location A

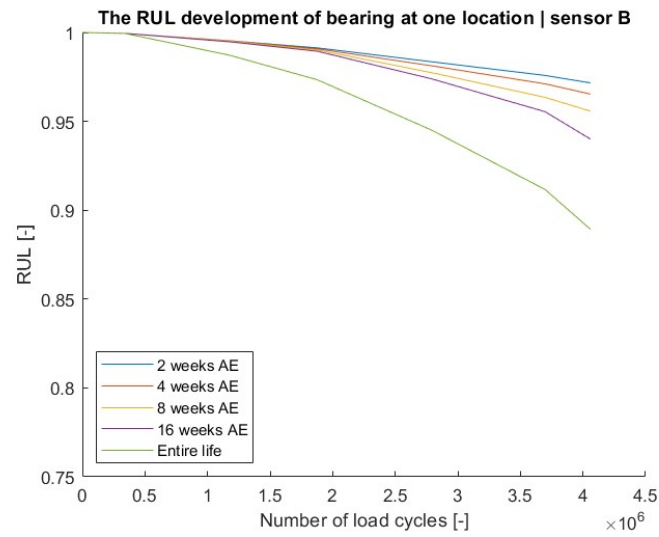


Figure 71: The RUL development for the different AE intervals for sensor location B

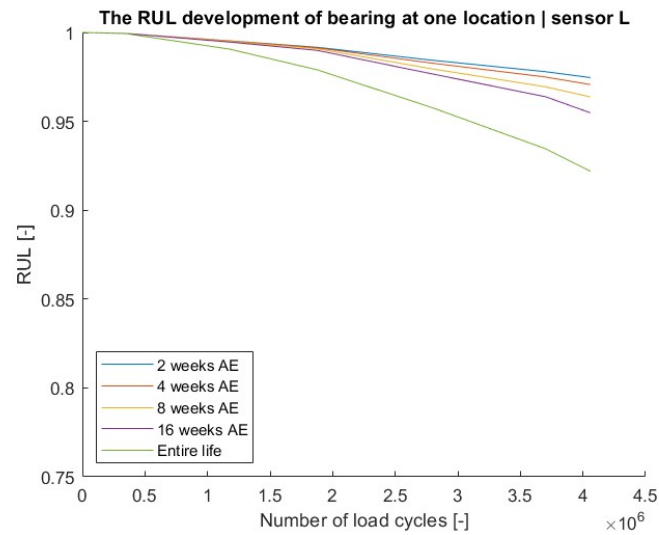


Figure 72: The RUL development for the different AE intervals for sensor location L